International journal
for science, technics and
innovations for the industry

MACHINES TECHNOLOGIES MATERIALS

YEAR XVII Issue 7 / 2023 ISSN PRINT 1313-0226
ISSN WEB 1314-507X



Published by
Scientific technical
Union of Mechanical Engineering

MACHINES. TECHNOLOGIES. MATERIALS

INTERNATIONAL SCIENTIFIC JOURNAL

ISSN PRINT 1313-0226, ISSN WEB 1314-507X, YEAR XVII, ISSUE 7 / 2023

INTERNATIONAL EDITORAL BORARD

EDITOR IN CHIEF:

Georgi Popov	Technical University of Sofia	BG

MEMBERS:

Abdrakhman Naizabekov	Rudny industrial institute	KZ
Ahmet H. Ertas	Bursa Technical University	TR
Albert Albers	Karlsruhe Institut of Technology	DE
Andrzej Golabczak	Lodz University of Technology	PL
Dimitar Karaivanov	University of Chemical Technology and Metallurgy, Sofia	BG
Dobre Runchev	Ss. Cyril and Methodius University in Skopje	NM
Emilia Abadjieva	Akita University	JP
Erdem Camurlu	Akdeniz University, Antalya	TR
Eugen Sheregii	University of Rzeszow	PL
Franz Haas	Graz University of Technology	AT
Galina Nicolcheva	Technical University of Sofia	BG
Gennadii Bagliuk	Institute for Problems of Materials Science NAS of Ukraine, Kiev	UA
Georgii Raab	Ufa State Aviation Technical University	RU
Gregory Gurevich	Shamoon College of Engeeniring, Ashdod	IL
Hiroyuki Moriyama	Tokai University, Hiratsuka	JP
Idilia Batchkova	University of Chemical Technology and Metallurgy, Sofia	BG
Ivan Kralov	Technical University of Sofia	BG
Ivan Kuric	University of Zilina	SK
Julieta Kaleicheva	Technical University of Sofia	BG
Katia Vutova	Institute of Electronics, Bulgarian Academy of Sciences	BG
Maria Nikolova	Angel Kanchev University of Ruse	BG
Natasa Naprstkova	Jan Evangelista Purkyne University in Usti nad Labem	CZ
Oana Dodun	Gheorghe Asachi Technical University of Iasi	RO
Ognyan Andreev	Technical University of Sofia	BG
Predrag Dasic	High Technical Mechanical School of Trstenik	RS
Rasa Kandrotaite	Kaunas University of Technology	LT
Raul Turmanidze	Georgian Technical University, Tbilisi	GE
Roumen Petrov	Ghent University	BE
Sergey Dobatkin	National University of Science and Technology "MISIS", Moscow	RU
Souren Mitra	Jadavpur University, Kolkata	IN
Svetlana Gubenko	National Metallurgical Academy of Ukraine, Dnipro	UA
Vedran Mrzljak	University of Rijeka	HR
Wu Kaiming	Wuhan University of Science and Technology	CN

TECHNICAL EDITORS:

M. Sc. Eng. Radoslav Daskalov,
M. Sc. Eng. Oleg Mihailov

Scientific and technical union of mechanical engineering
108 R. S. Rakovski str., Sofia, Bulgaria
www.stumejournals.com, office@stumejournals.com

C O N T E N T S

MACHINES

Design of lng tank Type C
Helena Galić, Vedran Slapničar, Smiljko Rudan 244

Example of the maintenance of a machine pero (D 2504-019) for cleaning metal parts in the working conditions of OEM company from the autotive industry
Ismar Alagić 255

TECHNOLOGIES

Renovation of moulds for high-pressure casting of aluminium by laser cladding
Janette Brezinová, Miroslav Džupon 259

AFM morphology of sol gel coatings on glass for photovoltaics
Stancho Yordanov, Silviya Simeonova, Mihaela Aleksandrova, Vladimir Petkov, Bojidar Jivov 262

Application of reverse engineering techniques in automotive component design
Kender Štefan, Brezinová Janette 264

Thermal decomposition of biomass, significance of biochar
Viktor Madár, András Betovics, Norbert Schrempf, László Tóth 267

New optical method in laser phototherapy
Alexander Gisbrecht, Luchezar Avramov 270

Antibacterial Coatings Containing Nanodiamonds
Anna Karczemska, Michał Szczypiński, Dariusz Witkowski, Józef Doering, Radosław Wach, Bożena Rokita, Alicja Olejnik, Beata Kolesińska, Justyna Frączyk, Anna Gajda, Sylwia Magdziarz, Totka Bakalova, Lucie Svobodova, Petr Exnar, Irena Slamborova, Petr Louda, Ahmed El Mallul, Remigiusz Pawelczyk, Stanisław Mitura 272

MATERIALS

The study of the corrosion zinc-nickel coated ST2 stainless steel
Julieta Daniela Chelaru, Maria Oana Felecan 275

Structure, phase composition and tribological properties of iron-based composites *in situ* synthesized from powdered Fe—high-carbon ferrochrome mixtures
Yevheniia Kyryliuk, Genadii Bagliuk, Iaroslav Sytnyk, Serhiy Ivanchenko., Victor Varchenko 278

Production method role for the composite powders quality
Krasimira Toncheva, Zoya Savova, Luben Lakov 282

Development of a composite alloy zinc-containing material and investigation of its influence on the chemical composition of BRSN5ZN5PB5 powders produced by the method of induction melting and spraying the melt with an inert gas
Aliaksandr Ilyushchanka, Ruslan Kusin, Iryna Charniak, Aliaksei Kusin 285

Structure and physical-mechanical properties of bulk and ribbon amorphous and nanocrystalline iron-based alloys
Viktor Nosenko, Maksym Nizameiev, Oleksandr Semyrga, Vitaliy Bevz, Mykola Skoryk, Vasyl Kyrylchuk, Oleksandr Kondaurov 288

Design of lng tank Type C

Helena Galić[1], Vedran Slapničar[1], Smiljko Rudan[1]
[1]University of Zagreb, Faculty of Mechanical Engineering and Naval Architecture, Zagreb, Croatia

ABSTRACT: :*Cylindrical tank-type c is designed for cruise passenger ships trying to adopt hull space and meet the requirements of propulsion. Tank must be a double wall with the vacuum space in between, which is also fulfilled with the perlite as insulation. The main input for the design was a tank capacity of 430 m^3, vapor pressure, and available space inside of hull structure. The holding period of the boil-off gas is limited to 21 days of ship voyage. Trying to satisfy the volume capacity of the inner tank different dished end of tank was observed. The inner tank is divided into segments for the calculation of hydrodynamic pressure. According to classification rules, dnv and igc rules tank thickness, supports, stiffening and vacuum rings are determined to satisfy bending and buckling requirements. Some of the requirements were according to british standards for validation of the results. The material that is used for calculation is stainless steel 304 l. The main goal of this paper is to provide the optimal design of the lng tank type c considering the mass of the whole lng tank, with attendance to reduce the steel mass of the structure by optimizing shell thicknesses and the number of vacuum rings. After analytical calculations are made finite element analysis is used for verification of the given results. According to the given results space for improvements of tank-type c was observed.*

KEYWORDS: *TANK TYPE C; VAPOR PRESSURE; CLASSIFICATION RULES; DISHED END; SUPPORTS, BENDING; BUCKLING; STIFFENING AND VACUUM RINGS; FINITE ELEMENT ANALYSIS*

1. Introduction

According to IMO regulations, [1] low emissions ships should be operated in the next years. Low carbon emission is mandatory to satisfy all regulations, which benefits global climate change. Critical role to relevant environmental benefits is associated with Liquified Natural Gas [2]. The demand to produce cruise ships is still increasing. Regarding to LNG newbuilds for 2021. and 2024. according to DNV- rules the largest percentage refers to Cruise ships [3].

The aim of this paper is to analyze storage tank type C which holds Liquefied Natural Gas that is used for dual fuel vessels. Natural gas is a cleaner burning fuel which can reduce sulfur oxide (SO2) emissions by 90% to 95% and carbon dioxide (CO2) emissions by 20% to 25% [4]. Not only that LNG satisfy the demand for clean fuel it is also suitable for limited space which is an advantage for cruise ships. For the same voyage period amount of space will be much higher for the battery system than for tank type C.

Dual fuel ships have voyage limitations for LNG which is called Boil off gas. BOG is a state of LNG evaporation during a small heat increase which should not be reached in this study for 21 days. To eliminate the LNG evaporation state, proper thermal insulations are used, vacuum and perlite. Perlite insulation has much lower heat flux than vacuum insulation, therefore it has significant role in the heat transferee [5]. The gas supply system provides the engines with the required quantity of regasified LNG and with a pressure inlet from 5-9 bar which is suitable for Otto cycle engines [6].

According to the IGC Code [7] cargo tanks are categorized into integral, membrane, semi-membrane, and independent types. Independent tanks, which are subcategorized into A, B, and C categories, are not part of the ship's hull and are self-supporting. A common feature of types A and B is that the design vapor pressure must be less than 0.7 bar and for tank type C are much higher. Generally, Type C tanks are used as the fuel tank in LNG-fueled ships since they can withstand BOG [8]. IMO tank type C, as a pressure vessel, meets the pressure vessel criteria by having a design vapor pressure not less than the Maximum allowable relief valve setting (MARVS) where maximum allowable working pressure (MAWP) is set to 90% of MARVS [7].

Most of the scientific paper refers to utilization of the boil- off gas, sloshing and thermal analysis. For example: regasification under different filling ratio in type C [9], development of dynamic model to investigate the thermodynamic behaviors of the pressurized LNG fuel tanks [10] and under sloshing excitation [11]. Design procedure of structural integrity of tank type C is done according to other pressure vessel standards or codes such as ASME Boiler and Pressure Vessel (BPV) Code [12], [13]. If the Ship entered the US coast Tank design requirements should meet the US Coast Guard requirements [14]. Regarding to the European standards David Nah has made comparison between Design of Unfired pressure vessel EN 13445 with ASME VIII and British Standard PD5500[15].

Regarding all Codes the entire methodology of design tank type C can be segmented into three stages: heat transfer analysis, structural analysis, and fatigue analysis [16].

At this paper calculations are made according to DNV-GL rules following PD5500 rules. All calculations are done regarding DNV strength analysis [17] comparing with the DNVGL-RU-SHIP-Part 5 Chapter 7 Liquified gas tankers [18] which provides much more information. DNVGL-RU-SHIP-Part4 Chapter 7 Pressure equipment [19] is used to validate most of the formulas and results from DNV strength analysis. DNVGL-RU-SHIP-Part5 Chapter 5 Liquified gas carriers [20] are like DNV strength analysis, but it is used for comparison. Material properties are selected from DNVGL-RU-SHIP-Part2 Chapter 2 Metallic materials [21]. PD5500 British Standard is used to calculated construction details for the cylinder's mid-span and in the saddle's plane, which results are validated with Finite Element Method FEM direct calculation considering primary and secondary stresses.

The goal of this paper is to provide basic structure designed procedure according to different DNV-GL chapters. Distinction between primary and secondary stresses applied to model and comparison of analytical calculated stresses by PD5500 and obtained stresses for exact point at the FEM model. Given results will show analytical accuracy or robustness which may be sufficient for the first part of calculations and for further optimization process FEM direct calculations will provide area for simplification or improvements regarding to the first part of the calculations.

2. *Methods*

Cylindrical tank type C consists of an inner tank with or without a stiffener ring, an outer shell with vacuum rings, support between the inner and outer surface, and saddle support for an outer shell. Between inner and outer shell is perlite and vacuum. Main input was vapor pressure and volume constrain relating to the tank. After generating the geometry and obtaining inner and outer thickness, stiffener, and vacuum rings according to the DNV rules and British standard PD500 was used for critical stresses at the tank. This stresses at the specific point indicate which analytical calculations are similar to the same stress point in FEM model and which analytical calculations have large deviations from the FEM analysis. Understanding of primary and secondary maximum allowable stresses as limitations leads to iteration process of thickness. Summary of the design concept is shown at Fig.1

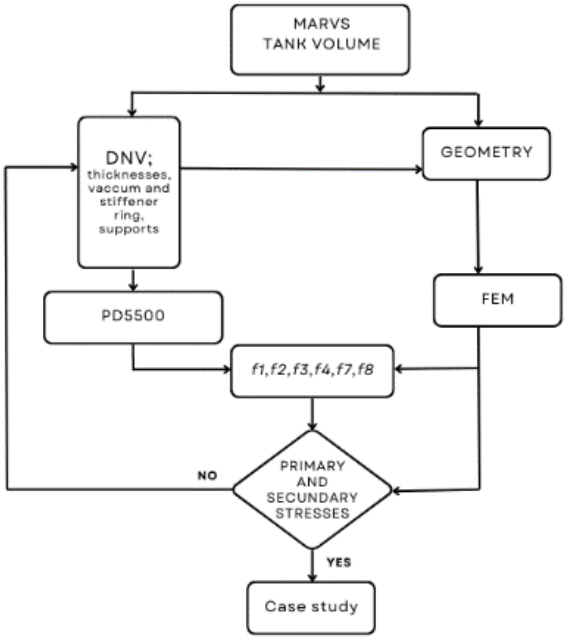


Fig. 1 *Summary of the design concept*

2.1 Inner tank

The inner tank consists of two parts, cylindrical and dished end, which can be spherical, elliptical or torispherical. The filing limit of the inner tank according to the IGF code is 83% of the total capacity, and the rest of the space is left as storage for LNG evaporation. The inner tank is designed to withstand bending stresses occurring under internal pressure, the weight of liquid, the mass of the tank, and added equipment. Internal pressure is defined as:

$$p_{eq} = p_o + p_{gd,max} + p_v \quad [\text{MPa}] \tag{1}$$

where p_o represents vapor pressure, $p_{gd,max}$ is maximum gravitational and dynamic pressure and p_v is vacuum pressure.

Vapor pressure is given as an input value, vacuum is taken as absolute value for the purpose of calculation and maximum gravitational and dynamics pressure is defined by:

$$(p_{gd})_{\max} = \frac{a_{\alpha\beta} Z_{\alpha\beta} \rho}{1.02 \cdot 10^2} \quad [\text{MPa}] \tag{2}$$

where $a_{\alpha,\beta}$ stand for dimensionless accelerations, $Z_{\alpha,\beta}$ is liquid heights, ρ is specific density and α, β refers to angle in longitudinal and transvers directions.

Different heights of liquid value are calculated for y-z (3) and x-z (4) tank plane for different angle α and β at the point of the tank segments, which are determined by the maximum width of the plate.

$$Z_{\alpha,\beta} = y\, sin_{\alpha\beta} + z\, cos_{\alpha,\beta} + R \tag{3}$$

$$Z_{\alpha,\beta} = x\, sin_{\alpha\beta} + z\, cos_{\alpha,\beta} + R \tag{4}$$

where Z stands for heights of liquid, x, y, z are coordinates of the specific point at the tank segment in 2D plane, and R is radius of the torispherical part of the tank for longitudinal plane and for transfer plane R is radius of the cylinder.

To calculate the component of dynamic pressure inside of LNG tank acceleration ellipsoid is used, see Figure 2. The longitudinal and transverse planes of the ellipsoid include ship acceleration components a_x, a_y, a_z duo to ship motions which include geometrical characteristics of the ship. Components of static weight are included in a_x, a_y accelerations while a_z does not include the component due to the static weight. The intersection of a straight line and ellipsoid gives Equation (5) and 6). For x-z longitudinal plane

$$x_{1,2} = \frac{-2kla_x^2 \pm \sqrt{4k^2 l^2 a_x^4 - 4a_x^2 (a_z^2 + k^2 a_x^2)(l^2 - a_z^2)}}{2(a_z^2 + k^2 a_x^2)} \tag{5}$$

$$k = \text{tg}(\pi/2 - \beta),\ l = 1 \tag{6}$$

where acceleration components a_x, and a_z are given in the IGC Rules [22], which correspond to the probability of exceedance of 10-8 in the North Atlantic, and k is equal to the angle that a straight line of liquid is closing with a_x direction in x-z plane (6) where straight line is written as:

$$z_{1,2} = kx + l \tag{7}$$

Dimensionless accelerations $a_{\alpha,\beta}$ can be calculated from Pythagoras theorem for the absolute value of $z_{1,2}$ and $x_{1,2}$ for different angle. The same methodology is applied for a transverse plane of acceleration ellipsoid for different angles of α shown in Figure 2.

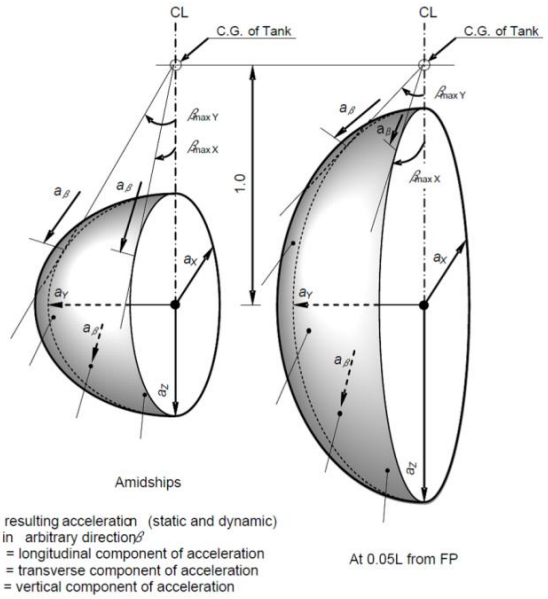


Fig. 2 *Acceleration ellipsoid*

After determination of internal liquid pressure P_{gd} for each segment of the tank thickness, inner shell is calculated by given Equation from (8) to (10).

cylindrical thickness: $t_1 = \frac{pR_c}{10\sigma_t e - 0.5p} + c$ (8)

spherical thickness: $t_2 = \frac{pR_s}{20\sigma_t e - 0.5p} + c$ (9)

torspherical thickness: $t_3 = \frac{DK}{20\sigma_t e} + c$ (10)

Where σ_t is design equivalent stress given in MPa, e is joint efficiency factor, taken as 1.0 for independent tank type, *c* is corrosion thickness which is equal to 0.0 generally for inside tanks, *Rc* is inner radius for cylinder given in mm, Rs is inner radius for sphere given in mm, *D* is outer diameter given in mm and *K*, factor which considers the stress at the conjunction, and *p* is the pressure for inner tank and in case of outer tank *p* is equal to P_{ed} given in N/mm^2.

Design equivalent stress f is determined as a lower ratio of these two values: R_m/A and R_{eH}/B, where R_{eH} is yield stress and R_m tensile strenght. Whereas for austenitic stainless-steel A= 3,5 and B= 1,5 according to IGC code. Austenitic stainless steel doesn't lose mechanical properties at -196 °C.

Cylindrical part of inner shell occurs the membrane stresses which are equivalent to primary σ_m Von Mises general membrane stress shown Equation (11):

$$\sigma_m \leq f \quad (11)$$

, and for σ_L primary local membrane discontinuities this equation is relevant:

$$\sigma_L \leq 1.5f \quad (12)$$

Acceptance criteria for global stresses in the cylindrical shell according to DNV Strength analysis for circumferential or hoop stresses and longitudinal stress is given by Equations (13) to (14):

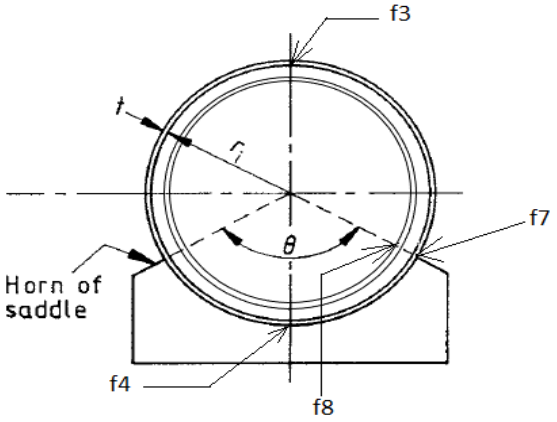
circumferential stress: $\sigma_h \leq 1.5f$ (13)

longitudinal stress: $\sigma_z \leq 0{,}8\,R_{eH}$ (14)

Primary membrane stresses at the mid-span according to PD5500 given as f_1, and f_2 are involving the longitudinal stresses:

$$f_1 = \frac{p_m r}{2t} - \frac{M_2}{\pi r^2 t} \quad (15)$$

$$f_2 = \frac{p_m r}{2t} + \frac{M_2}{\pi r^2 t} \quad (16)$$



Where r and t are geometrical characteristic of the cylinder, M_2 is longitudinal bending moment at the mid-span of cylinder and p_m *is* pressure in the centerline of the tank.

Fig. 3 *Longitudinal and circumferential stresses at the point*

2.2 Dished end

Dished end could be spherical, elliptical or torispherical. Torispherical dished end provides 4,7% higher volume than spherical dished end for the same length and diameter [23]. Equations that are used to calculate thickness of torispherical dished end are shown in chapter 2.1 with Equation numbers (9) and (10) which are represented by thickness t_2, and t_3. Thickness t_2 represents the spherical part with crown radius, and the torus part is represented by t_3, where the shape factor K is defined by iteration of the thickness using the graph from Pt.4. Ch.5, and by comparison with DNV strength analysis and PD5500.

Dished ends contain membrane and bending stresses. As primary bending stresses 1,5 f excludes discontinuities, and secondary stresses which occur at structural discontinuities caused by mechanical load, are applied for the knuckle area of the dished end with expression 3 f.

2.3 Stiffening ring

Stiffening rings at the place of support prevent longitudinal bending of the upper part of the cylinder. Horizontal tanks supported by saddles should be supported by two or more saddles supports according to DNV Pt.5Ch.7. For the calculation of the stiffening rings aligned with the center of the saddle support, the classification rule PD5500 is used, which is referred to by the DNV strength analysis.

According to PD5500 stiffener ring can be placed in the center of the saddle support or two stiffener rings can be placed for each side of the center line of saddle. As the bending is the state of stress, the main criteria how to dimension stiffener rings are limitless longitudinal and circumferential stress which appears in the four main point of the cylindrical shell and stiffener ring placed in the plane of saddle support shown by Fig. 3. At the Fig.3 f_4, f_3 represents longitudinal stresses at the cylindrical shell, f_7 represents circumferential stresses at the horn of the saddle, and f_8 circumferential stresses at stiffener ring in the plane of saddle. The given values of allowed stresses for each stress point is shown by Equations from (17) to (20). f_3, and f_4 are representing the longitudinal stresses, with limitation according to of design stress f. The numerical values of circumferential stresses *f7, f8* should not exceed 1.25 f according to PD5500.

$$f_3 = \frac{p_m * r}{2t} - \frac{M_4}{K_1 * \pi * r^2 * t} \quad (17)$$

$$f_4 = \frac{p_m * r}{2t} + \frac{M_4}{K_2 * \pi * r^2 * t} \quad (18)$$

$$f_8 = \frac{C_5 * K_7 * W_1 * r * d}{I} - \frac{K_8 * W_1}{a} \quad (19)$$

$$f_7 = \frac{C_4 * K_7 * W_1 * r * c}{I} - \frac{K_8 * W_1}{a} \quad (20)$$

Where C_4, C_5 are coefficient that could be -1 or +1; K_7, K_8 are coefficient depending on the ark of the saddle; I, a, c, d are geometrical characteristic of cross section of stiffener ring, W_1 is reaction force in one saddle support and M_4 *is* longitudinal bending moment at the place of the saddle support.

According to DNV strength analysis primary local and bending stresses are defined with Equation (21):

$$\sigma_L + \sigma_b \leq 1.5f \quad (21)$$

which is considered for the area of stiffener ring. Purpose of stiffener ring is to reduce stresses in the upper part of the cylinder above the saddle support.

2.4 Outer shell

Outer shell must resist bucking deformation which is a state of instability occurring in outer shell structure caused by difference of outside external pressure and inside the vacuum. The ratio, between designed external pressure p_{ed} and external critical pressure p_c, corresponding to elastic instability must be greater than 4, representing a safety factor for cylindrical shell:

$$\frac{p_c}{p_{ed}} >= 4 \quad (20)$$

Designed external pressure:

$$P_{ed} = P_1 + P_2 + P_3 + P_4 \quad (21)$$

where P_1 is vacuum relief valve, P_2 pressure relief valve, P_3 is pressure for a tank on exposed decks and P_4 is pressure compressive due to weight.

External critical pressure:

$$P_c = \frac{20E}{(n^2-1)\left[1+\left(\frac{n}{Z}\right)^2\right]^2}\frac{t_1}{D} + \frac{20E}{3(1-poison^2)}\left\{n^2 - 1 + \frac{2n^2-1-poison}{\left(\frac{n}{Z}\right)^2-1}\right\}\left(\frac{t}{D}\right)^3$$

(22)

where E is modulus of elasticity at room temperature in N/mm^2, L is effective length between stiffeners in mm, n is integral number of waves for elastic instability and Z is given as:

$$Z = \frac{0{,}5\pi D}{L}$$

The same equations (8) to (10) which are used for thickness of inside shell are used to determine the thickness of outside shell with only one thickness for cylindrical part because there are no tank segments because there is no influence of hydrodynamic pressure.

According to DNV structural global analysis acceptance criteria for a cylindrical shell for longitudinal stress compression should not achieve below buckling criteria:

$$\sigma_x \leq \frac{0.20E\,(t_1/R_c)}{1+0.004\frac{E}{R_{eH}}} \quad (25)$$

where σ_x is longitudinal stress compression.

Acceptance criteria for buckling strength assessment are given for membrane yield stress with Equations (24) and (25) for cylindrical part:

$$P_y = 20\frac{\sigma_F t_1}{D} \quad (24)$$

$$P_{ed} = \frac{P_y}{3} \quad (25)$$

Where σ_F is equal to yield stress and Py is external pressure corresponding to the membrane yield of the material.

According to DNV strength assessment dished end buckling capacity is given with Equation (26) and for membrane yield check Equation (27) is used.

$$P_c = 2.4E\left(\frac{t_2}{R}\right)^2 \quad (26)$$

$$P_y = 20\frac{\sigma_F t_2}{R} \quad (27)$$

Where t_2 is equal to torispherical part of dished end and R is equal to the outside crown radius of sphere.

2.5 Vacuum rings

Vacuum rings can be outside and inside of tank shell.

If the space between inner and outer shell is small position of the vacuum ring must be considered regarding to position of the pipes. Minimum moment of inertia is defined:

$$I_x = \frac{0.18\,D\,P_{ed}\,L\,\rho\,D_s^2}{10\,E} \quad (28)$$

where Ds is diameter of the neutral axis of the stiffeners.

If the vacuum rings are inside of shell, neutral ax will be closer to the centerline of tank thus the moment od inertia will be lower. Effective length between stiffeners is determined in previous chapter as a part of Z coefficient which is determined by critical pressure.

2.6 Saddle support

Saddle supports are part of the outer shell. Between inner and outer shell supports resistant to vacuum are placed in a plane of the tank saddle supports. One of the supports placed between tanks need to be fix in axal direction and another support is allowed to have axial displacement. Outer saddle supports which are welded for outer shell have one saddle support welded for the ship frame and other support is fixed with bolts for a ship structure.

According to DNV global design stress analysis shear stress in the cylindrical shell at the support should be by Equation (29)

$$\tau = 0.8\frac{R_{eH}}{\sqrt{3}} \quad (29)$$

Considering primary local membrane and bending stress 1,5f is applied.

3. Case Study

3.1 Ship and tank parameters

Ship main particulars for dual fuel engine cruise ship are given in Table 1. and center of gravity of the tank is given from the shipyard shown in Table 2. Maintaining values from given Tables 1. and 2. dimensionless acceleration components do to ship motions can be calculated according to IGC Rules and obtained results are given in Table 3.

Table 1: *Ship main particulars*

Parameter	Value
length on summer water line L_{WL}, m	256,4
breadth B, m	33,5
block coefficient C_B	0,6753
service speed V, kn	17

Table 2: *Center of gravity of the tank do to ship*

Parameter	Value
distance from amidship to the center of gravity of the tank; x, m	17,355
distance from the centerline to the center of gravity of the tank; y, m	4,5
distance from the ship's actual waterline to the center of gravity of the tank; z, m	1,9

Table 3: *Dimensionless acceleration components do to ship motions*

Parameter	Value
longitudinal acceleration, a_x	0,1161 g
transverse acceleration, a_y	0,4204 g
vertical acceleration, a_z	0,3845 g

Two tank type C are used as a storage tank of LNG for the dual engine cruise ship. The tank must be designed for the same volume capacity of 430 m^3 in available hull space. Main constraints due to geometry of the tank design are volume capacity of the tank, available hull section length 21600 mm, height 8700 mm, width 8700 mm, and 21 days of holding period without achieving BOG inside of tank. To achieve 21-day requirement insulation thickness is calculated to be 300 mm.

Constraints according to cryogenic conditions are satisfied by austenitic stainless steel. 304L is chosen for inside and outside shell where tensile strength Rm is 440 MPa, and yield stress is 180 MPa

by DNVGL-RU-SHIP-Pt2Ch2 [21]. Calculated design stress from mechanical properties is equivalent to membrane stress.

One component of inside tank design pressure determination is vapor pressure *Po* which is set equal to maximum allowable relief valve setting.

Working conditions of tank are limited to 90% of the value of the given vapor pressure which means that the maximum allowable working pressure of tank will be set to 8,1 bar. Tank properties are given in Table 4.

Table 4: *Tank properties*

Parameter	Value
Maximum allowable relief valve setting (MARVS), barg	9.0
Vacuum pressure for calculation, bar	1
Insulation thickness, mm	300
Nominal LNG temperature, °C	-163
Tank material	304L
Tensile strength Rm, N/mm^2	440
Yield strength $R_{eH0,2°}$, N/mm^2	180
Design stress f, N/mm^2	120
Modulus of elasticity at room temperature, N/mm^2	200000
Steel density, kg/m^3	7900

3.2 Results for inner tank

According to hull limited space dimensions of a tank are defined in Table 5.

Table 5: *Inner tank dimensions*

Parameter		Value
cylinder	**Inside**	**Outside**
length, mm	16500	17500
diameter, mm	5900	6500
dished end		
crown radius, mm	5900	6500
knuckle radius, mm	0,15D	0,15D

The cylindrical part of the inner shell is divided into 14 segments, and dished end to torispherical end and spherical dished end, where spherical and torispherical are divided into two more segments.

Dimensionless acceleration given from acceleration ellipsoid are calculated for beta angle 0 to 30 degrees. In the longitudinal plane, dimensionless acceleration can be calculated from 0 to 7 degrees, and for the transverse plane from 0 to 24 degrees. The product of the dimensionless acceleration of a specific angle beta and specific liquid height gives the hydrodynamic pressure for each segment of the tank. The highest pressure occurs in the longitudinal section of the tank due to the largest liquid highest thus for final pressure is taken as hydrodynamic pressure for longitudinal segments of the tank. Because of the tank symmetry calculation has been carried out only for half of the tank.

Tank segments and determination of liquid height for one of the segments is shown in Fig. 4. For each segments liquefied heights was calculated referring to the lowest point of the segment.

The same results for hydrodynamic pressure are obtained for symmetrical half of the tank thus the thicknesses are calculated only for one half of the tank. Obtained tank thicknesses for inner tank are shown in Fig. 5. where the cylindrical thickness is calculated from 25,9 mm to 26,4 mm, for torispherical part from 35,2 mm to 35,9 mm, and for spherical part from 25,8 mm to 26,3 mm.

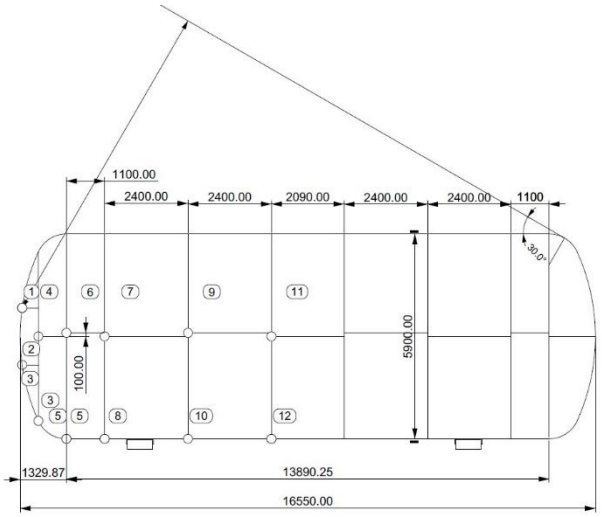


Fig. 4 *Segments of cylinder and dished end with liquid height*

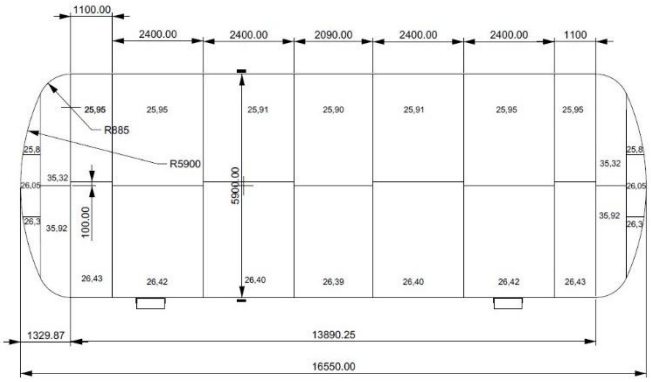


Fig. 5 *Thicknesses for inner tank segments*

3.3 Inner tank – thickness optimization, analytical and FEM results at the mid-span, at the saddle plane and primary and secondary **stresses**

Inner tank model consists of the cylindrical segment and a dished end. To be on the safety side of direct FEM calculation the lower thickness obtained from analytical results are applied for whole cylindrical inner tank, which is 25 mm for the cylinder, 36 mm for the torus segment of dished end, and 25 mm for the spherical segment of dished end. Plate elements are used for modeling, gravity load and liquid weight are included in FEM calculation. Mesh size of elements are 2t, two times thickness.

Analytical results according to PD5500 are represented with *f1, f2, f3, f4, f7* and *f8* where *f1* and *f2* are results referring to longitudinal stresses at the mid-span of the cylinder and *f3* and *f4* referred to longitudinal results at the upper and lower point at saddle plane, and *f7* and *f8* referred to circumferential stresses, where *f7* is stress at the horn of saddle and *f8* at the stiffener ring.

Calculated stresses according to PD5500 are compared with the results at the same point at the FEM model. Obtained stress results are shown in Table 6. for the stresses at the mid-span of the cylinder with the results according to PD5500.

Table 6: *Analytical and fem results for inner tank at mid-span*

stresses MPa	*f1*	*f2* ;	DNV
PD5500		57	63
FEM (Von Misses)	102	107	120
FEM (longitudinal)	52	53	/
FEM (hoop,top)	118	124	180
FEM (hoop,bot)	121	117	180

According to DNV strength calculation, design equivalent stress *f* is equal to Von Misses stresses which are 120 MPa, and circumferential stresses are *1,5 f* = 180 MPa, also longitudinal stresses are allowable to reach 0,8Reh = 144 MPa. All membrane stresses which are obtained at mid-span of an inner cylinder at the point *f1* and *f2* are acceptable, which means that the cylindrical part will not reach the yield point of the material. It is visible that the analytically obtained longitdinall streses are the same as given FEM results. Two times higher circumferential stresses above longitudinal are expected. Process of thickness iterations to satisfy the max. allowable stress provides single thickness for the whole cylindrical part of 25,5 mm. This iteration process of thickness reduces the mass of the tank and ultimately simplified the ordering of construction materials.

Analytical and FEM results for cylinder at the saddle plane are represented in Table 7. Coefficients C_4, C_5, K_7, K_8 are determined by arc of the saddle and position of the stiffener ring according to PD5500. All obtained results for *f3, f4, f7, f8* referred to the arc of the saddle at 120 degrees and stiffener ring in the plane of the saddle. Results are given for the half of the tank where the saddle is not fixed in the axial direction. Results obtained for the cylinder without a stiffener ring at the saddle plane are given in Table 8.

Table 7: *Analytical and fem results at inner cylinder in the saddle plane and at stiffener ring*

stresses MPa	*f3*	*f4*	*f7*	*f8*
PD5500	65	62	-83	101
FEM (Von Misses,top)	59	95	72	
FEM (Von Misses,bot)	123	176	92	
FEM (longitudinal,top)	-34	-108	/	/
FEM (longitudinal,bot)	141	201	/	/
FEM (hoop,top)	/	/	81	/
FEM (hoop,bot)	/	/	96	/
FEM (beem stress) /	/	/	64	

Cylindrical part obtains membrane stresses which can be longitudinal and circumferential. Considering primary local membrane discontinuities where *1,5f* is allowed, which is 180 MPa, it is acceptable to have differences in top and bottom longitudinal stresses at the upper point *f3* and *f4* at the plane of the saddle support. Differences in the top and bottom stresses refer to the fact that bending stresses have occurred, which is also accepted while the primary bending stress are limed to 180 MPa. The result for PD5500 is valid only for longitudinal stress *f3*, *f4* but the area with the stiffener ring is obtaining longitudinal and bending stresses, therefore the stresses obtained by FEM are much higher regarding to analytical results. Longitudinal stresses *f3* at the top of the cylinder in the plane of the saddle without stiffener ring provides results that are closer to obtained analytical stress according to PD5500. Membrane circumferential stress or hoop stresses *f7* at the point of the horn of the saddle with the stiffener ring gives a similar value to analytical calculations.

Table 8: *Analytical and fem results at inner cylinder in the saddle plane without stiffener ring*

stresses MPa	*f3*	*f4*	*f7*
PD5500	65	62	-83
FEM (Von Misses,top)	105	119	108
FEM (Von Misses,bot)	101	176	104
FEM (longitudinal,top)	57	-134	/
FEM (longitudinal,bot)	56	201	/
FEM (hoop,top)	/	/	124
FEM (hoop,bot)	/	/	120

Without a stiffener ring, it is visible from table 8. that Von Mises top and bottom are the same for the upper part of the cylinder, the same is valid for the longitudinal top and bottom stresses. At point *f4*, longitudinal stresses for the lower part of the vessel at the place of support reach a smaller value, but the bottom Von Mises is higher comparing to the stresses when the stiffener ring is used. Referring to circumferential stresses at point *f7* it is visible that the stiffener ring reduces stresses at the point of the saddle horn.

While the Table 6. Table 7. and Table 8. represents comparison between analytical and direct calculations for specific point at the cylinder, Fig. 5, Fig.6, Fig.7, Fig.8, Fig.9 and Fig.10 shows stresses obtained only by FEM calculations. Obtained stress in all figures shows stress distribution in the x-z plane for upper half of the tank and for lower half of the tank.

All figures from Fig.5 to Fig. 10 have on the x-axis element positions in FEM which depends on geometry, and on the y-direction assigned stress for a certain element position. Elements includes spherical, torspherical and cylindrical part of the geometry. Cylinder part is in the range of 1330 mm to 8500 mm, the area between 3000 mm and 4000 mm represents constraints regarding to saddle supports, and from 4000 mm to 0 element position is area of small cylindrical and toprsphericla dished end at the x-axis of the graph. Tis figures provides us understanding of primary and secondary stress and where is the stress limits. Since the stresses are shown for the plane it is possible to read FEM results relating to positions *f1, f2,f3,f4*. Top and bottom stress are extracted for longitudinal and circumferential stress on each Fig. When top and bottom stress are overlapping it is the area of membrane stress, referring to the cylindrical part where max. allowable stress are defined up to 120MPa. When the top and bottom stress lines started to divergence it is the because the bending stress started to occur. Combined analytical bending and local membrane stress are allowed up to 180MPa which refers to the area around saddle or stiffener rings. Combined local, membrane and bending stress are considred primary stress.

Fig.6, Fig.7, Fig.8, and Fig 9. represents circumferential and longitudinal stress for lower and upper half of the tank where it is visible that circumferential stresses are two times higher than longitudinal stresses. Fig.10 and Fig 11. represents VonMises stresses for the lower and upper half of the tank with and without stiffener ring.

The dished end is considered as secondary stress including discontinuities which allows us to have stress up to 360 MPa.

It is wisible from the figures that primary and secondary streses satisfy.

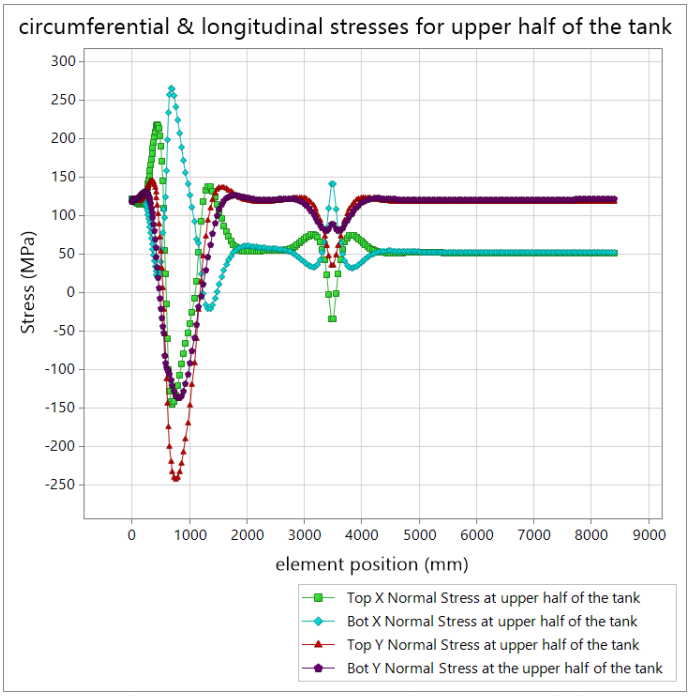


Fig. 6 *circumferential and longitudinal stress for the upper half of the tank, with stiffener ring*

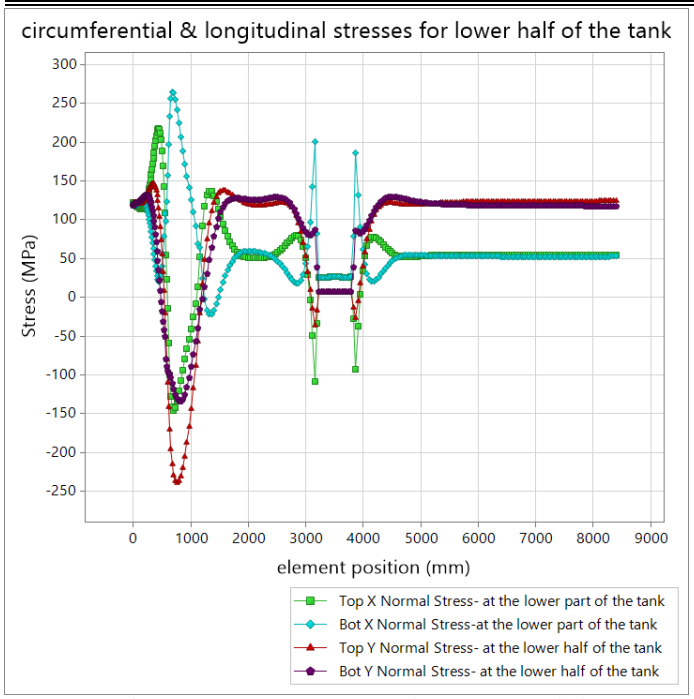


Fig. 7 *Circumferential and longitudinal stress for the lower half of the tank, for x-axis, is sliding, with stiffener ring*

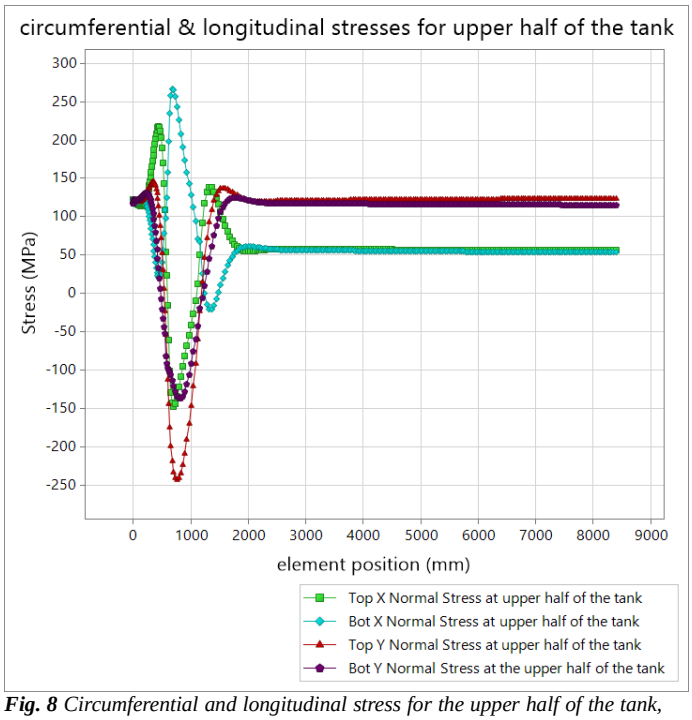


Fig. 8 *Circumferential and longitudinal stress for the upper half of the tank, for x-axis is sliding without stiffener*

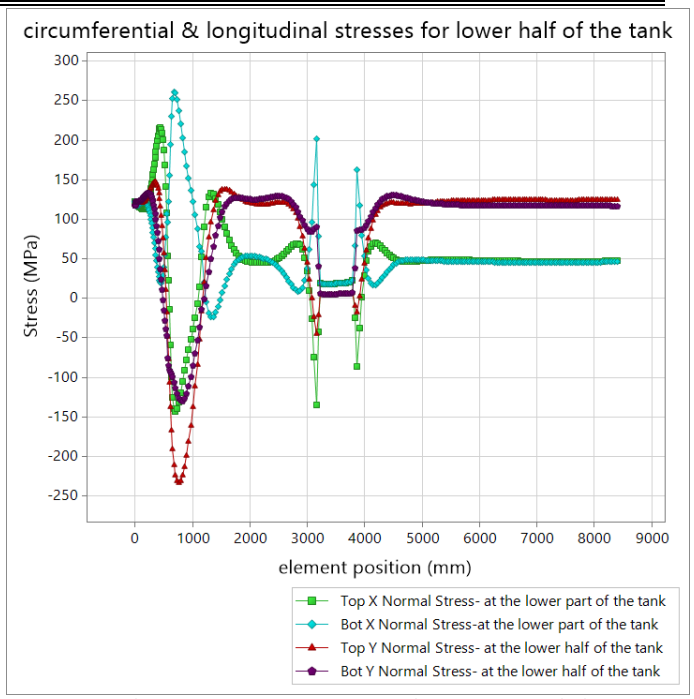


Fig. 9 *Circumferential and longitudinal stress for the upper half of the tank, for x-axis, is sliding without stiffener*

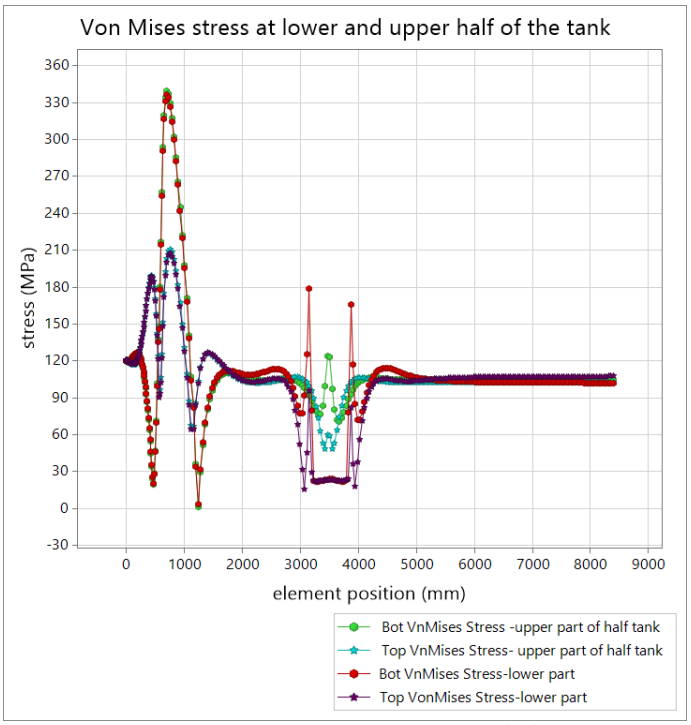


Fig. 10 *Von Mises stresses at the lower and upper half of the tank with stiffener ring*

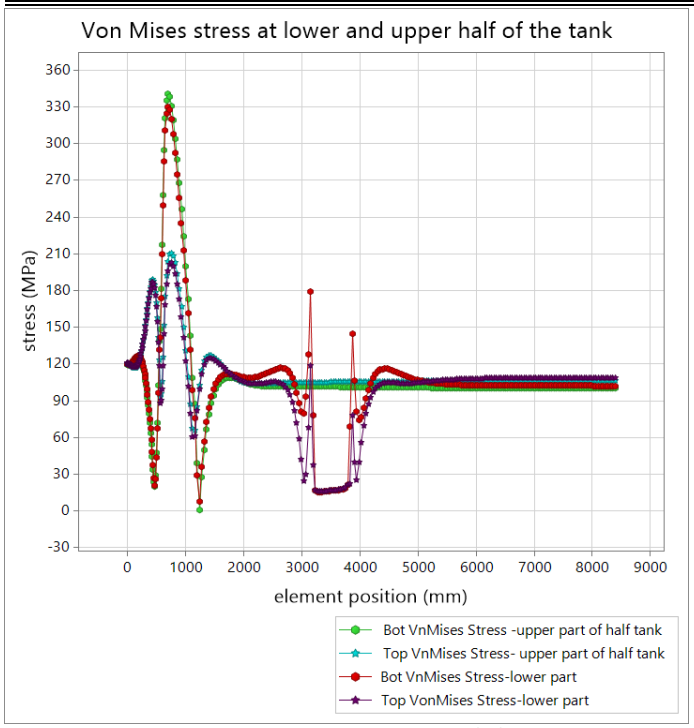


Fig. 11 *Von Mises stresses at the lower and upper half of the tank without a stiffener ring*

Figure 12. and Figure 13. represents circumferential streses for x-y plane with and without stiffener ring.

It is visible much clearer from Figure 12, and Figure 13, that circumferential stresses are reduced when stiffener ring is used from 190 MPa to 104 MPa pointing to the the highest stresses at the whole circle, not at one point.

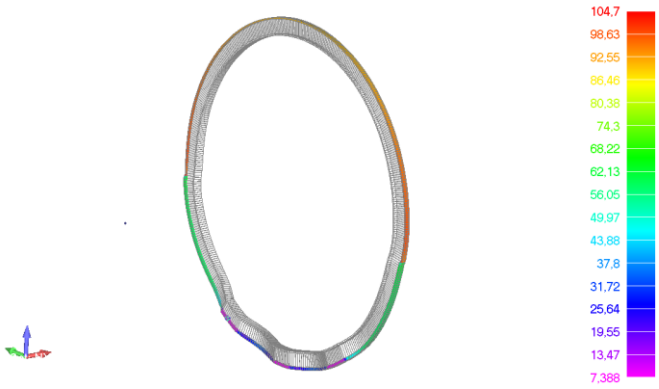


Fig. 12 *Bottom y-nominal stress for cylinder in the plane of the saddle with stiffener ring*



Fig. 13 *Bottom Y-Nominal Stress For Cylinder In The Plane Of The Saddle Without Stiffener Ring*

3.4 Inner tank- three Durolight supports between inner and outer shell

Between inner and outer shell there is perlite and a vacuum space. Durolight has very good behavior inn vacuum. Three durolight box are fixed for one side of the shell at the place of sliding support and at the place of fix support it is fixed for inner and outer shell. In the contact between inner cylindrical tank and durolight boxes, double plate should be paced calculated according to the rules. Fig.14, Fig.15, Fig.16 and Fig.17 represents segments of the inner tank with and without ring in the plane of the saddle support, with double plate, given loads and constraints for fixed and sliding supports.

Results for longitudinal and circumferential stresses in the plane of the saddle are obtained for available axial direction, and all other 5 degrees of freedom are fixed. To compare analytical and FEM results for shear stress the larger value of shear is achieved when all six degrees of freedom are achieved. Limitations for shear stress according to DNV stress analysis are given in chapter 2.5. Saddle support and its value is 83,14 MPa.

The cylindrical shell has a double plate with the same thickness as the cylinder shell and the same element is used for that area times double because the cylinder is 25 mm, and the double plate is also 25 mm. The double plate is fixed at three main supports to evaluate shear stress when the axial direction is allowable and when not, referring to sliding and a fixed support. Shear stresses are compared with stiffener rings and without.

Figure 14. and Figure 15. are representing max shear stresses for when an axial direction is allowable and the other 5 digress of freedom are fixed with and without a stiffener ring. Figures 16. and 17. representing max. shear stresses when the saddle is fixed, all 6 degrees of freedom are unable. It is visible that the stiffener ring reduces stresses shear stresses near the saddle by 42% when sliding support is used and 23 % when fixed support is used.

Although the shear stresses are reduced in the plane of the saddle with a stiffener ring, the value of 90 MPa shear stress when the support is fixed it is above the limit of 83,41 MPa according to DNV for global stresses at cylinder for shear stress at support. Shear stresses are acceptable for sliding support but not for fixed support.

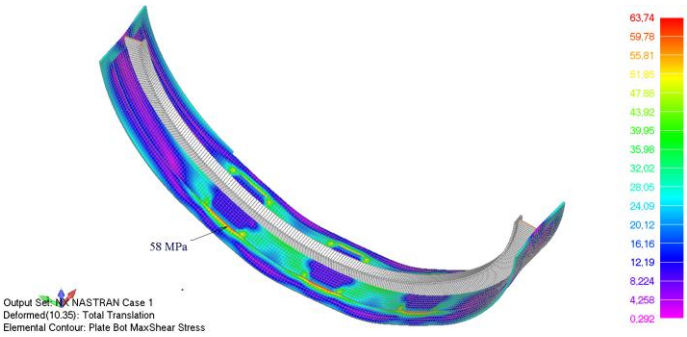


Fig. 14 *Plate Bottom Maxshear Stress In The Area Of The Double Plate With Stiffener Ring At The Sliding Support*

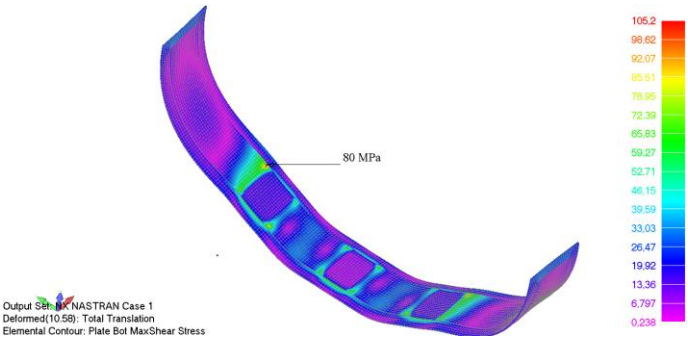


Fig. 15 *Plate bottom Maxshear stress in the area of the double plate without stiffener ring at the sliding support*

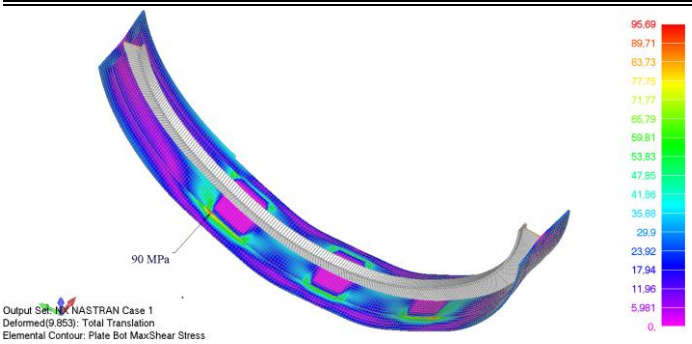


Fig. 16 *Plate bottom MaxShear stress in the area of the double plate without stiffener ring at the fixed support*

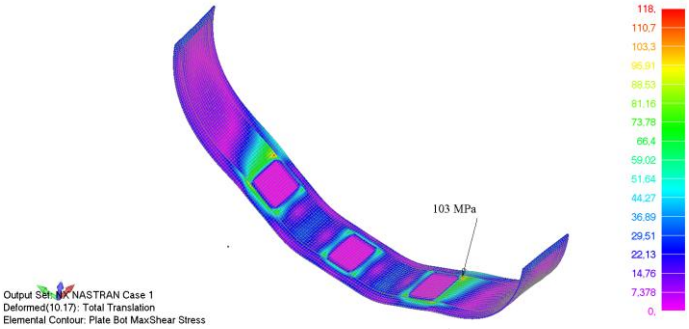


Fig. 17 *Plate bottom MaxShear Stress in the area of the double plate without stiffener ring at the fixed support*

This saddle support area is considered to have a primary local membrane and bending stress which is allowed to reach equivalent von mises stress of 1.5*f* which is 180 MPa. Table 9. represents circumferential and Von Mises stress where is visible that the DNV criterion of 1,5*f* is reached, therefore three supports do not satisfy, and therefore the number of supports should be increased.

Table 9: *Analytical and fem results at the inner cylinder in the saddle plane for sliding support*

stresses MPa	with ring	without ring
DNV, shear	83	83
DNV, $\sigma_L + \sigma_b$	180	180
FEM (MaxShear,bot)	63	105
FEM (hoop,bot) 101	165	270
FEM (Von Mises,bot)	189	248

Table 10: *Analytical and fem results at the inner cylinder in the saddle plane for fixed support*

stresses MPa	with ring	without ring
DNV, shear	83	83
DNV, $\sigma_L + \sigma_b$	180	180
FEM (MaxShear,bot)	90	118
FEM (hoop,bot) 101	180	227
FEM (Von Mises,bot)	245	268

3.5 Outer shell – thickness optimization and analytical and FEM results

The main issue to calculate inner tank thickness was defining MAWP. For the outer shell, there was no problem defining MAWP because it defines as 90% of the vapor pressure value, which is given by the producer, but for the inner shell, the problem in definition occurred. Designed external pressure is determined by four pressures, where one of the pressures refers to PRV (pressure relief valve). Pressure relief valve P_2 is taken as 0 when the tank is putted in open space, and P_2 is equal to PRV for closed space when tank is placed inside of the hull. PRV must not be higher than the vapour pressure, which means that it can be equal to the vapour pressure (MARVS) in the design of the tank when the one relief valve is used. According to DNVGL-RU-SHIP-Pt5Ch7 [18] when two or more pressure relief valves are fitted one pressure relief valve is sat to 50% of total relieving capacity and the other is 5% above MARVS. Table 5. represents obtained values according to DNV rulesPt5Ch7 [18].

Table 11: *Designed external pressure components*

Parameter	Value, bar
P_1	0,25
50%P_2	4,5
5%P_2	9,45
P_3	0
P_4	0,05

Therefore, depending on the number of pressure relief valves there is a big difference to get designed external pressure and ultimately a big difference in the thickness of the wall itself represented in table 12.

Table 12: *Thickness of outer shell for two PRV*

PRV	5%MARVS	50%MARVS
P_{ed}, bar	9,75	4,8
cylinder part, t1, mm	26,51	13,03
spherical part, t2, mm	26,46	13,01
torispherical part, t3, mm	34,51	17,08

DNV strength analysis mentioned that the point of the relief valve has normally been used in the range of about 4 bars. Usually, for such a tank two relief valves are used and regarding those further calculations are maintained with external design pressure equal to 4,8 bar.

Thicknesses in table 12. are calculated using the thickness equations for inner shell. If this thickness is applied to calculate external pressure corresponding to a membrane yield P_y for cylindrical part and dished end for yield stress 180MPa and given values of P_y divided with safety factor 3 given values should be equal or higher than Ped, external design pressure. This iteration process gives values for t_1 = 26,21 mm for cylindrical shell and, t_2 = 36 mm for torspherical part of dished end with external buckling critical pressure for dished end P_c=14,4 bar.

To calculate external bucking critical pressure for cylindrical part number of waves n should be iterated until the smallest but acceptable bucking critical pressure P_c is reached, where the ratio P_c/P_{ed} must be equal or larger than 4, for cylindrical part.

Critical bucking pressure for cylindrical part is obtained P_c=19,36 bar for n=11 which is visible in Figure 18.

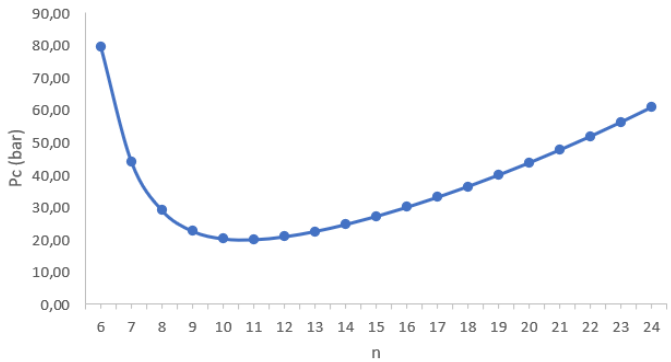


Fig. 18 *Buckling pressure for cylindrical part*

Effective length between stiffeners for Figure 19. is 2200 mm. The length of the cylinder part of outer shell is 14219 mm, and the number of vacuum rings is 6,5. To have 7 vacuum rings the length between stiffeners is reduced to 2000 mm but the number of waves remains the same n= 11, and critical bucking pressure is on safety side with P_c= 21,87 bar.

Vacuum rings are placed from the inner side of the outer shell because moment of inertia is highly reduced because of diameter of the neutral axis of the stiffeners is smaller when it is from the inner side.

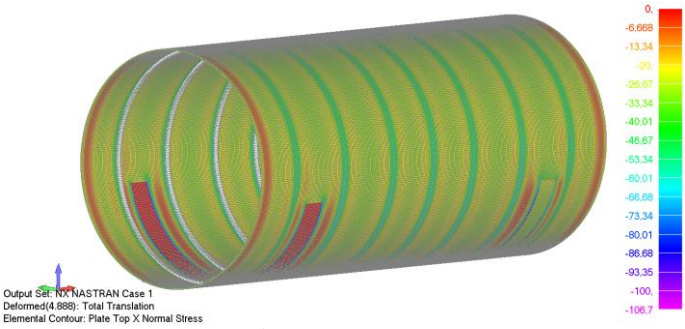


Fig. 19 *Longitudinal stresses for cylindrical outer shell*

Longitudinal stress (compression) for cylindrical shell should not reach 60 MPa according to the DNV strength calculation rules.

Figure 20. shows satisfaction of primary and secondary stresses.

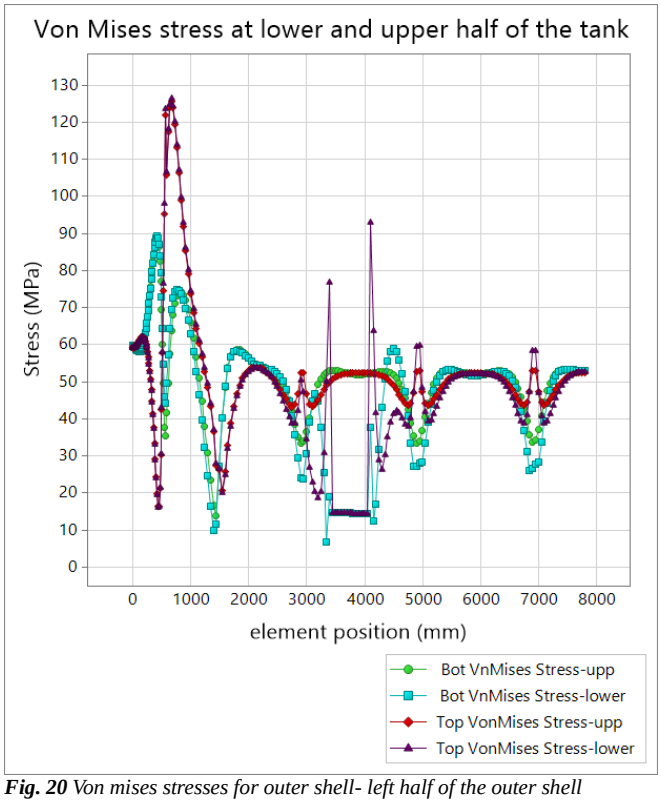


Fig. 20 *Von mises stresses for outer shell- left half of the outer shell*

4. Conclusion

Analytical calculations according to DNV-GL standards and analytical calculations for specific points regarding to British standard PD 5500 combined with FEM stress calculations provide next insight for

Inner shell:

- obtained results for analytical longitudinal stresses at the mid- span of the cylinder are close to stress obtained in FEM calculations.
- analytical obtained smallest value was used for inner tank thickness which satisfied primary and secondary stress and leads to one thickness dimension of inner tank and reduces higher thicknesses and larger number of segments
- reducing the thicknesses of the inner layer results in a reduction in the time required to calculate the hydrodynamic pressure, facilitates the procedure of ordering the material, and ultimately reduces the mass of the material.
- inner cylinder thickness reduced to 25 mm
- circumferential analytical stress *f7* at the horn of the saddle provides accurate results compering to FEM analysis with or without stiffener.
- longitudinal analytical stress *f4* and *f3* in the plane of the saddle are very different from FEM analytical stress analysis

Outer shell:

- iteration proses has been made to satisfied the pressure criteria which result in negligible thickness iteration
- analytical

Number of supports between two shells need to be increase referring to primary and secondary stress.

Several issues are appearing in this paper:

- The terminology from different DNV-GL Rules is not always unambiguous. It is problem to distinguish when primary and secondary stress is applied, on which segments of the tank, therefore it is not easy to the validate results obtained from Rules to direct FEM calculation.
- Inside of the Rules is not briefly explained the situation with the double shell, and which are the critical area to consider between inner and outer shell.
- Rules don't say clearly when Dimensionless accelerations are not mandatory for calculations which will save a lot of time. A basic understanding of design of LNG tank type C is given in this paper with the possibilities for a future extension on other details.

ACKNOWLEDGEMENTS

The project is supported by European Regional Development Fund, project IRI 5 (Research, Development, and Innovation)-Center of competence for advanced mobility DIV, Zagreb.

REFERENCES

[1] IMO International Code of Safety for Ship Using Gases or Other Low-flashpoint Fuels (IGF Code), (2015)

[2] Tommaso Iannaccone, Gabriele Landucci, Alessandro Tugnoli, Ernesto Salzano, Valerio Cozzani, Sustainability of cruise ship fuel systems: Comparison among LNG and diesel technologies, (2020)

[3] Ole.Vidar.Nilsen, LNG regulatory update, DNV-GL, (2018)

[4] American Bureau of Shipping, Strength Assessment of Independent Type C Tanks, (2022)

[5] Heewoo Park, Jinseong Park, Jong-Rae Cho, Evaluation of Insulation Performance and Structural Integrity of an IMO Type C LNG Storage Tank
https://doi.org/10.14775/ksmpe.2021.20.07.001

[6] Banaszkiewicz T, Chorowski M, Gizicki W, Jedrusyna A, Kielar J, Malecha Z, Piotrowska A, Polinski J, Rogala Z, Sierpowski K, et al. (2020). Liquefied natural gas in mobile applications—opportunities and challenges. Energies. 13(21):1–35. https://doi.org/10.3390/en13215673

[7] IMO International code for the construction and equipment of ships carrying liquefied gases in bulk (IGC Code). London, (2016)

[8] J Harperscheidt , Bunkering, infrastructure, storage, and processing of *LNG* - Ship & Offshore, (2011)

[9] Yan Lin, Chao Ye, Yan-yun Yu, Shi-wei Bi, n Approach to Estimating the Boil-Off Rate of LNG in Type C Independent Tank for Floating Storage and Regasification Unit under Different Filling Ratio, (2018)
https://doi.org/10.1016/j.applthermaleng.2018.02.066

[10] Cheng Wang, Yonglin Ju, Yunzhun Fu, Dynamic modeling and analysis of LNG fuel tank pressurization under marine conditions, (2021)
https://doi.org/10.1016/j.energy.2021.121029

[11] Sixian Wu, Yonglin Ju, Numerical study of the boil-off gas (BOG) generation characteristics in a type C independent liquefied natural gas (LNG) tank under sloshing excitation, (2021)

[12] Bo Wang, Yung-Sup Shin, Eric Norris, strength assessment of type 'C' LNG fuel tanks, (2015)

[13] Bo Wang, Xiaozhi Wang, Yung-Sup Shin, structural integrity assessment of independent type 'C' LNG carriers, (2014)

[14] Ivo Senjanović, Vedran Slapničar, Zoran Mravak, Smiljko Rudan & Ana Maria Ljuština, structure design of cargo tanks in liquefied gas carriers

[15] David Nash, Differences Between EN 13445 and Other International Standards, (2008)
https://doi.org/10.1115/PVP2003-1794

[16] Young-IL Park, Jin-Seong Cho and Jeong-Hwan Kim, Structural Integrity Assessment of Independent Type-C Cylindrical Tanks Using Finite Element Analysis: Comparative Study Using Stainless Steel and Aluminum Alloy, (2021)
https://doi.org/10.1016/j.energy.2021.120001

[17] DNV No .31.13 Strength analysis of independent type C tanks, 2016

[18] DNVGL-RU-SHIP-Part5 Chapter7 Liquified gas tankers, 2017

[19] DNVGL-RU-SHIP-Part4 Chapter7 Pressure equipment, (2017)

[20] DNVGL-RU-SHIP-Part5 Chapter5 Liquified gas

[21] DNVGL-RU-SHIP-Part2 Chapter2 Metallic materials, (2017)

[22] IMO. International code for the construction and equipment of ships carrying liquefied gases in bulk (IGC Code). London,2016

[23] John Kokarakis, Standards and Guidelines for Natural Gas Fuelled Ship Projects, 2015

Example of the maintenance of a machine pero (D 2504-019) for cleaning metal parts in the working conditions of OEM company from the autotive industry

Ismar Alagić
International University of Sarajevo, Hrasnička cesta 15, 71210 Ilidža - Sarajevo, Bosnia and Herzegovina
E-mail: ismar.alagic@gmail.com; ialagic@ius.edu.ba

Abstract: *In this article, it will present a example of the maintenance of a machine PERO (D 2504-019) for cleaning metal parts in the working conditions of renowned OEM company in producing filters from automotive industry. The maintenance process is of particular importance in order to use production capacities to the maximum extent. Maintenance is an indispensable segment of any production system. It follows that maintenance should be adapted to these conditions, and be economical and efficient, so as not to slow down the progress of the production system. Various maintenance methods have developed alongside the development of technology, all with the aim of increasing efficiency and reducing costs. This entails the need for increasing knowledge and skills of the workers themselves in the maintenance system. Large sums of money are invested in modern industry, in order to prevent monetary losses caused by system failures. If the machine tools, devices, and accessories are not maintained on time and adequately, there will be a stoppage of production, which is extremely inconvenient for the company. When the machine stops, delivery is delayed, which leads to a psychological effect on the worker, who is then put under pressure to make up for lost time. In this article, the whole procedure of cleaning, mantenance and inspection of machine PERO (D 2504-019) through 13 steps has been studied. The indicators of the reliable operation of the analyzed machine through the analysis of the machine's operation, the analysis of downtime, and the analysis of the occurrence of failures through the obtained values of MTTR (Mean Time to Repair) and MTBF (Mean Time Between Failures) are presented in details.*

KEYWORDS: *MAINTENANCE, MACHINE PERO (D 2504-019), CLEANING, FILTERS, MTTR (Mean Time to Repair), MTBF (Mean Time Between Failures).*

1. Introduction

In this paper, we will present an example of the maintenance of a machine for cleaning metal parts from the machinery park of the company Mann Hummel BA in Tešanj. MANN+HUMMEL BA is a development partner and series supplier to the international automotive and mechanical engineering industry. The company's production in Tešanj (Bosnia and Herzegovina) started in 1974 on the basis of a licensed contract with the MANN+HUMMEL company from Germany. The company's products include air filtration systems, intake systems, fluid filtration systems, cabin filters and engine head covers made of plastic with a high degree of integration for the automotive industry, as well as elements for maintenance and repair of trucks. Production took place on the basis of a license agreement with the MANN+HUMMEL company from Germany until 1989. After the termination of the license agreement, the development of its own brand takes place, which is named "UNICO FILTER". The brand "UNICO FILTER" was primarily intended to meet the needs of the market of the former Yugoslavia, later it became recognizable much more widely, in Russia, Albania, Ukraine, Bulgaria, Greece and the Czech Republic, and as such occupies an important place in the part of Southeast Europe. Due to the specificity of the product, the materials for the production of filters (sheet metal and paper) are procured from abroad, while the packaging materials are used mainly from Bosnia and Herzegovina, and in this way every year an increasing number of local suppliers are helped to develop and their quality system reaches a level that corresponds to MANN+HUMMEL. About 90% of the material is imported from Germany. In general, the biggest customer of MANN+HUMMEL BA for the last 20 years is Volkswagen. Apart from them, there are other well-known manufacturers of cars and trucks such as Mercedes, KHD/DEUTZ and others. For product validation, MANN+HUMMEL BA uses its own laboratory, which is equipped with modern devices for functional testing of oil, fuel and air filters, as well as the testing and development of materials that are installed in these filters. The MANN+HUMMEL BA laboratory is part of the global MANN+HUMMEL test network, which enables access to special "tailor made" test devices. It also provides testing services using its own resources to all locations of the MANN+HUMMEL Group. Experienced engineers on test procedures in cooperation with development engineers define the test parameters, and through the product validation process ensure that the product provides the filter function during use in extreme conditions [1].

The company PERO (Peter Erbel Reinigungsanlagen und Oberflächentechnik-Peter Erbel cleaning systems and surface technology) founded in 1953 in Königsbrunn near Augsburg, Germany, is a leading manufacturer of parts cleaning systems supplying companies in many different industries - automotive, aerospace, etc. Many industries specialized in cutting and deformation processing clean their product parts in PERO units, and this is also the case with MANN+HUMMEL BA, which owns one such machine. The maintenance of the PERO AG machine itself will also depend on the further quality of the cleaned product parts in it, which are further used in the assembly of the finished filter product. The maintenance process is of particular importance in order to use production capacities to the maximum extent. Maintenance is an indispensable segment of any production system. It follows that maintenance should be adapted to these conditions, and be economical and efficient, so as not to slow down the progress of the production system. Various maintenance methods have developed alongside the development of technology, all with the aim of increasing efficiency and reducing costs [2]. This entails the need for increasing knowledge and skills of the workers themselves in the maintenance system. Large sums of money are invested in modern industry, in order to prevent monetary losses caused by system failures. If the machine tools, devices, and accessories are not maintained on time and adequately, there will be a stoppage of production, which is extremely inconvenient for the company. When the machine stops, delivery is delayed, which leads to a psychological effect on the worker, who is then put under pressure to make up for lost time. Very often, maintenance is reduced to corrective maintenance, i.e. maintenance when the machine stops, instead of preventive maintenance. This especially applies to large plants that have high-volume production, because they cannot afford to stop production [3]. The costs of regular service are much cheaper than stopping the entire production and waiting for the defect to be fixed. Sometimes it takes up to 3 months to get a new replacement part, so you should always plan in time to avoid delays. A large part of failed plants happened precisely because of inadequate maintenance, and many of them were greatly contributed by bad management. Machines should be maintained according to the manufacturer's recommendations and according to the annual maintenance plan. All machine repairs should be properly recorded, and all inspections and repairs should be performed according to elaborate technological procedures. The technical maintenance service forms a maintenance team depending on the type of failure. It is very important that the maintenance is approached conscientiously in order to maintain the planned production, as well as the operational stability of the production plant [4].

2. The whole procedure of maintenance of machine PERO (D-2504-019)

As already mentioned, MANN+HUMMEL BA has a PERO machine model (D 2504-019) intended for cleaning parts of metal products, shown on Figure No. 1 [1].



Fig. 1. *Examples of learning from nature.*

The maintenance of this machine is presented in the work order for TPM (Total Productive Maintenance) monitoring shown on Figure No. 2, which contains a detailed explanation of the maintenance actions on each machine [1].

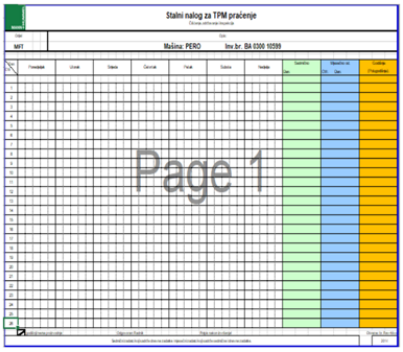


Fig. 2. *Example of work order for TPM monitoring.*

This order includes cleaning, maintenance and condition monitoring. In addition to the above actions that were carried out in the maintenance process, the order contains:
- type of machine being maintained (model and series),
- the department to which the machine belongs,
- the time period when the examination should be performed,
- daily/weekly/monthly/yearly overview overview,
- the person/worker responsible for the inspection.

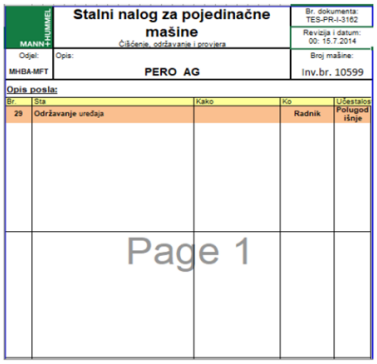


Fig. 3. *Example of work order for individual machine.*

In addition to the permanent order for TPM monitoring, there is also an order for monitoring the maintenance and condition of each machine, presented in figure 3. In this order, the steps for each part on which maintenance was carried out and how it was done are explained in detail.

3. Cleaning, maintenance and inspection of machine PERO (D-2504-019)

The entire cleaning, maintenance and control procedures of the machine PERO AG model D 2504-019. we will explain in thirteen steps.

a) **Solvent check** – the agent used to clean the parts of the product in the machine as shown in Figure 4. Inspection is performed as follows: temperature check, pH value check; solvent check after introduction of consumables that boil with solvent, and; solvent check after introduction of consumables that foam with solvent. Frequency of checking: on a daily basis, before starting the machine. The check is performed by: the worker.





Fig. 4. *Solvent check.* ***Fig. 5.*** *Checking the tightness of all parts.*

b) **Checking the tightness of all parts through which the solvent flows**, as shown in Figure 5.
Control is performed visually as follows: tank check; checking the water separator; checking capacitors; checking pipe connections, and; checking the flanges. Frequency of checking: on a daily basis, before starting the machine. The check is performed by: the worker.
c) **Checking the filter**, as shown in Figure 6. Inspection is performed visually, followed by: filter cleaning, and; filter replacement as needed. Frequency of checking: on a daily basis, before starting the machine. The check is performed by: the worker.
d) **Lubrication of the bearings**, as shown in Figure 7. The inspection is performed as follows: the bearings of the rotating device are lubricated; means used for lubrication: grease LITMA 2EP. Frequency of checking: on a daily basis, before starting the machine. The check is performed by: the worker.





Fig. 6. *Checking the filter.* ***Fig.7.*** *Lubrication of the bearings.*

e) **Checking the temperature**, as shown in Figure 8. Temperature control is performed visually as follows: due to the heating of the device, check the temperature of the solvent. Frequency of checking: on a daily basis, before starting the machine. The check is performed by: the worker.
f) **Inspection of the aeration lines**, as shown in Figure 9. The control is performed visually in the following way: the concentration of exhaust air must be checked behind the aeration filter for liquid air. Frequency of checking: on a daily basis, before starting the machine. The check is performed by: the worker.





Fig. 8. Checking temperature. **Fig.9.** Inspection of the aeration lines

g) **Maintenance of the chamber door**, as shown in Figure 10. The control is performed visually in the following way: the concentration of exhaust air should be checked behind the air filter for liquid air. Frequency of checking: on a daily basis, before starting the machine. The check is performed by: the worker.
h) **Maintenance of the addition unit**, as shown in Figure 11. Maintenance control of the addition unit is performed as follows: clean the addition area, and; remove shavings and oil residues.

Frequency of checking: on a weekly basis, before starting the machine. The check is performed by: the worker [1].



Fig. 10. *The chamber door .*



Fig.11.*The addition unit.*

i) **Water separator maintenance**, as shown in Figure 12. Water separator maintenance control is performed as follows: clean the water separator,i; check consumable anode and zinc wire. Frequency of checking: monthly, before starting the machine. The check is performed by: the worker.

j) **Maintenance of the sound generator**, as shown in Figure No.13. Maintenance control of the sound generator is performed as follows: clean the suction network of the ultrasound generator. Frequency of checking: monthly, before starting the machine. The check is carried out by: an engineer from the maintenance service [1].



Fig. 12. *The water separator.*



Fig.13. *The sound generator*

k) **Maintenance of the pneumatic cylinder**, as shown in Figure 14. Control of the maintenance of the pneumatic cylinder is performed as follows: tighten the counter nuts of the cylinder handles, and; check the efficiency of the cylinder switches, adjust them if necessary. Frequency of checking: annually, before the start of machine operation. The check is carried out by: an engineer from the maintenance service.

l) **Dryer maintenance**, as shown in Figure 15. Dryer maintenance control is performed as follows: open and clean the dryer, i; clean the cooling fins. Frequency of checking: annually, before the start of machine operation. The check is performed by: the worker.



Fig. 14. *Pneumatic cylinder.*

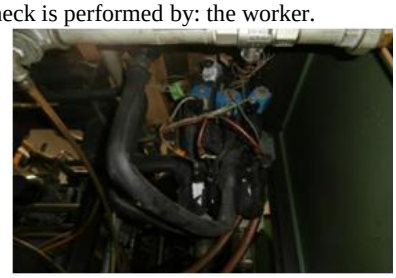


Fig.15*. The Dryer.*

m) **Maintenance of the analyzed device**, as shown in Figure 16. Maintenance control of the analyzed device is performed as follows: clean all surfaces of the device, and; after cleaning, lubricate the bearings and guides. Frequency of checking: annually, before the start of machine operation. The check is performed by: the worker [1].



Fig. 16. *The machine PERO (Model D2504-019).*

After the maintenance has been performed, the confirmation of the execution order is approved by the technical service, that is, personally by the head of the maintenance service, and the same is entered into the SAP system and stored in the database. In this way, by entering data on the performed maintenance for each machine at any time, we have an insight into the performed maintenance of an individual machine, as shown in Figure No. 17 [1].



Fig. 17. *Work orders list from SAP ERP system.*

Figure No. 17 shows the order for preventive maintenance in the month of December 2020. The PM order is made up of a list of orders for individual machines/equipment. The above list consists of the following data[1]:

-the main work center where the machine/equipment that needs to be maintained is located;
-the start date of the maintenance procedure;
-type of machine/equipment (L00002-GUSBI, L00228-CIRCULAR PRESS EHA 3213, etc.);
-short text about the machine/equipment;
-system status (OTP, PRT, NMAT, POKR, PROB);
-maintenance plan for each machine individually (L00002-03, L00228-00, etc.);
-machine/equipment location;
-total planned costs and;
-total actual costs.

In this way, by entering all the data, you always have an insight into the state of maintenance of each machine/equipment.

4. The indicator of reliable operation of the analyzed machine

Machine breakdowns happen sooner or later, it is important that we are prepared for them when they happen unexpectedly. The breakdown can be partial or it can be a complete breakdown of the machine, basically a breakdown is any event that prevents the machine from fulfilling its function. Eliminating defects significantly reduces their impact on the production process and costs. In order to effectively solve malfunctions, there are certain calculations that we use to monitor the state of the machines. Understanding the calculation method eliminates the need to guess the condition of the equipment and provides management with the information needed to make business decisions. For quality results, it is necessary to collect reliable data about the operation of the machines beforehand. Indicators of successful machine operation are important for any production-oriented company. Monitoring equipment reliability is a daily requirement of every maintenance department. Recording and monitoring of failures is useful, so the same is implemented in the MANN+HUMMEL BA company, which we will present in the following excerpts, as shown in Figure No.18 [1].

BMV	Prematic	Jelsingrac	DRS160	DRS400	PEE250	PEE250-Zilha	Record	Schuller	Ukupno
3:45:55	10:49:30	0:19:50	0:00:00	0:53:47	0:21:04	0:00:00	4:50:30	0:16:36	52:42:39
5:27:46	7:43:28	0:18:39	0:20:40	0:00:00	0:00:00	0:11:33	8:11:31	0:18:49	65:38:13
0:55:37	4:40:32	12:17:48	0:00:00	0:00:00	0:17:16	0:09:57	4:28:08	0:00:00	60:50:34
4:26:52	1:52:07	0:00:00	2:16:41	0:00:00	0:00:00	1:13:01	2:25:47	0:06:30	68:43:35
2:25:35	2:33:44	4:06:50	2:58:50	0:00:00	1:11:37	0:11:13	0:12:03	2:54:01	56:40:16
1:14:00	0:25:52	1:24:59	0:33:00	0:00:00	0:01:20	0:00:00	0:03:47	3:40:55	48:17:43
5:00:21	4:15:02	3:01:06	1:15:47	0:09:47	0:45:13	1:21:17	0:44:36	2:21:48	71:03:19
2:31:42	2:47:25	0:00:00	0:00:00	0:00:00	0:00:00	1:14:35	0:35:08	0:44:57	30:53:58
4:47:28	6:39:48	1:12:55	0:11:37	4:50:41	0:00:00	2:05:30	0:34:00	4:42:02	78:33:33
11:57:53	3:44:52	1:24:24	0:56:23	0:00:00	0:00:00	0:58:31	1:30:45	1:23:55	#######
18:11:47	7:19:24	0:55:23	1:18:44	0:05:52	1:38:12	0:18:58	0:00:00	3:03:44	83:27:06

Fig. 18. *Analysis of machine operation.*

Figure No. 18 shows the working hours of individual machines, in addition to the operation of the PERO AG 2504-019 machine marked in the column as PEE 250. During the operation of the

machine, it is inevitable that there will be a malfunction that will further cause a stoppage in production, and all of this will be reflected on the final product, costs and quality, as shown in Figure No. 19 [1].

	YTD 2020	Januar	Februar	Mart	April	Maj	Juni	Juli	August	Septembar	Oktobar	Novembar	Decembar	
Vrijeme proizvodnje [h]	9588,409	8475	9567,5	9037,5	9630	7447,5	9142,5	10597,5	5812,5	12675	12786	11422,5		
Vrijeme zastoja [h]	87,32909	52,7	65,38	60,83	68,74	56,67	49,18	71,05	30,53	78,55	124,54	83,45		
Broj zastoja	182,9061	178	200	198	217	150	133	184	105	223	239	195		
MTTR 2019	0,378	0,378	0,378	0,378	0,378	0,378	0,378	0,378	0,378	0,378	0,378	0,378	0,378	
MTTR 2020	0,363	0,295	0,327	0,307	0,317	0,378	0,362	0,366	0,291	0,352	0,521	0,451		
MTBF 2019	49,32	49,32	49,32	49,32	49,32	49,32	49,32	49,32	49,32	49,32	49,32	49,32	49,32	
MTBF 2020	52,66	47,32	42,46	45,34	44,96	49,27	58,38	56,72	55,07	56,49	52,89	61,29		

Fig. 19. *Machine downtime analysi.*

Figure No. 19 shows a tabular presentation of the analysis of production time and downtime for the year 2020. (where the month of December is not included). The above table shows a comparison of the dismissals that occurred in 2019, and 2020. for the same monthly periods. Calculations require data recorded in the computerized maintenance management system (CMMS): number of breakdowns, number of working hours of the machine, number of working hours spent on maintenance tasks. It is worth noting what the abbreviations MTTR and MTBF stand for. The abbreviation MTTR stands for "Mean Time To Repair" (eng. Mean Time To Repair), that is the time required to repair a machine or machine system and make it 100% functional again. Time is measured from the time the repair begins until the machine is back up and running at full capacity, and includes repair time, test time, and time to return to normal operating conditions. MTTR time is calculated by dividing the total maintenance time by the total number of repairs during a defined period.

MTTR = total maintenance time / total number of repairs …(1)

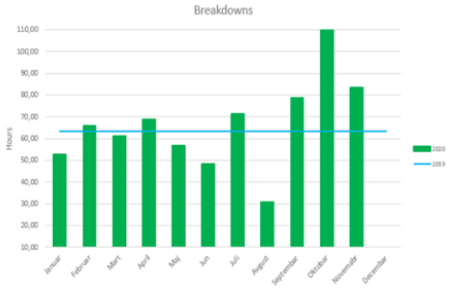


Fig. 20. *The graphical interpretation of the machine failures occurrence.*

The abbreviation MTBF stands for "Mean Time Between Failures". This is the most well-known indicator that measures the time elapsed from one mechanical or electrical failure to the next failure while the machine is in normal operation. The MTBF indicator measures the time predicted for how long a machine will operate before the next unplanned failure occurs. In fact, MTBF is a prediction of when the next failure will occur. MTBF is calculated by dividing the total machine uptime by the total number of failures over time [1].

MTBF = total operating time / number of failures …(2)

MTBF is measured only for technological systems that can be repaired and for failures caused by damage that cause plant shutdown depending on the duration of repairs of the damaged machine. It does not take into account the time the plant spends in suspension for planned maintenance activities. The higher the MTBF, the longer the machine system will operate without failure.

Analyzing the data from Figure No.20, if we look at the MTTR parameter, we come to the conclusion that for one-year better monitored and implemented maintenance, the MTTR was higher in 2019 compared to 2020, which means that the time needed to repair the machine was longer in 2019 compared to 2020, i.e. with better and more efficient maintenance, fewer hours were successfully spent in regulating the failure, i.e. repairing the machine and restoring its functionality in operation. The same thing can be said with observing MTBF. It was previously stated that the higher the MTBF, the longer the mechanical system will be without failure, and we can see this in the table from Figure No. 19, where it was higher in 2020 compared to 2019 for the same observed period. So, in 2020, the machines worked significantly longer until a new failure occurred compared to the year before, where the failure occurred at more frequent time intervals. Figure No. 20 presents a diagram of failures at the annual level. Months for the year 2020 are entered on the abscissa, and hours of machine operation on the ordinate. The comparison and cross section is given for the year 2019 and the same is shown by blue line in the diagram given with figure No. 20 [1].

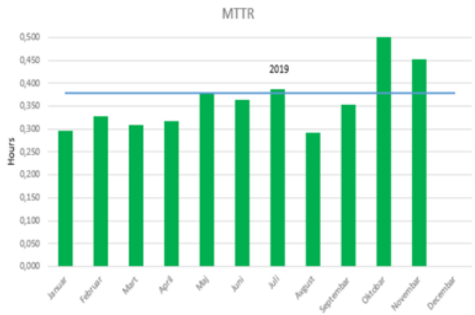


Fig.21*. Value of MTTR 2020 and cross section with MTTR 2019.*

The graphical interpretation of the mean repair time and the mean time between failures for the observed and compared years 2019 and 2020 are presented oh figure 21 and figure No. 22 [1].

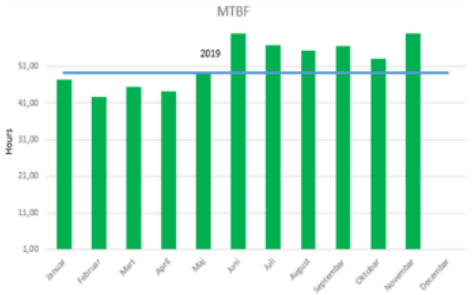


Fig.22*. Value of MTBF 2020 and cross section with MTBF 2019.*

5. Conclusions

The article presents the methods of cleaning, maintenance and inspection of machine PERO (D 2504-019).Practically all stages of maintenance procedure through 13 steps are explained in details. that were previously theoretically explained in this article are presented. Based on examples from practice, this article shows that the entire maintenance process based on TPM principles. All indicators of reliable operation of analyzed machine are presented. In order to improve quality of maintenance, we did compare data from the different periods of machine work on regular basis.

6. References

[1] Alagić Ismar, PROJEKTOVANJE TEHNIČKIH SISTEMA ZA ODRŽAVANJE- sa fokusom na montažu mašinskih konstrukcija i visokoregalnih skladišta, ISBN 978-9958-31-492-6, COBISS.BH-ID 45855494, Off-set, Tuzla, 2021.

[2] Alagić Ismar, MONTAŽA I DEMONTAŽA: Tehnike spajanja i tehnološki sistemi u montaži sa primjenom u industriji, ISBN 978-9958-31-491-9, COBISS.BH-ID 45851142, Off-set, Tuzla, 2021.

[3] Alagić Ismar, Tehnologija montaže i demontaže, ISBN 978-9958-617-53-9, COBISS.BH-ID 41739782, Univerzitet u Zenici, Mašinski fakultet, Zenica, 2020.

[4] Alagić Ismar, ASSEMBLY AND MAINTENANCE OF HIGH BAY WAREHOUSES ON A PRACTICAL EXAMPLE OF A METAL STRUCTURE INSTALLATION PROJECT, ISSN 2367-3370 ISSN 2367-3389 (electronic) Lecture Notes in Networks and Systems, ISBN 978-3-031-31065-2 ISBN 978-3-031-31066-9; Nature Switzerland AG 2023.

Renovation of moulds for high-pressure casting of aluminium by laser cladding

Janette Brezinová, [1,*] Miroslav Džupon[2]
Technical University of Košice, Faculty of Mechanical Engineering, Košice, Slovakia[1]
Slovak Academy of Science, Institute of Materials Research, Košice, Slovakia[2]
janette.brezinova@tuke.sk, mdzupon@saske.sk,

Abstract: *The paper presents the results of an investigation focused on the analysis of the wear of moulds for high-pressure casting with Al alloy. In order to repair and refurbish the mould parts of moulds for high-pressure casting of aluminium alloys, samples of experimental welds were prepared on the base material of grade 1.2343 (Dievar) of dimensions 150x130x30 mm refined to the hardness value of 44-48 HRC. A TruDisk 4002 solid-state disk laser with BEO D70 focusing optics was used for surfacing. Mat.No.1.2343 (Dievar), Mat.No.1.6356 (Dratec) and Mat.No.1.6356 (UTPA 702 and NIFIL NiCu7/Dievar) wires were used as additional material. Light microscopy technique was used to inspect the microstructures on the cross-sections of the welds. Microhardness measurements were performed with a Vickers indenter at a load of 500 g and a mutual indentation distance of 0.4 mm between the indenter impressions..*
Keywords*:* LASER CLADDING, DIE CASTING, CASTING DIES, ALUMINIUM, CONTACT ANGLE

1. Introduction

High-pressure die casting is a process that is used in the manufacture of components used mainly in the automotive industry but also in the aerospace industry. The principle of this technology consists in injecting, at a temperature of 670 - 710 °C, aluminium and its alloys into the mould cavity at high speed (30 - 100 m.s-1) and under high pressure (70 - 120 MPa) through complex injection systems. This process consists of several steps, from spraying the release agent on the mould surface, opening and closing the mould, but also the actual solidification of the casting (crystallisation) is important. Before each casting process, a release agent is sprayed on the mould surface to prevent the liquid metal from sticking to the mould surface and to ensure easier removal of the casting from the mould. The mould and its functional parts are preheated to a temperature of 400 °C prior to casting, where a significant temperature gradient occurs as the aluminium hits the mould surface at temperatures of around 700 °C. The layers on the mould surface tend to increase in size due to the natural thermal expansion from 400 °C to 700 °C. This expansion is limited by the other layers beneath them. The situation is then similar to the application of compressive surface stresses, which force the surface layers to be smaller in dimension than would be expected at these temperatures. However, as a consequence, the areas below the surface will be subjected to tensile stresses. Moulds designed for high pressure aluminium die casting are subject to a number of effects, mainly mechanical stresses, temperatures and liquid metal filling rates. These effects result in degradation mechanisms that act on the moulds and cause them to wear, Fig.1. Worn moulds require refurbishment once the condition is considered. One of the options to increase the life of the moulds is by cladding [1-8].



Fig. 1 *Initiation and propagation of cracks due to thermal gradient of the mould surface*

2. Experimental methodology and material

In order to repair and refurbish mould parts of moulds for high-pressure casting of aluminium alloys, samples of experimental welds were prepared on the base material of grade 1.2343 (Dievar) of dimensions 150x130x30 mm refined to a hardness value of 44-48 HRC. A TruDisk 4002 solid-state disk laser with BEO D70 focusing optics was used for surfacing. As additional material, Mat.No.1.2343 (Dievar), Mat.No.1.6356 (Dratec) and Mat.No.1.6356 (UTPA 702 and NIFIL NiCu7/dievar) wires were used.

The winding parameters were:
(a) Dievar additive material, laser power 1500W, crimping speed 6 mm/s, feeding speed feed rate 10 mm/s, focus 20 mm, protective atmosphere Ar (4.6) 7 l/min.

b) Dratec additive, laser power 1600W, winding speed 6 mm/s, feeding speed feed rate 10 mm/s focus 20 mm, protective atmosphere Ar (4.6) 10 l/min/min

c) UTPA702 additive material, laser power 1500W, winding speed 6 mm/s, feeding speed feed rate 5 mm/s, focus 0 mm, protective atmosphere Ar (4.6) 12 l/min.

Table 1: *Chemical composition of the additive materials used [wt.%]*

	Element										
	C	Si	Mn	Cr	Mo	Ni	Co	Ti	Al	Cu	Fe
1.2343 (Dievar)	0,463	0,147	0,423	5,13	2,27	0,067	<0,01	<0,002	0,008	-	Rest.
1.6356 (UTPA 702)	0,020	-	-	-	4,0	18,0	12,0	1,60	0,10	-	Rest.
1.6356 (Dratec)	0,0005	0,20	0,50	0,15	4,0	18,0	12,0	1,60	-	-	Rest.

Light and electron microscopy, EDX microanalysis

Light microscopy technique was used to examine the microstructures on cross-sectional sections of the striae in the magnification range of 25x to 1000x. The inspection of the welds was focused on the identification of defects and non-integrity of the welds. Scanning electron microscopy technique and semi-quantitative EDX microanalyses were used to analyse the distribution of alloys in the 1.2343 Dievar, 1.6356-UTPA 702 and 1.6356-Dratec alloys.

Hardness of cladds

Microhardness measurements were performed with a Vickers indenter at a load of 500 g and a mutual indentation distance of 0.4 mm.

Verification of surface wettability of samples with modified topography by contact angle measurement techniques

Only stochastic texture can realistically be applied to the mould parts of moulds for high-pressure casting of aluminium alloys on cold chamber machines. After each casting cycle, a separating agent - lubricant - is applied to the mould parts in order to form a thin layer on the surface preventing direct contact of the melt with the metal surface of the mould part. At the same time, this layer is also a thermal barrier. When filling the mould cavity with the aluminium alloy melt, this separation layer lubricant may be removed locally and the aluminium alloy melt is in direct contact with the metal surface of the mould. Research in the field of modification of the surface topography of mould parts was aimed at obtaining information on the interaction of separating agents (lubricants) used for the treatment of mould parts with modified surface topography - texturing by low-energy laser radiation. Tests of the interaction of the separating agent SafetyLube 7815 with the laser-textured surface by the "random" mode were carried out. The run-in phase conditions of the new or refurbished mould part were approximately obtained by repeated heating to 250°C (mould part temperature in high pressure die casting of aluminium alloys) and repeated splashing with SafetyLube 7815 release agent.

3. Results and discussion

Material 1.2343-Dievar. HAZ /heat affected zone/ thickness was max.0,5 mm. Microstructure in the coating - sorbitic with directed crystallization, without integrity defects, zone of building - without integrity defects and anomalies in microstructure, in HAZ gradual transition from ferritic-carbide mixture to sorbitic microstructure of the base material, Fig.2.



Fig.2 *Material 1.2343-Dievar, a) disposition; b) detail of the outline; c) background material*

Material 1.6356 - UTPA 702. HAZ thickness was max. 1.0 mm. Microstructure in the coating - casting with directed crystallization (visible in scanning electron microscope in BSE mode), without integrity defects, HAZ - without integrity defects, build zone without integrity defects, base material - sorbitic microstructure without integrity defects, Fig.3.

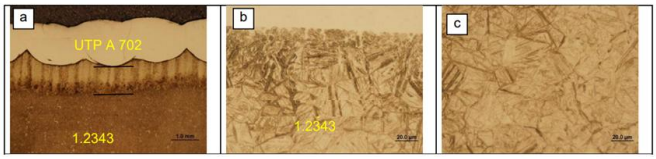


Fig.3 *Material 1.6356 - UTPA 702, a) disposition; b) detail of HAZ and construction material; c) detail of HAZ*

Material 1.6356 - Dratec. The thickness of HAZ was max. 1.0 mm. Microstructure in the coating - casting with directed crystallization (visible in scanning electron microscope in BSE mode), without integrity defects, HAZ - without integrity defects, build zone without integrity defects, base material - sorbitic microstructure without integrity defects, Fig.4.

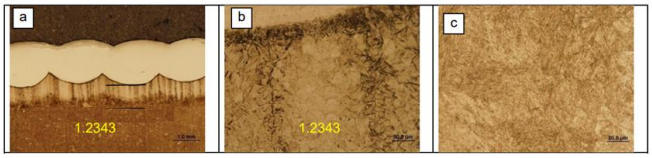


Fig.4 *Material 1.6356 - Dratec, a) disposition; b) TOZ detail and melting zone; c) detail of HAZ*

In both layers of the 1.2343-Dievar deposit, the distribution of alloys was uniform, Fig.5. In the 1.6356-UTPA 702 deposit, no cobalt was detected in the second layer, Fig.6. In the second layer of the 1.6356-Dratec deposit, the concentration of cobalt and nickel was reduced with respect to the first deposit, Fig.7.

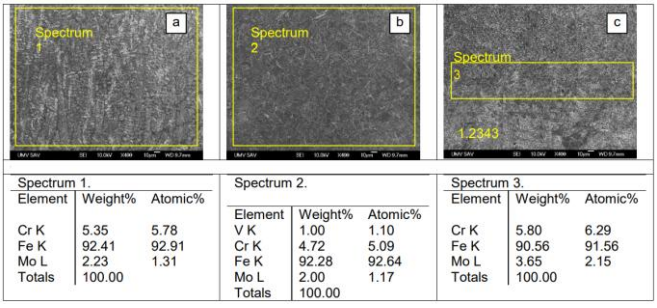


Fig.5 *Microstructure of material 1.2343; a) 2nd layer of clad; b) 1st layer of clad; c) HAZ*

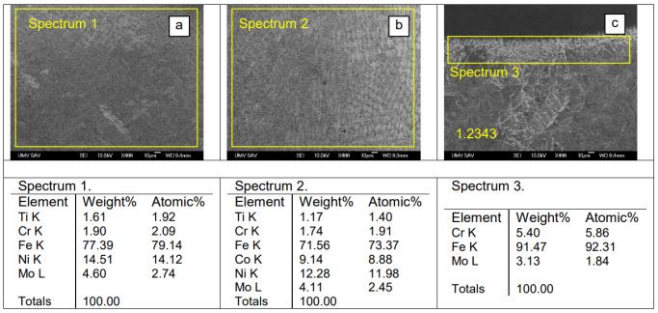


Fig.6 *Microstructure of material 1.6356-UTPA 702; a) 2nd layer of clad; b) 1st layer of clad; c) HAZ*

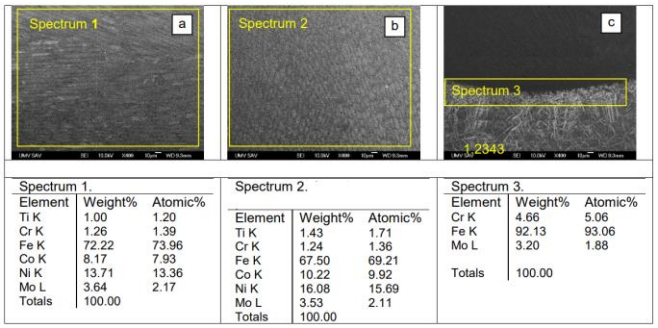


Fig.7 *Microstructure of material 1.6356-Dratec; a) 2nd layer of clad; b) 1st layer of clad; c) HAZ*

Material 1.2343-Dievar - At the surface the microhardness value was 600 HV0.5, at a depth of 0.8 mm the microhardness was ~ 700 HV0.5, Fig. 8a. Die 1.6356-Drill and Die 1.6356-UTP702 A - From the surface to a depth of 1.2 mm, the microhardness value was 400HV0.5. At a depth of 1.6-2.0 mm, the microhardness value was locally increased to 600-700 HV0.5 Fig.8 b,c.

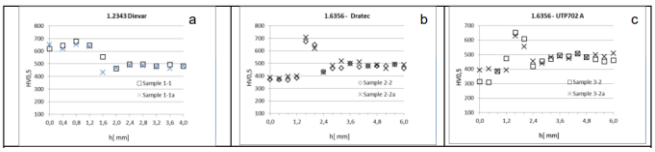
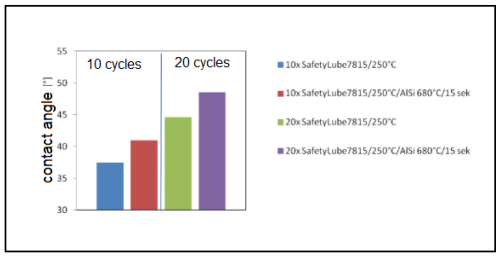


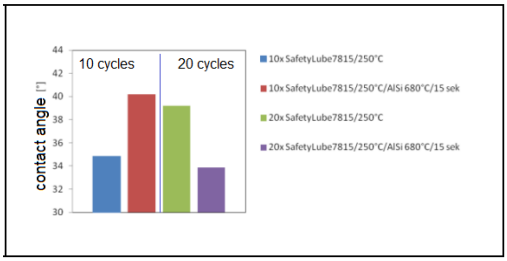
Fig.8 *Microhardness from surface, indentation distance 0,4 mm; a) material 1.2343 - Dievar ; b) material 1.6356 - Dratec; c) material 1.6356 - UTP 702 A*

After ten and twenty cycles of abrasion with the separating agent, the 250°C samples were immersed in an aluminum alloy melt maintained at 680°C. The immersion time was 10 seconds. The ablation craters were coated with a thin layer of Safety Lube 7815 lubricant after ten cycles. After twenty cycles, there was a 2 and 3 times thicker layer of Safety Lube 7815 lubricant in the ablation craters.

The contact angle measurement was targeted to test the methodology designed to determine the number of splashes of the separating agent - lubricant Safety Lube 7815 on the surface of the new or renovated mould part for the first casting cycle. On the textured surface of the Dievar grade material, the increase in the contact angle value with the number of Safety Lube 7815 splash cycles was measured, Fig.9. The contact angle values of Safety Lube 7815 were measured on the PVD coating $NaCRo_4$ deposited on the textured surface (texture random). The contact angle values as a function of the number of spray cycles with Safety Lube 7815 separator were smaller after 20 spray cycles and a 15 second immersion in the aluminium alloy melt than after 10 spray cycles and a 15 second immersion in the aluminium alloy melt.



a)



b)

Fig.9 *Contact angle vs. number of spray cycles lubricant Safety Lube 7815. a) Surface Punch + texture random, b) Surface Dievar + laser random + duplex $NaCRo_4$ coat*

4. Conclusions

The paper presents the results of research aimed at determining the quality of three types of brews. Three types of strands were produced by lasso technology. A TruDisk 4002 solid-state disk laser was used for the surfacing. DIEVAR, DRATEC AND UTPA702. The quality of the overlays was evaluated by light and electron microscopy and the chemical composition of the different regions was evaluated by EDX microanalyses. The distribution of alloys was uniform in the coatings. The blooms showed high structural quality. The use of surface texturing provides the possibility to ensure smooth lubrication of the moulds, especially in the mould run-out. Further research will be focused on the determination of the quality of the welds under the conditions of high temperature corrosion in molten aluminium.

Acknowledgments: This contribution is the result of the project implementation: "Innovative approaches to the restoration of functional surfaces by laser weld overlaying" (APVV-20-0303), supported by the Slovak Research and Development Agency and supported by the Ministry of Education of Slovakia Foundation under grant projects VEGA No. 1/0497/20 "Application of progressive technologies in restoration of functional surfaces of products" and KEGA 036TUKE-4/2021 "Distance form of education in the field of engineering technologies using modern IT tools for foreign students". This support is highly appreciated by the authors. Conflicts of Interest: The authors declare no conflict of interest.

5. References

1. M. Sadeghian, M. Shamanian, A. Shafyei:. Materials & Design 60 (2014), pp. 678-684.
2. L. Binglin, J. Y. Richard Liew, A. L. Hoang: Engineering Structures 200 (2019), pp. 256-263.
3. A. Behera: Materials Today: Proceedings (2020), pp. 1-5.
4. C. Zhu, J. Cheon, X. Tang, S. Na, F. Lu, H. Cui Effect of swing arc on molten pool behaviors in narrow-gap GMAW of 5083 Al-alloy J. Mater. Process. Technol., 259 (2018), pp. 243-258
5. D. Chen, M. Chen, C. Wu Effects of phase difference on the behavior of arc and weld pool in tandem P-GMAW J. Mater. Process. Technol., 225 (2015), pp. 45-55
6. K. Wu, T. Yin, N. Ding, M. Zeng, Z. Liang Effect of phase on the behavior of metal transfer in double-wire pulsed GMAW Int. J. Adv. Manuf. Technol., 97 (2018), pp. 3777-3789
7. K. Wu, N. Ding, T. Yin, M. Zeng, Z. Liang Effects of single and double pulses on microstructure and mechanical properties of weld joints during high-power double-wire GMAW J. Manuf. Process., 35 (2018), pp. 728-734
8. J. Chen, Y. Zhang, C. Wu, G. Padhy Suppression of undercut defects in high-speed GMAW through a compound magnetic field J. Mater. Process. Technol., 274 (2019), p. 116288

AFM morphology of sol gel coatings on glass for photovoltaics

Stancho Yordanov[1], Silviya Simeonova[2], Mihaela Aleksandrova[1], Vladimir Petkov[1], Bojidar Jivov[1]
[1] Institute of Metal Science, Equipment and Technologies with Hydro- and Aerodynamics Centre "Acad. A. Balevski", Bulgarian Academy of Sciences
[2]Sofia University "St. Kliment Ohridski" Faculty of Chemistry and Pharmacy, Department Physical Chemistry, 1164 Sofia, 1 James Bourchier Blvd.
e-mail: stancho14@abv.bg

Abstract: *In this paper, we present the results of atomic force microscopy (AFM) characterizing the surface morphology of nanostructured coatings on photovoltaic glass obtained by the sol-gel method. Two organic titanium precursors were used to prepare the TiO_2 deposition solution: Titanium isopropoxide (TTIP) and titanium tetrabutoxide - $Ti(OC_4H_9)$. The hydrolyzing agent is distilled water and the stabilizer is nitric acid /HNO3/and acetylacetone (AcAc). Many samples were obtained at different ratios of the components involved, rate of application of the solution on the glass substrate, and different curing and holding temperatures. The samples were characterized by AFM analysis.*

Keywords*: AFM, TIO_2 fiLMS, SOL-GEL METHOD, $TI(OBU)_4$, TTIP*

1. Introduction

The intensive construction of photovoltaic systems represents an adequate energy alternative [1-7] in line with modern trends towards high energy efficiency, use of ecological renewable energy sources and increasing the energy independence of individual consumers. Regarding the final consumers of the generated electricity, photovoltaic plants are classified into three main categories [1,2,4]: stand-alone installations (providing power only to remote sites) mainly equipped with electricity storage systems, installations connected to the National Electricity Distribution Network and combined (hybrid) systems combining the characteristics of the previous two. A variety of photovoltaic installations [2,4] have been developed for business, manufacturing or industrial sites with a power of 10 kWp, 30 kWp, over 200 kWp and up to 500kWp or applicable to multi-family or single-family residential buildings with a power of mostly 10 kWp.

The full functioning of photovoltaic installations is determined by a number of factors [1,2,4]: positioning and orientation of solar modules, impact of cyclic day and season weather changes, climatic specifics of the region, pollution [8,9] of the working surface of photovoltaic panels etc. Predominant pollutants are diverse fractions of dust particles [8,9] of natural or industrial origin, heterogeneous local surface deposits, products of the life cycle of various populations of biological organisms, and others. A variety of cleaning systems [8,9] are applicable to different types of photovoltaic installations: manual, automated, robotic, and others. At the same time, the development of innovative nano-sized, self-cleaning coatings [10,11] obtained by technological methods providing a long-lasting effect, high atmospheric resistance and the presence of other performance indicators [10-40] is of significant interest: anti-reflective, hydrophobic, fire-resistant, anti-dust, anti-icing, anti-fog and others.

The technological possibilities for the deposition of two-layer self-cleaning [12,13] TiO_2/SiO_2 and ZrO_2/SiO_2 antireflective [14] thin films applicable to the preparation of surface coatings and their influence on the efficiency of photovoltaic modules have been investigated.

In the present study, self-cleaning protective coatings potentially applicable in the production of various photovoltaic modules with increased efficiency were prepared by the sol-gel method.

2. *Experimental*

2.1. Materials

All compounds were supplied as analytical grades and were used without further modification. Thin film coatings are performed on glass slides from AGC Glass Europe. TiO_2 precursors and solvents were 99% titanium butoxide - $Ti(OBu)_4$ and 99.9% ethanol (C_2H_5OH), all purchased from Alfa Aesar Germany. The hydrolyzing agent is distilled water, and the stabilizer is nitric acid /HNO_3/.

2.2. Preparation of the glass substrate.

Before being cleaned, the slides were cut to size (20 mm x 70 mm x 2 mm). Substrate cleaning is important prior to the deposition process, as this allows the cleaning and removal of submicron particles from the substrate surface. After cleaning the substrate is coated with the resulting sol. This is decisive for the quality of the bonding film on the substrate. The glass substrates were cleaned/washed/ in 99.9% ethyl alcohol for 15 minutes and acetone for 15 minutes and then dried for 30 minutes at 100^0C. Cleaning the glass substrates improves the adhesion of the coating material to the substrate and prevents contamination on the formed coating.

2.3. Preparation of TiO_2 sol.

The aim of the synthesis is to obtain coatings of TiO_2 on glass substrates applying sol-gel method. Mixture of precursor – 5 ml of 99 % $Ti(OBu)_4$ and 5 ml of DEA /$C_4H_{11}NO_2$/– was added dropwise to the acid solution, made of ethanol, water and nitric acid in a ratio of 1:1:0.5 for prevent gel formation. To ensure adequate hydrolysis, the mixture was continuously stirred at 500 rpm with a magnetic stirrer for 2 hours under air pressure to produce a pink translucent solution /fig.1/.

Schematics of the process of obtaining a thin film of sol gel with TiO_2

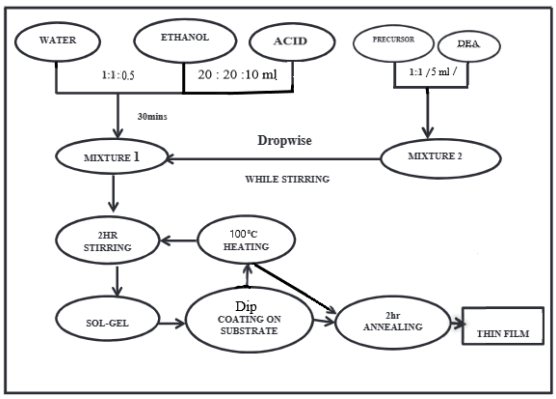


Figure 1. Depiction of the chemical synthesis of TiO_2-based sol

A dip coating machine (Dip Coating technology) at a speed of 42.8 mm/min was used to deposit thin layers of TiO_2 on the substrates. A lower speed of the applied solution on the glass substrate helps the coating to be uniform, while a higher rate helps the solution to become thinner. The deposited films were then heated at a temperature of 400^0C for 2 hours.

Table for samples:

samples:	Main composition:	Drying time	T°C-treatment	Number of layers
GlS-2	$Ti(OBu)_4$	30 min.	400°C- 2 h.	2
GlS-3	$Ti(OBu)_4$	30 min.	400°C- 2 h.	3
GlS-4	TTIP	30 min.	500°C- 2 h.	1

$Ti(OBu)_4$ – Titanium butoxide, $Ti(OBu)_4$ (Bu = $CH_2CH_2CH_2CH_3$)

TTIP - Titanium tetraisopropoxide, $Ti[OCH(CH_3)_2]_4$

Atomic force microscopy (AFM)

Atomic force microscopy (AFM) is a modern method that is widely used in the field of nanotechnology for the study of surface structure and topography of various samples. In the study with an atomic force microscope, high precision and resolution in the nanometric scale is achieved.

AFM imaging was performed on the NanoScope V system (Bruker Ltd, Germany) operating in tapping mode in air at a room temperature. We used silicon cantilevers (Tap 300Al-G, Budget Sensors, Innovative solutions Ltd. Bulgaria) with 30 nm thick aluminum reflex coatings. According to the producer's specifications the cantilever spring constant and the resonance frequency are in the range of 1.5 to 15 N/m and 150 ± 75 kHz, respectively. The radius of tip curvature was less than 10 nm. The scanning rate was set at 1 Hz and the images were taken in highest possible resolution mode of the AFM, 512 × 512 pixels in JPEG format. The NanoScope software was used for the section analysis and roughness of the all images.

3. Results and Discussion

The obtained results for the samples from the GLS series show very good protective properties of the applied sol-gel coatings**.**

3.1. Characterization of the measured surface of the samples GLS 2, GLS 3 and GLS 4 by Atomic force microscope

The topography of the samples GLS 2, GLS 3 and GLS 4 was measured using an atomic force microscope with a surface scan area - 5 μm, is presented in Fig.2. An analysis of the surface was made as well as an assessment of the roughness of the different coatings: - TiO_2-deposited coatings with different percentages in titanium tetrabutoxide solution (GLS 2 and GLS 3), as well as TiO_2-deposited coatings with different percentages of solution in titanium isopropoxide solution (GLS 4). The morphology and roughness of the coatings were compared.

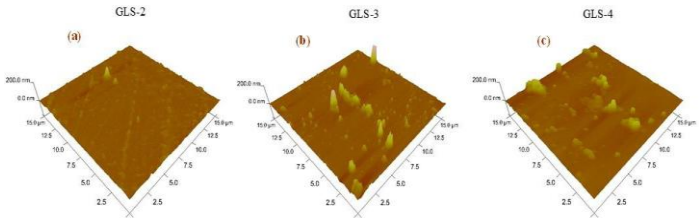


Figure 2. *3D AFM images of the surface of the samples GLS 2, GLS 3, GLS 4 with scan area 5 × 5 μm² and z-range, z = 100 nm and z = 200 nm*

From the AFM images and the analysis of the roughness of the different samples it was found:

1. In the topography of the samples GLS 2 and GLS 3 with applied organic precursor of titanium tetrabutoxide, areas with a smooth surface as well as areas with a rougher surface are observed. The roughness value Rq for the scan surface at 5 μm for the coating GLS2 and GLS 3 is in the range between 5.51 nm and 14nm.

2. In the topography of the sample GLS 4 with applied organic precursor of titanium tetraisopropoxide, again areas with a smooth surface as well as areas with a rougher surface are observed. The roughness value Rq for the scan surface at 5 μm for the coating GLS 4 is in the range 11.7 nm.

4. *Conclusions*

3D AFM images of the samples: GLS-2, GLS-3, GLS-4 were obtained.

The AFM images of the three coating types were compared from the AFM measurements and it was found that, the topography of the surface of the three samples is different, which is due to the different coatings in the system. Difference in the structures is in the range at about 10 nm.

It is observed that the coating GLS 2 with $Ti(OBu)_4$ has low value - 5.51 nm of the roughness Rq at a scanned area of 5 μm. While for the GLS 4-/coating with TTIP/, the roughness values Rq at a scanned area of 5 μm are higher to those of the GLS 2.

The preparation of self-cleaning protective coatings by the sol-gel method are potentially applicable in the production of various photovoltaic modules with increased efficiency.

5. References

1. S. A. Kalogirou, The potential of solar industrial process heat applications. Applied Energy, , 76: 337-61 (2003).
2. G. K. Singh, Solar power generation by PV (photovoltaic) technology: A review, Energy, Vol. 53), pp. 1-13 (2013)
3. J. Barwicki, M. Kubon, A. Marczuk, "New Developments of Solar Energy Utilization in the Aspect of EU Directives", Agric. Eng. 21, pp 15–24, (2017).
4. L. Hernández-Callejoa, S. Gallardo-Saavedraa, V. Alonso-Gómez, "A review of photovoltaic systems: Design, operation and maintenance", Solar Energy, Vol. 188, pp. 426-440. (2019).
5. Kougias, I.; Taylor, N.; Kakoulaki, G.; Jäger-Waldau, A. The role of photovoltaics for the European Green Deal and the recovery plan. Renew. Sustain. Energy Rev. 144, 111017, (2021).
6. Elzbieta Rynska, Review of PV Solar Energy Development 2011–2021 in Central European Countries, Review, Energies, 15, 8307. (2022).
7. E. Kulińska, M. Dendera-Gruszka, „New Perspectives for Logistics Processes in the Energy Sector", *Energies,15* (15), 5708, (2022).
8. M. Mani, R. Pillai, Impact of dust on solar photovoltaic (PV) performance: research status, challenges and recommendations. Renew. Sustain. Energy Rev. 14, pp. 3124–3131, 2010.
9. B. S. Yilbas, H. Ali, M. M. Khaled, N. Al-Aqeeli, N. Abu-Dheir, K. K. Varanasi, Influence of dust and mud on the optical, chemical, and mechanical properties of a PV protective glass. Sci. Rep. 5, 15833, (2015).
10 10J. Son, S. Kundu, L.K. Verma, M. Sakhuja, A.J. Danner, C.S. Bhatia, H. Yang, A practical superhydrophilic self cleaning and antireflective surface for outdoor photovoltaic applications. Sol. Energy Mater. Sol. Cells98, pp. 46–51, (2012).
11 Zhi, J., and Zhang, L.-Z., Durable Superhydrophobic Surface with Highly Antireflective and Self-Cleaning Properties for the Glass Covers of Solar Cells, (2018)
12 A. Soklic, M. Tasbihi, M. Kete, U. L. Stangar, Deposition and Possible Influence of a Self-Cleaning Thin TiO_2/SiO_2 Film on a Photovoltaic Module Efficiency. Catal. Today 252pp. 54–60, (2015)
13 Adak, D., Ghosh, S., Chakrabarty, P., Mondal, A., Saha, H., Mukherjee, R., et al., Self-cleaning V-TiO_2:SiO_2 Thin-Film Coatings with Enhanced Transmission for Solar Glass Cover and Related Applications. Solar Energy 155, pp. 410–418, (2017).
14 Li, J., Lu, Y., Lan, P., Zhang, X., Xu, W., Tan, R., et al., Design, Preparation, and Durability of TiO_2/SiO_2 and ZrO_2/SiO_2 Double-Layer Antireflective Coatings in Crystalline Silicon Solar Modules. Solar Energy 89, pp. 134–142, (2013).

Application of reverse engineering techniques in automotive component design

Kender Štefan[1], Brezinová Janette[1]
Technical University of Kosice, Slovakia[1]
stefan.kender@tuke.sk
janette.brezinova@tuke.sk

Abstract: *The aim of the work was to digitize an automotive component using reverse engineering. To apply the procedures by which an automotive component can be designed. Reverse engineering belongs in the field of innovation among the first established knowledge-intensive services. Together with the advancing development of technology and utilizing of 3D scanning, the reverse engineering is becoming an important tool for accelerating the product innovation cycles and increasing the potential of lean approach and agility of development processes in Product Design. The paper illustrates the possibilities of using and experience with these tools on examples of the scanning of the geometry of the selected automotive components.*
Keywords*: REVERSE ENGINEERING, 3D SCANNMG, AUTOMOTIVE DESIGN, RAPID PROTOTYPING*

1. Introduction

At the Technical University of Kosice, there was established the Product Design laboratory, where are used 3D scanners MicroScribe G2 and FARO Laser Scanner PlatinumArm in combination with software Rhinoceros, PolyWorks and Autodesk Maya 2012. The possibilities of using and experience with these tools on examples of the scanning of the geometry of the selected automotive components are the main works in this lab.

Digitizing of automotive components is a part of reverse engineering. This process includes transformation of real component shapes to digital form. Result of those actions is mostly a cloud of points, which can be in the future used for e.g. rapid prototyping or product design etc. [1, 2, 3]

Digitizing includes some problematic actions. One of the most problematic are:

- 3D scanning of large-size components and connected operations
- 3D scanning of components with improper surface colour

2. 3d Scanning of large-size components

One of the problematic operations by 3D scanning is large-size components scanning. Large- size components need to be scanned in more steps. Through this kind of scanning partial scans are made. Final points cloud is made by connecting of these partial scans. These operations are demanding for hardware equipment.

Example of this kind of 3D scanning can be e.g. 3D scanning of car petrol tank (Fig.1).



Fig. 1 *Petrol tank prepared for 3D scanning.*

Dimensions of such a petrol tank are bigger than 3D scanner arm possibilities used in our lab (1,8m). This kind of scanning arm allows us to scan component only through partial scans, which are to be connected.

Before 3D scanning process it's necessary to choose a group of planes, which will be scanned in all partial scans. With the help of these planes, the partial scans will be connected. In submitted example of 3D scanning were as an initial group of planes a clip surfaces chosen (Fig.2).



Fig. 2 *Petrol tank prepared for 3D scanning.*

During the scanning process is though choosing an initial group of planes further necessary to made some help planes, which will be useful for better best-fit operations. These planes are chosen by consider (Fig.3).

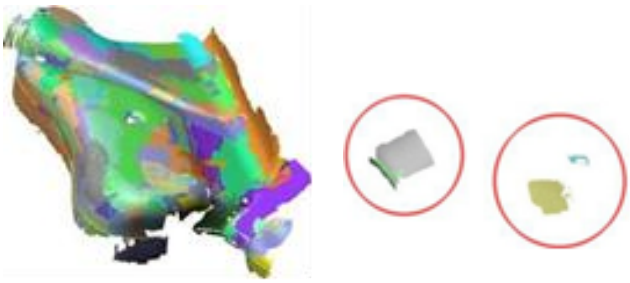


Fig. 3 *Sample of help planes scanned for best-fit operations.*

Another step before 3D scanning is to divide component to several parts which overlay each other. For demonstrative example we 'll show you best-fit of first two partial scans. The I st scan is bigger and creates the base for entire 3D scan (Fig.4).

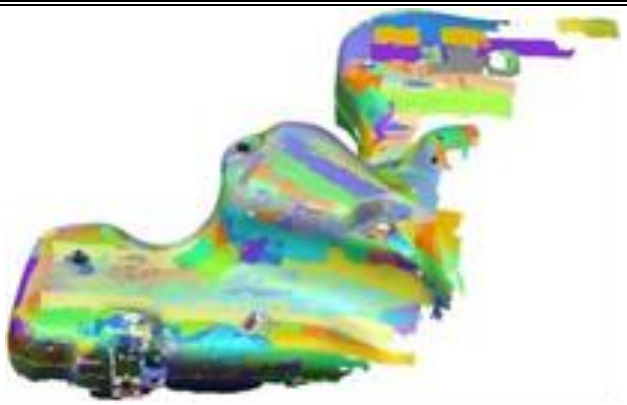


Fig. 4 *I st partial scan of petrol tank.*

The 2nd scan is an opposite side of I st scanned part of component (Fig.5).

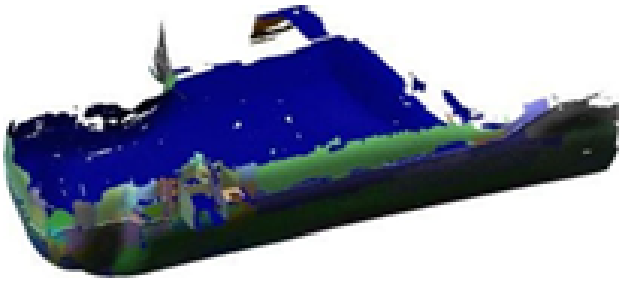


Fig. 5 *2nd partial scan of petrol tank.*

Using predetermined best-fit surfaces, we align these two scans through n-pairs of points (Fig.6). Through the use of this method we we'll obtain a larger unit (Fig.7).

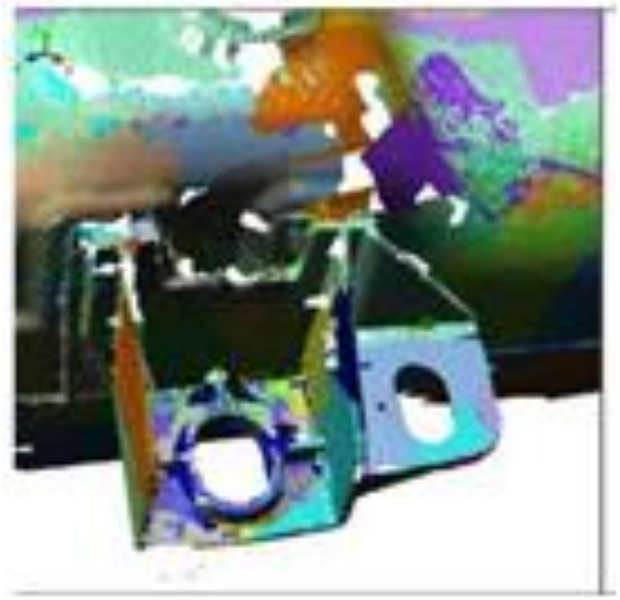


Fig. 6 *Best-fit with n-pair of point.*



Fig. 7 *Unit made by best-fit operations (after points reduction).*

Using these methods we were able to made all another parts of fmal scan. Total number of partial scans was 10 (Fig.8).

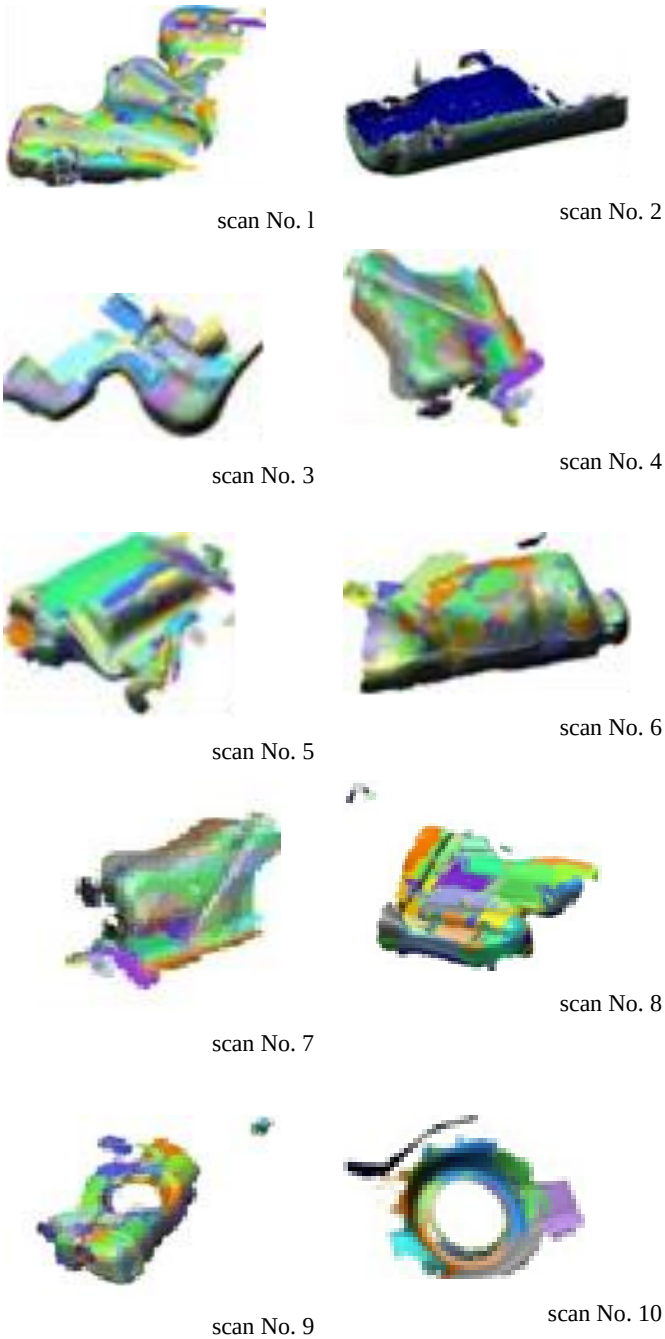


Fig. 8 *Partial scans of petrol tank prepared for best-fit.*

By using the best-fit operations we obtain step by step complete 3D scan of petrol tank. One of the last operations is points overlay reduction (Fig.9).

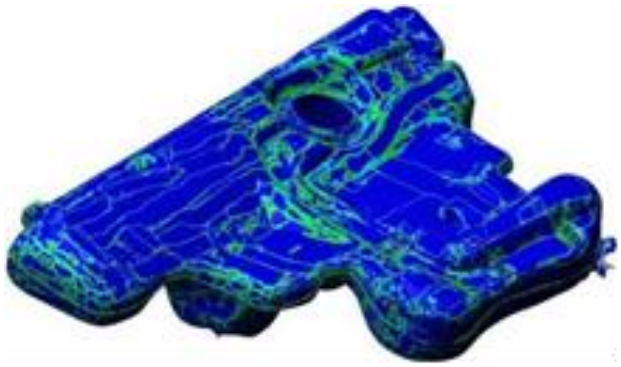


Fig. 9 Points overlay reduction.

Table 1: *Properties of 3D scan of petrol tank.*

Number of partial scans	**10**
Number of scanned parts	**1468**
Total number of scanned points	**14 146 823**
Number of points after points overlay reduction	**22041176**

Points cloud prepared like that is ready to use or export to some CAD software like for example CATIA ant for further modifications.



Fig. 10 Final points cloud (3D scan of petrol tank).

With use of partial scans connecting methods it 's possible to scan also objects or components which are larger than possibilities of scanning equipment. However, this method of producing 3D scans is also available for scanning of smaller components. It can be used for example for

3D scanning of surface parts, which can 't be scanned per one operation and so the component must be moved before scanning another part of surface.

It 's possible to fill up missing parts of surface of scanned component or to make some simple repairs of points cloud. [4]

3. Conclusion

The possibilities of using 3D scanning equipment and experiences with these tools are proving that digitizing is a tight part of product design processes and production. Experiences with 3D scanning equipment show us their high potential in mechanical industry but also in other branch of science. Problems that were introduced in this paper are solvable and results after solving are capable for mechanical industry demands.

Even large components and complex shapes can be digitized in parts. It is important to assemble the individual scans correctly so that they geometrically connect to each other. The joining of adjacent surfaces of the point cloud is based on interpolating the same geometry on two adjacent scans and recalculating its new position through the Best-fit operation.

Acknowledgement:

This contribution is the result of the project implementation:

APVV-20-0303, VEGA No. 1/0497/20and KEGA 046TUKE-4/2022. This support is highly appreciated by the authors. Conflicts of Interest: The authors declare no conflict of interest.

References

1. M. Dúbravčík, Š. Kender. Application of reverse engineering techniques in mechanics system services In: Procedia Engineering: Modelling of Mechanical and Mechatronics Systems. Zemplínska Šírava, Slovakia. - Košice : TU, (2012) Vol. 48 , p. 96-104. - ISSN
2. M. Dúbravčík, Š. Kender, Š. Babjak. Using of 3D scanner in the automotive design. In: Transfer inovácií. (2012), Vol. 22, p. 121-124. - ISSN 1337-7094.
3. M. Dúbravčík, Š. Kender. 3D scanning and measurement with 3D measuring devices. In: It-stro jár. (2011), p. 1-4. – ISSN 1338-0761.
4. B. Shabani, Z. Pandilov. Analyzing and application of reverse engineering for desingn and development of mechanical parts. In: Mechanical Engineering – Scientific Journal, (2017) Vo l. 35, No. 2, p. 89–96. - ISSN 1857–5293.

Thermal decomposition of biomass, significance of biochar

Viktor Madár[1], András Betovics[2*], Norbert Schrempf[2], László Tóth[2]
[1] Pyrowatt Kft., Kiskunmajsa, Hungary
[2] Institute of Technology - Hungarian University of Agriculture and Life Sciences, Gödöllő, Hungary
* E-mail: betovics.andras.mate@phd.uni-mate.hu

Abstract: *Biochar is an uniquely useful renewable resource that has significant advantages in solving many environmental problems. It helps to mitigate the harmful soil degradation experienced in recent years (decades), including the restoration of the balance of pollutants in the soil, water and gaseous medium. After all, synergistically, with proper use, it can improve soil, water and air quality, carbon dioxide sequestration and moderate greenhouse gas emissions. We designed and implemented laboratory equipment (with a total weight of 0.5 kg) and industrial equipment (50 - 100 kg of coal/hour) and validated the laboratory results with this industrial equipment.*
Our equipment is a so-called resting-bed design. Drying and carbonization are also carried out by direct heat transfer. The carbonizing material is continuously rotated in the interior due to the material movement with the stirrer lever. As a result, the quality of the material leaving and entering the reactor is balanced. Better heat transfer and uniform distribution of thermal energy is facilitated by the circulation of the hot gas that fills the space. The high-temperature gas is supplied with a gas jet pump. The energy obtained by burning the pyrolysis gases produced during carbonization ensures the heating of the system, so there is no need for significant external energy input.
According to our results, the quality and other characteristics of biochar vary significantly depending on the type of raw material and pyrolysis conditions. In order to ensure the quality of the created material, the production process must be closely monitored in every detail of the equipment. The continuous quality control of the products cannot be neglected either. According to the opinion of international associations and research groups, significant development of the use of biochar is expected in the future. There is growing interest in the use of biochar to remove pollutants from soil, water and gas, and its potential to replace expensive commercial activated carbon.
KEYWORDS: *BIOMASS; BIOCHAR; PYROLYSIS; QUALITY OF BIOCHAR*

1. Introduction - The significance of biochar for soil and production

Many researchers have been dealing with the return of biochar to the soil for a long time, most of them have registered positive characteristics, according to which it increases the soil's productivity and water retention capacity and thus promotes richer soil life.[1,2,] There are also known publications that talk about negative effects, but they usually draw attention to the characteristics of the soil and describe the quantities that can be applied to a given soil unit and the structure of the biochar. Coals that contain Polycyclic Aromatic Hydrocarbons (PAH group) in excess of what is allowed by law are not recommended. This group of compounds can cause varying degrees of damage to the ecosystems living in the soil through the soil and groundwater.
The IBI (International Biochar Initiative) summarized the researches being carried out at the international level and defined the basic principles that should be supported so that they are as beneficial as possible for the environment and its sustainability. Some of these are:
In order to maintain the quality of the soil, it is advisable to use biochar, which can increase the productivity of the soil and reduce the degradation of the soil, if the soil is overused and eventually rendered unsuitable for agricultural production. [3,4]
Its application improves climate stability, as it is neutral from the GHG point of view. It does not increase atmospheric carbon dioxide, as it enters the soil. Traditional biomass residues decompose quickly in the soil, but the atmospheric gases produced by burning biomass are also immediate pollutants.
It also has a positive effect in terms of energy production, since in the closed system of its production, the energy efficiency is better compared to the traditional one, and the net energy is higher than what is available with traditional combustion processes. [5,6]
The production technology ensures that various residues can also be used. [7]
The technology is such that it does not pollute the immediate environment.

2. Developed biochar producing unit and measurement results

(Type.: PYROCHAR, Manufacturer: PYROWATT KFT.)
Based on literary sources and our own analytical measurements, we prepared the main designs of the carbonization equipment. The detailed plans and construction of the manufactured equipment were carried out by Pyrowatt Kft.
The main features of the equipment are presented in the next section.
In the upper part of the open fuel tank (Figures 1 and 2) there is a screen to separate coarsely large particles (pieces of material). The fuel is carried out by an electrically driven (0.75 kW) scraper on the lower side of the storage tank. The size class of the required fuel is G30 - G50, according to the Önorm M7133 classification.

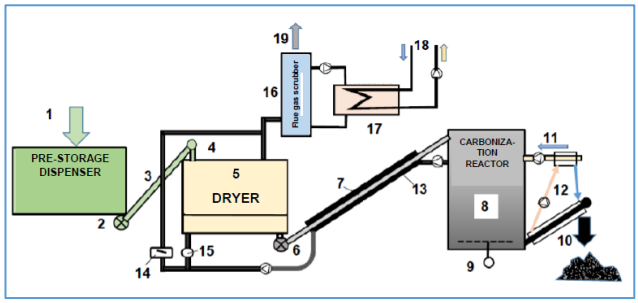
Width of container: 1.5m
- The length of the container: 1.0 m
- The maximum height of the fuel: 1.0 m
- Nominal volume: 1.5 m^3
- The maximum mass flow of the conveyor: 400 kg/h

Fuel with a maximum moisture content of 18% must be provided for the operation of the carbonizer, if it is higher, the fuel must be dried. The fuel is dried using rotary drum technology. The fuel goes from the pre-storage through a feeder into the rotary drum dryer. The energy required for drying is provided by the hot 300-400 °C flue gas coming out of the carbonizer. The flue gas is transported by a radial fan. The dryer is a steel structure that is completely enclosed. Its surface is insulated. Its maximum surface temperature is 65°C. The drying performance can be regulated by the temperature and volume flow of the drying flue gas and steam. At the end of the drying channel, there is a conveyor auger that transports the dry fuel to a coaler.

Heat output requirement of the dryer:
- 200 kW (in the case of the highest mass flow, projected on dry material)
- Material mass flow 240.0 kg/h (from 40% moisture content to 15%)
- Drying temperature: 180-230 °C
- Electrical power requirement: 3.0 kW
- Drying and carbonization are also carried out by direct heat transfer. The carbonizing material is continuously rotated in the interior due to the material movement with the stirrer lever. As a result, the quality of the outgoing material is balanced. Better heat transfer and uniform distribution of thermal energy is facilitated by the circulation of the gas filling the space. The high-temperature gas is supplied by a gas jet pump. During carbonization, the energy obtained by burning the pyrolysis gases produced ensures the heating of the system.
- The maximum temperature that can be set 600-800 °C.
- Biochar production capacity: 50-100 kg/h
- Outlet flue gas temperature: 300-900 C°
- Electrical power demand: 5.0 Kw

– Dimensions of the main size of the carbonizer: 6.0 x 2.4 x 3.6 m
– The weight of the machine: 3400 kg
– Temperature of exiting material: 180 C°
– Power generated by recovering the heat content of the exiting flue gas: 100 kW

Figure 1. *Flow diagram of the system*



Markings in the figure:
1. biomass into the pre-storage-feeding hopper; 2. cell dispenser; 3. angled applicator; 4. adding material to the dryer; 5. two-part dryer (paddle mixer and screw discharge unit); 6. cell dispenser; 7. application auger; 8. reactor; 9. moving and scraping structure (with drive motor); 10. biochar storage auger (and accumulated material); 11. air feeder; 12. preheating of supplied air (through the jacket of the carbon delivery and air intake pipe); 13. heating jacket pipe; 14. regulator (can be supplemented with a heat exchanger); 15. introduction of air gas mixture into the dryer; 16. introducing the gas flowing out of the dryer into the washing unit; 17. heat exchanger (heat recovery recuperator); 18. extraction of recovered heat, introduction of outside air; 19. purified flue gas

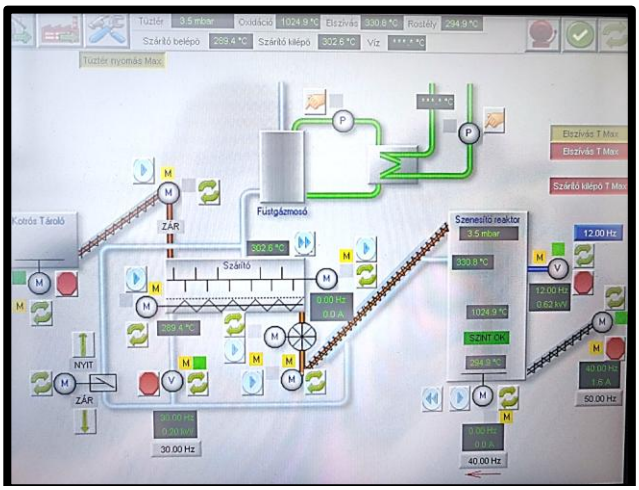


Figure 2. *The control panel of the system*

We carried out carbonization of G50 sieved hardwood fed into the machine. We examined the size distribution of the resulting carbon particles.
INTERNA and C.E. Brewer draw attention to the importance of this study, stating that biochar has different micro-sized (<2 nm), meso (2-50 nm) and macro (>50 nm) poles. Biochar with a smaller pore size cannot absorb the plant protection agent.
During the production of biochar, the activation process is the determining factor, which determines the porosity and surface of the biochar.
The grain distribution of the obtained results can be characterized with a good approximation by a quadratic curve, the peak of which is in the range of 1.0 and 1.6 mm. From the point of view of the surface evaluation, it can be considered favorable.
We examined the composition of the material in an accredited laboratory, primarily in terms of the content of various microelements. The obtained values are listed in the following table. The resulting biochar contains a wide variety of elements, among which heavy metals occur well below the permissible value.

*2.1. Examination of the composition of the obtained material **

Table 1.

Examined parameter	Unit of measure	Value
pH		10.1
Conductivity 25 °C	mS/cm	3980
Nitrite	mg/kg (L/S=10)	<0.5
Chloride	mg/kg (L/S=10)	3310
Ammonium	mg/kg (L/S=10)	<1
Nitrate	mg/kg d.m.	<50
Sulfate	mg/kg d.m.	<250
TC	m/m% d.m.	50.2
TOC	m/m% d.m.	44.6
CEC	cmol+/kg	9.34
Loose set density	kg/m^3	160
Ash content	m/m% d.m.	39.3
Silicon	mg/kg d.m.	6060
Magnesium	mg/kg (L/S=10)	127
Calcium	mg/kg (L/S=10)	24
Phosphorus	mg/kg (L/S=10)	1070
Sulfur	mg/kg (L/S=10)	52
Molybdenum	mg/kg (L/S=10)	<0.5
Boron	mg/kg (L/S=10)	<2
Iron	mg/kg (L/S=10)	0,5
Potassium	mg/kg (L/S=10)	12700
Arsenic	mg/kg d.m.	<1
Mercury	mg/kg d.m.	<0.1
Cadmium	mg/kg d.m.	<0.3
Cobalt	mg/kg d.m.	<1
Chromium	mg/kg d.m.	3
Molybdenum	mg/kg d.m.	<1
Nickel	mg/kg d.m.	2
Lead	mg/kg d.m.	<1
Copper	mg/kg d.m.	6
Selenium	mg/kg d.m.	<0.3

** Examination date: 2022.09.27. (d.m. – dry material)*

We investigated PAH compounds (polycyclic aromatic hydrocarbons, including phenanthrene, catechol, pyrene, etc.) separately, as these compounds bind less on surfaces. Our obtained values comply with EU standards (<0.05%).

3. Conclusions

Biochar is significantly different from coal, which contains many harmful substances, but also differs from the coal used in medicine, which is used for purification in various processes due to its aggressive properties (water, pharmaceutical industry, etc.). By breaking down biomass species with a high cellulose content in the material, the so-called we dealt with pyrolysis processes, in which coal, oil and gas are produced depending on the decomposition temperature. The coal (biochar) obtained during this process is used to improve soils, to increase the carbon content of the soil, and to use gas and oil as propellants and to produce mechanical and electrical energy. In pyrolysis technology, biomass is heated at a higher temperature in an oxygen-free environment. As a result, the organic materials "crack" and the resulting biochar has a significant absorbent capacity due to its large surface area. The incineration process differs from the process in that the amount of carbon dioxide produced is incomparably less and it moderates the greenhouse gas emissions that cause warming.
The amount of biochar is significantly influenced by the pyrolysis temperature, the raw material and the pyrolysis technology.
According to research, the replacement of biochar in the soil and growing media has many advantages, but its application should only

be carried out under controlled conditions. The biochar that enters the soil is beneficial for the soil structure, mediates the absorption of nutrients from the soil for plants, affects the pH value, increases the soil's water-holding capacity, but also binds toxic substances in the soil, such as heavy metals. The production of biochar by pyrolysis is a system that does not significantly affect the closed environment, which enables the use of biological waste in the circular nature model.

4. References

1. M.I. Jahirul, M.G. Rasul, A.A. Chowdhury, N. Ashwath.: 2012 Biofuels production through biomass pyrolysis – a technological review, Energies 5 - 4952– 5001.
2. M.K. Awasthi, M. Wang, H. Chen, Q. Wang, J. Zhao, X. Ren, D.-S. Li, S.K. Awasthi, F. Shen, R. Li, Z. Zhang, Heterogeneity of biochar amendment to improve the carbon and nitrogen sequestration through reduce the greenhouse gases emissions during sewage sludge composting, Bioresour. Technol. 224 (2017) 428–438.
3. S. Pang, Advances in thermochemical conversion of woody biomass to energy, fuels and chemicals, Biotechnol. Adv. 37 (2019) 589–597.
4. J. Wei, C. Tu, G. Yuan, Y. Liu, D. Bi, L. Xiao, J. Lu, B.K.G. Theng, H. Wang, L. Zhang, X. Zhang, Assessing the effect of pyrolysis temperature on the molecular properties and copper sorption capacity of a halophyte biochar, Environ. Pollut. 251 (2019) 56–65.
5. M.K. Awasthi, M. Wang, H. Chen, Q. Wang, J. Zhao, X. Ren, D.-S. Li, S.K. Awasthi, F. Shen, R. Li, Z. Zhang, Heterogeneity of biochar amendment to improve the carbon and nitrogen sequestration through reduce the greenhouse gases emissions during sewage sludge composting, Bioresour. Technol. 224 (2017) 428–438.
6. J. Liu, Y. Ding, L. Ma, G. Gao, Y. Wang, Combination of biochar and immobilized bacteria in cypermethrin-contaminated soil remediation, Int. Biodeter. Biodegr. 120 (2017) 15–20.
7. Czégény, Zs., et all: 2020 Comparison of hydrothermal carbonization and torrefaction of azolla biomass: Analysis of the solid products, Journal of Analytical and Applied Pyrolysis 149 p. Paper: 104844 https://www.bayzoltan.hu/wp-content/uploads/2017/09/Cz%C3%A9g%C3%A9ny-Zsuzsanna_termikus_modszerek.pdf (download: 2023)

New optical method in laser phototherapy

Alexander Gisbrecht *, Luchezar Avramov
Institute of Electronics, Bulgarian Academy of Sciences, Sofia, Bulgaria
agiz@abv.bg

Abstract: *In this study we investigate the kinetics of oxygen tension (pO_2) in skin tissue under the influence of the transcutaneous laser irradiation. The results of in vivo experimental measurements of pO_2 by a method of transcutaneous oxygen monitoring (TcOM) are presented. The results show that under laser irradiation the value of tissue oxygenation increases and after approximately 10 minutes of exposure exceeds its initial level up to 1.6 times. The observed increase in pO_2 indicates the process of photodissociation of oxyhemoglobin (HbO_2) in skin blood vessels, which results in local O_2 increase in the tissue. Such laser-induced enrichment of tissue oxygenation can be used in phototherapy of pathologies, where the elimination of local tissue hypoxia is critical.*
KEYWORDS**:** *HEMOGLOBIN, TISSUE OXYGENATION, PHOTOTHERAPY, PHOTODISSOCIATION*

1. Introduction

Tissue oxygenation plays a key role in the cell metabolism, energy supply and life activity of an organism. Many diseases such as diabetes, burns, bedsores and wounds are accompanied with an insufficient supply of oxygen to the tissues [1,2]. Also, the deficit of oxygen in cancer tissue is a major problem limiting the efficiency of photodynamic therapy [3,4]. The wound healing process directly depends on the oxygen pressure in skin tissue ($TcPO_2$). For example, the additional supply of oxygen leads to an increase in the rate of collagen synthesis and an improvement of the protective functions of the skin. It is currently accepted that the adequate tissue oxygen concentration for normal cell metabolism should exceed 40 mmHg. Injuries, infections, and diseases can reduce this vital tissue oxygen level down to almost zero, which indicates tissue hypoxia. Optimal tissue healing occurs when the pO_2 rises to between 50 and 80 mmHg. Consequently, the value of pO_2 is an objective indicator for evaluating the local state of the tissue and the efficiency of cell metabolism. Controlling this mechanism provides the possibility for biological stimulation with a therapeutic effect.

In clinical practice the commonly used method for elimination of tissue hypoxia is ventilation of the lungs by pure O_2 at normal and hyperbaric pressure. Sustained periods at such pO_2 levels can only be realized through the use of hyperbaric oxygen therapy [5], but it leads to the risk of oxygen intoxication. Moreover, this approach has not had a broad clinic application for local treatment due to technical difficulties. Thus the problem of local hypoxia elimination in biological tissues remains significant and the methods of influencing the delivery of oxygen to the tissue are of considerable interest. One of these methods is the light radiation in the optical spectral range.

A new approach for the optically induced increase in the local oxygen concentration due to photodissociation of oxyhemoglobin in cutaneous blood vessels has been proposed in [6]. The absorption of light by blood HbO_2 is connected with the following photochemical and photophysical processes. It is known [7] that absorption of a photon with the activation energy leads to the dissociation of a part of the molecules, resulting in the release of molecular oxygen and the formation of deoxyhemoglobin. Photodissociation is one of the simplest chemical reactions when a compound dissociates under the action of radiation. .

$$HbO_2 + h\nu \rightarrow Hb + O_2$$

The quantum efficiency of the photodissociation of oxyhemoglobin is high and reaches 10 % in a wide visible spectral range [7]. The photophysical process is connected with the non-radiative dissipation of the absorbed excitation energy, as the heat generated in this process is transferred to the blood capillaries with a characteristic thermal relaxation time of ~ 0.05-1.2 msec. Estimates show that in the typical case a local increase in temperature of only 0.1 - 0.5 ^{0}C may be expected [8]. Such a small rise in the local temperature may produce little improvement in the capillary microcirculation of the blood and can hardly stimulate the cell metabolism [9].

We suppose that in the case of low energy irradiation the most important process is the photodissociation of HbO_2. Experimental proof of the suggested concept has been demonstrated in [10,11]. The observed local decrease in the level of arterial blood saturation during laser irradiation clearly proves the induced photodissociation of HbO_2 in blood capillary vessels. The efficiency of this process depends on the wavelength and the output power of the laser radiation, the blood vessels density in the irradiation area, the optical properties of the skin and the depth of the blood vessels in the tissue. It is interesting but still unclear what fraction of O_2 molecules released by photodissociation can escape from the heme pocket and diffuse through the cell membranes and capillary walls, thereby increasing the tissue oxygen pressure. However, relevant studies mainly refer to *in vitro* experiments or studies of individual cases [12-15]. No investigations have been carried out as yet into whether an immediate improvement in the oxygen saturation occurs *in vivo*, which would be a key to wound healing.

In this paper, we present an experimental study *in vivo* of the pO_2 rate in skin under the influence of local transcutaneous He-Ne laser (628 nm) irradiation.

2. Materials and methods

The transcutaneous oximeter method, based on the principle of measuring the oxygen tension pO_2 in arterial blood, is a method for direct registration of gases that dissolve in the blood plasma. The choice of this method is determined by the fact that the TcOM allows the direct determination of the oxygen pressure in the skin tissue, in units of mmHg. Measurements were carried out using a transcutaneous oxygen monitor "Radiometer" TCM-4 with a Clark-type polarographic sensor with a diameter of 2.5 mm ($TcPO_2$ electrode) that consists of a platinum cathode and silver anode, electrolyte and an oxygen permeable membrane; a heating section and an electronic system for measuring and controlling the sensor temperature. (Fig.1 a).

The measurements were carried out on three volunteers, in the conditions of an absence of physical and emotional stress, in a seated position and at room temperature. All the procedures performed in the study were in accordance with the ethical standards. Human studies in the article were approved by the relevant Institutional Review Board. During an individual measurement, all conditions were identical for all the subjects and remained constant throughout the measurement.

The measurement procedure is as follows. The sensor is placed on the skin of the forearm, an area with high capillary pressure then it is heated to 43ºC (Fig. 1 b).

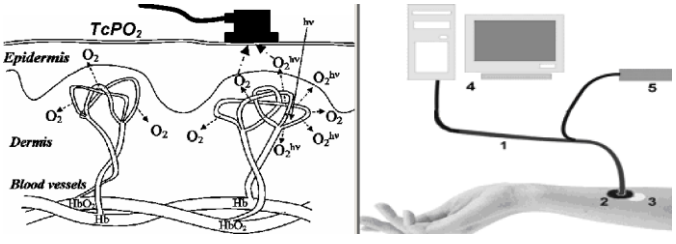


Fig. 1 Model of oxygen diffusion in tissue (a) and measurement (b) of tissue oxygen tensions: 1 - Clark sensor, 2 - electrolytic cell, 3 - irradiating zone, 4 - monitor TCM, 5 - He- Ne laser

Under the influence of temperature, oxygen diffuses from the capillaries into the epidermis and then into the electrolytic cell, where it is measured. The value of oxygen tension, measured transcutaneously ($TcPO_2$), corresponds to the value of pO_2 measured in the arterial blood plasma. The errors in the determination of $TcPO_2$ come from the skin thickness, the subcutaneous blood flow and the physiological factors influencing O_2 delivery to the skin surface (decrease in the blood flow, the arterial blood pressure, the vasoconstriction occurrence). Since oxygenation depends on a number of factors, the laser radiation was only used once and the measurements were carried out immediately, in order to obtain direct observation of the effect of radiation.

3. Results

For local irradiation of cutaneous blood vessels, a He-Ne (632,8 nm) laser was chosen. As shown in the model calculations of the absorption spectra at the tissue depth [6], this wavelength lies in the effective absorption band of HbO_2 and penetrates deep into the skin issue. The laser output is 1 mW, and the beam diameter – 2,5 mm, providing a laser power density of ~ 20 mW/cm2. First, after thermostabilization, the initial oxygen pressure in the tissue is measured, then the laser radiation is applied. In Fig.2 the measured values of pO_2 in dependence on the irradiation time are presented. The obtained results are normalized to the initial oxygen pressure value.

As can be seen, the tissue oxygen tension increases for all three patients (although with different rates) and reaches saturation levels after approximately 10 minutes of exposure. The value of $TcPO_2$ in the irradiation zone depends on the time of exposure and the properties of the tissue that differ considerably for all three cases. It is significant to note that this growth of $TcPO_2$ is due to the additional O_2 in the tissue as a result of the laser-induced photodissociation of HbO_2. The oxygen released from HbO2 first increases the pO_2 in the blood plasma and then diffuses into the surrounding tissue. The value of the $TcPO_2$measured transcutaneously increases about 1.6 times compared with its initial value. Generally, the diffusion occurs in three directions: toward the skin surface, inward to the muscle tissues and some is carried away by the blood flow. If we assume that the same amount of oxygen is carried away in all these directions, we should expect an increase in pO_2 in the arterial blood plasma by about a factor of 4.8.

It is interesting to note that the obtained value of pO_2 realized by laser-induced photodissociation of HbO_2 is comparable with the one typically reachable by the conventional method of hyperbaric oxygen therapy [5].

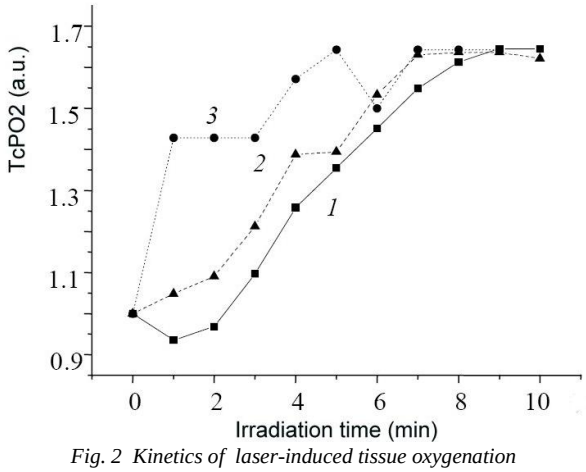


Fig. 2 Kinetics of laser-induced tissue oxygenation

4. Discussion

In contrast to other (in vitro) studies, this study was carried out under in vivo conditions, so it is possible to make statements about the feasibility of the measurement effect.

Thus, we demonstrate that after prolonged irradiation (several minutes), a certain fraction of oxygen molecules released due to photodissociation of HbO_2 diffuses in the surrounding tissue and increases the oxygen partial pressure. Since the values of oxygenation depend on a number of factors, the results of this study cannot identify any immediate effect of the radiation on the oxygenation in tissue in vivo. Thus, it would be reasonable if further studies on the immediate effects on oxygen saturation would take into account additional parameters, such as a variation in the wavelength radiation. The results obtained should correlate with the characteristics of light propagation in blood-filled tissues. The visible light in the blue and green spectral range has a small penetration depth into skin tissue, because of their proximity to the absorption bands of some basic skin chromophores such as HbO_2 and melanin. Red and especially near infrared radiation penetrates much deeper into the soft tissues and plays a dominant role in the absorption of laser radiation by oxyhemoglobin in the deeper layers of tissue blood vessels. Such possibility to increase the free oxygen content in tissues can be applied in clinical practice for treatment of a number of diseases related to problems with the microcirculation and oxygen supply and therefore requires further investigations.

It is very important to note that photodissociation of HbO_2 produces only molecular oxygen as a by-product and not singlet oxygen. Lepeshkevich in [16] uses time-resolved luminescence spectroscopy in the near-infrared region and does not measure detectable quantities of singlet oxygen during the photodissociation of O_2 from myoglobin and hemoglobin..

5. Conclusions

The obtained results demonstrate that the laser-induced photodissociation of oxyhemoglobin, whose main biological function is the transport of molecular oxygen, gives the possibility for an additional oxygen supply and allows the development of optical methods for tissue hypoxia elimination. Monitoring the kinetics of tissue oxygenation gives the possibility to control the normal aerobic cell metabolism.

It is shown that the efficiency of laser-induced oxygenation is comparable with the method of hyperbaric oxygenation, at the same time providing advantages by the local action. Advances in technology can lead to further improvement in the management of patients with wounds.

Acknowledgments

The research is supported partially by Bulgarian Science Fund under contract DO 02-112/2008

References

1. Leaper, D 2007, *Int. Wound. J,.3*. № 5
2. Hopf H., Rollins M. 2007, *Antioxidants and redox signaling*, 9, 1183
3. Lui H., Anderson R.1993 *Dermatol. Clin*., 11, 1
4. Pass H, 1993 *Natl. Cancer Inst*., 85, 443
5. Tibbles P, Edelsberg J. 1996, *N. Engl. J. Med*., 334, 1642
6. Asimov,M. et al.1998. *J. Appl. Spectrosc*., 65, 877
7. Saffran W, Gibson Q. *J. Biol. Chem*., 252, 7955.
8. Basford J. 1989 *Lasers Surg. Med*., 9, 1
9. Rogatkin D., Dunaev A.2014 *Journal of Medical Research and Development*, **3**, 100
10. Asimov M. et al. 2001 *Proc. SPIE*., 4397, 390
11. Yabushita I., Kobayashi T.2010, *Spectroscopy*, 24, 333
12. Liu P., Zhu Z. 2012 *J. Biomed. Optics*, 17, 125002
13. Heu F. et al. 2013 *Laser Ther*., 22, 21
14. Matsuo H. Morimoto Y. *Lasers Med. Sci*., 15, 181
15. Stratonnikov A., Ermishova, *Quantum. Electron.*, 32, 917
16. Lepeshkevich S,, Stasheuski A. *J. Photochem. Photobiol. B*., 120, 130

Antibacterial Coatings Containing Nanodiamonds

Anna Karczemska[1,*], Michał Szczypiński[9], Dariusz Witkowski[1], Józef Doering[1], Radosław Wach[2], Bożena Rokita[2], Alicja Olejnik[2], Beata Kolesińska[3], Justyna Frączyk[3], Anna Gajda[3], Sylwia Magdziarz[3], Totka Bakalova[4], Lucie Svobodova[4], Petr Exnar[5], Irena Slamborova[5], Petr Louda[4], Ahmed El Mallul[6,7,1], Remigiusz Pawelczyk[8], Stanisław Mitura[9]
Institute of Turbomachinery, Lodz University of Technology, Poland[1]
Institute of Applied Radiation Chemistry, Faculty of Chemistry, Lodz University of Technology, Poland[2]
Institute of Organic Chemistry, Department of Chemistry, Lodz University of Technology, Poland[3]
Faculty of Mechanical Engineering, Department of Material Science, Technical University of Liberec, Czech[4]
Faculty of Science, Humanities and Education, Department of Chemistry, Technical University of Liberec, Czech[5]
Department of Surgery, Faculty of Medicine, University of Radom, Poland[6]
Libyan Academy for Postgraduate Studies, Medical School, Libya[7]
Independent Public Health Care Center in Szamotuły, Poland[8]
TERMEX, Koszalin, Poland[9]
anna.karczemska@p.lodz.pl

Abstract: *The aim of this research is to obtain coatings with high antibacterial properties and low toxicity, for various applications. Sol-gel method was employed to manufacture coating comprising carbon nanoparticles (CNP) of nanodiamonds (ND). Methods of dip-coating and spraying were developed and optimized. The technology was adopted to automatic process using designed and manufactured laboratory and semi-industrial spraying and curing apparatus.*

Keywords*: CARBON NANOPARTICLES, NANODIAMONDS, ANTIBACTERIAL SOL-GEL COATINGS, PORTABLE LABORATORY STAND*

1. Introduction

Problem issue is a potential epidemiological threat - the spread of bacteria through people touching various surfaces at sensitive areas (hospitals, clinics, public transport, shops, schools, etc.). Problem arises in large human agglomerations and with people migrations (in EU millions of people travel from place to place every day). Problem are also bacteria from the other continents brought with tourists and immigrants to EU countries.

The aim of this research and solution to the above mentioned problems is the development of antibacterial coatings, obtained by sol-gel method, containing carbon nanoparticles (CNPs) [1-6]. In presented investigations the sol-gel technology of coatings deposition was applied. Such coatings could find many every-day applications (in public transport, supermarkets, toilets, etc.) but also can find applications in medicine.

2. Sol-gel coatings – deposition methods

A sol-gel layer is created thanks to the polymerization process just after it is deposited on the surface of the desired object. There exist various methods of transferring the liquid sol to the surface of the solid body that is desired to be coated. One can propose dip coating, spray coating and spin coating.

The laboratory at the Lodz University of Technology, Institute of Turbomachinery is equipped with two homemade stands designed for sol-gel layer deposition – a spray coating stand and a dip coating stand presented in Figure 1 and Figure 2.

Spray coating is done by spraying the sample surface with the sol solution using the aerograph (9). An aerograph is supplied with the compressed air coming from the electric-powered compressor (3) connected to a standard 230 V socket. Since the process should be as repeatable as possible a holder (8) attached to the holder base (4) is used to hold the aerograph in place. The horizontal bar present in the holder base (4) assembly can be repositioned vertically to control the spraying distance.

The maximum repeatability of the process is also ensured by the conveyor belt assembly (6). This device is used to move the sample at a constant speed while the spraying takes place. This action is important to obtain a fairly uniform sol-gel layer on the sample surface. Similarly to the dip coating stand described in section 2a the rotational speed of the electrical motor (5) is controlled using a power supply (1) equipped with a potentiometer that allows the change of the supplied voltage and thus the velocity of the belt. The belt (7) on which the sample is placed is stretched between two pulleys, one that turns freely and the second which is attached to the motor (5). A horizontal movement of the conveyor belt is controlled by the panel (2) which allows for engagement and disengagement of the motor as well as alters the direction of its rotation.

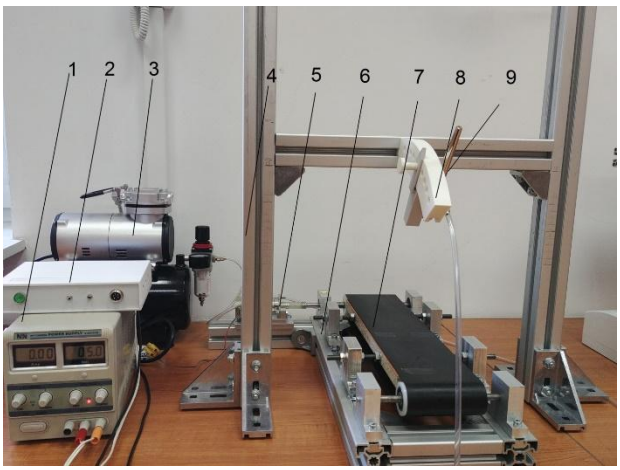


Fig. 1 *Spray coating stand – Lodz University of Technology.*

In a case of dip coating, a sample (1) is held in place by a clamp (2) and has to be drawn in and out of the sol solution (1) at a specific speed (4 cm/s). This task is accomplished thanks to the mechanism.
A clamp (2) is attached to the flat bar (4) that is screwed to the block (8). The block possesses a threaded connection with the rotating lead screw (9) and is capable of movement between two limitation blocks connected with the rod (10). A screw rotates thanks to the electric motor (12) located on the shelf (11). The rotational speed of the motor and thus the vertical movement speed of the sample is controlled by manipulating the voltage supplied to

the motor by the power supply (6). A control panel (7) is used to engage the motor and to alter the upward and downward movement of the sample (clockwise or counter-clockwise movement of the lead screw). The whole assembly is mounted on the stable base (5).

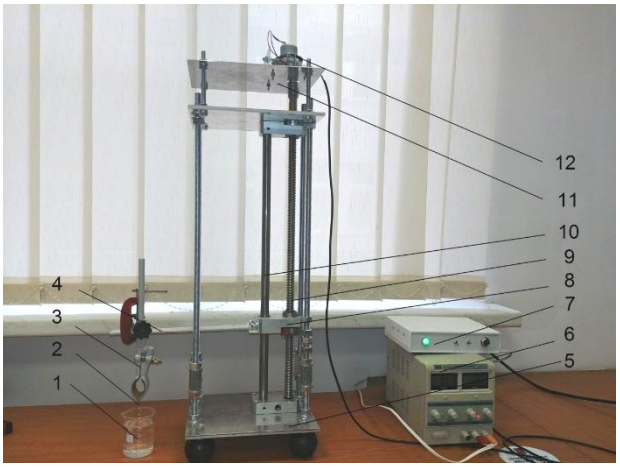


Fig. 2 *Deep coating stand – Lodz University of Technology.*

Both stands presented in Figures 1 and 2 are controlled by the same control panel and use the same power supply for the electric motors. In the case of the spray coating stand the power supply is connected to the electric motor that drives the conveyor belt. The samples move while the sol is being sprayed. An aerograph is mounted on the dedicated stand that allows to keep it in place and allows to keep the same distance from the sprayed surface throughout the process. By increasing the voltage applied to the motor one can regulate the velocity of the belt. During the laboratory work, the voltage was set to 6.5 V which corresponded to the linear velocity of the sample equal to. 6 cm/s. The spray coating procedure requires two layers of the coating to be deposited. A minimum of 3 minutes of drying time is required between the consecutive spraying of the layers.

A dip coating stand allows the upward and downward movement of the sample thanks to the rotating leads screw which is driven by the electric motor. Counterclockwise rotation of the lead screw causes the downward movement of the clamp with the mounted sample. During the dip coating procedure, one must immerse and withdraw the sample from the sol solution at a given speed which amounts to 4 cm/s. To do this the voltage applied to the motor has to be equal to 12.8 V for the downward movement and 13.5 V for the upward movement. A 1 minute waiting time is required between the immersion and withdrawal of the sample.

3. Sol-gel layer curing

After the sol-gel for both the dip-coating and spray-coating process, the hardening process followed by a 30-minute drying time is carried out. In the laboratory at the Lodz University of Technology, Institute of Turbomachinery there are three possible ways for the sol-gel layer hardening: conventional curing done with a furnace, infrared curing under the IR lamp, and UV curing. During the laboratory work the most frequently used methods were the furnace and IR curing since there was a doubt that the photoinitiated that needs to be excited by the UV radiation to begin the polymerization process possesses absorption maxima at the ranges of the UV spectrum that are not corresponding to the emission spectrum of the available UV lamp. The curing temperature for the sol-gel layers is 150°C and is easily achievable in the furnace and under the available IR lamp (that was tested before it was used for the hardening process). Hardening time was a subject of experiments for both furnace and IR curing however the recommended minimum hardening time was equal to one hour.

4. Portable Laboratory Stand

In the TERMEX company, in cooperation with the Lodz University of Technology, a laboratory stand was constructed for the production of coatings on different kinds of samples (Fig.3). The main module of the station is a CNC machine (computer controlled numerical device) equipped with a spray head that allows the application of sol on the samples. The open-frame construction is made of 20x40 aluminum profiles. The device has two motor guides. The spray head moves in three axes X,Y,Z using NEMA-17 bipolar stepper motors. The device is controlled by the BlackBox x32 driver from OpenBuilds USA supporting the grblHAL firmware.

The head moves over a 400x400 mm operating table with a glass surface, on which the samples are placed. In order to carry out polymerization, the surface of the operating table is heated with a silicone heating mat with a power of 1000 W, enabling the required temperature of 150°C to be reached. In addition, the station was equipped with an infrared radiation generator consisting of 4 medium-wave infrared radiators with a golden Heraeus reflector. The radiators have a heating length of 300 mm and their power is 500 W each (2000 W in total). The distance of fluorescent lamps from the operating table is adjustable. The infrared radiation generator is designed to improve the polymerization process. The operation of the heating mat and infrared radiators is controlled by a two-channel ESCO PT20+ temperature controller equipped with a Pt100 temperature probe, which was placed in the operating table.

The spray head itself has been designed in such a way that the atomizing nozzle can be easily replaced (e.g. with a different geometry). EXAIR (USA) circular spray nozzles are installed in the unit. The mixing of the air with the liquid takes place inside the nozzle. The nozzles are made of stainless steel type 303. Sol and compressed air are supplied to the nozzles, however, the nozzles used differ in the method of supplying the liquid. One of them is siphon fed and there is no need to supply sol under increased pressure. In this case, the liquid is sucked in using compressed air. The sol is supplied to the nozzles using a laboratory peristaltic pump, Lead Fluid BQ80S, which provides a flow in the range of 0.005-20 cm^3/min. Compressed air is produced by an oil-free Stanley Fatmax TABLET compressor. The pressure in the laboratory stand system is regulated by the compressor pressure reducer and by the reducer located on the installed 3-filter separator (dehydrator), which is designed to remove moisture and impurities with a size of approx. 2 microns.



Fig. 3 *Portable Laboratory Stand – TERMEX..*

5. Coatings

Layers with the use of NDs of various modifications and concentrations were produced, which were subjected for further material testing and to biological tests. The study investigates the

impact of nanodiamond concentration, deposition parameters, and temperature control during hardening process on the structural, mechanical, and tribological properties of the sol-gel coatings. Characterization techniques, including scanning electron microscopy, confocal microscopy and tribological tests have been performed (Fig.4-5).

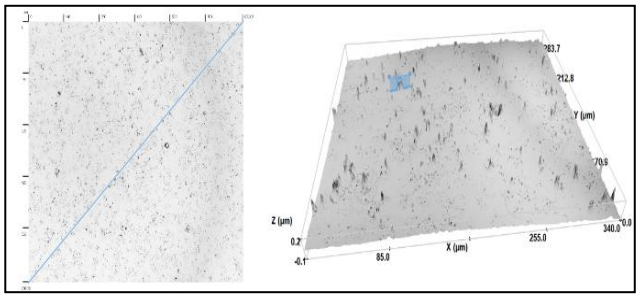


Fig. 4 *Example of the obtained sol-gel coating containing nanodiamonds – confocal microscopy (Liberec).*

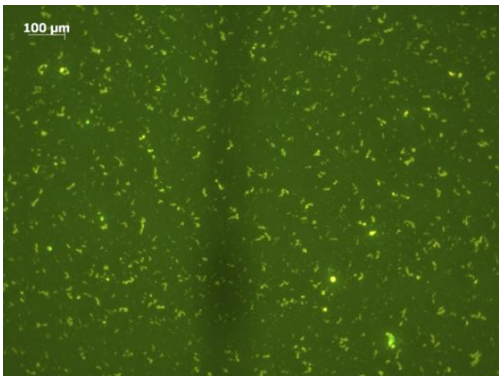


Fig. 5 *Example of the obtained sol-gel coating containing modified fluorescence nanodiamonds – fluorescence microscopy (Lodz University of Technology).*

An important research was carried out on the curing of sol-gel layers, in which infrared (IR) or ultraviolet (UV) radiation was used, conventional curing in an oven was used as a reference method. The layers were applied by spraying and deep coating methods. The optimal curing parameters such as the distance of the sample from the IR lamp, the required power and exposure time for the IR curing process were determined. Measuring devices were used to monitor the temperature: a pyrometer, a thermal imaging camera and a thermocouple (Fig.6).

Temperature distribution tests were performed. A thermal imaging camera and a thermocouple were used. Tests were also carried out using a UV lamp that emits light with a wavelength of λ=405 nm. The tests were carried out for different exposure times.

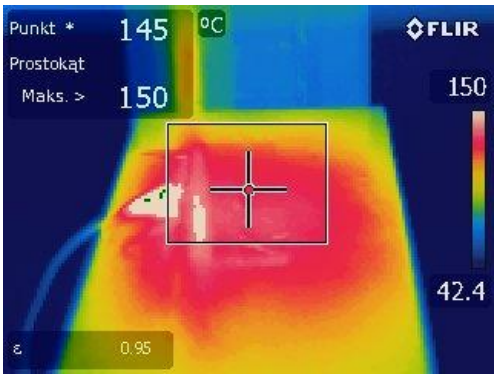


Fig. 6 *An example of IR curing monitoring using a thermal imaging camera (Lodz University of Technology).*



Fig. 7 *Example of the obtained antibacterial sol-gel coating on the door handle (cooperation with the hospital in Szamotuły, Poland).*

6. Conclusions

Tribological tests allowed to compare different samples produced with different methods. In order to increase the adhesion of the layer to the substrate, a procedure of cleaning of the samples surface was elaborated. The developed know-how and the results of the work have been implemented in semi-industrial scale. The findings of this study provide valuable insights into the deposition of sol-gel coatings with nanodiamonds, showing the potential of these coatings for various engineering and biomedical applications (Fig.7). Moreover, the portable laboratory stand offers a practical tool for researchers and engineers to explore and exploit the benefits of nanodiamond-enhanced sol-gel coatings in a controlled and reproducible manner.

7. References

1. I. Šlamborová, V. Zajícová, J. Karpíšková, P. Exnar, I. Stibor, Materials Science and Engineering: C 33 (2013) 265–273.
2. B. Rokita, L. Svobodowa, I. Slamborova, P. Exnar, P. Louda, K. Mitura, R. Wach, D. Witkowski, A. Karczemska; *31st PSB Annual Conference: Biomaterials in Medicine and Veterinary*, Rytro 13-16.10.2022.
3. R. Wach, B. Rokita, L. Svobodowa, I. Slamborova, P. Exnar, P. Louda, K. Mitura, D. Witkowski, A. Karczemska; *3rd BIOMAH Conference Biomaterials and Novel Technologies for Healtcare*, Rome 18-21.10.2022
4. J. Doering; *Diploma Thesis. Lodz University of Technology* (2022)
5. M. Szczypiński, S.Mitura, P. Louda, I.Slamborova, P.Exnar, A.Bartosik, A. El Mallul, A.Karczemska*;* Nanosmat Manchester UK 2018
6. M.W. Pośpiech, K. Prałat, A. Bartosik, I. Lovetinska Slamborova, P. Exnar, M. Szczypiński, P. Louda, D. Laskowska, A. Karczemska, *11th Innovative Technologies for Medicine ITMED*, 26-28 June 2018, Manchester, UK

Acknowledgments

This research was funded by The National Center for Research and Development (project AnBaCo „Antibacterial Coatings Containing Carbon Nanoparticles Obtained by Sol-Gel Method" number M-ERA.NET 2/2019/3/2020), and by the Technology Agency of the Czech Republic within the Epsilon Program (project number TH71020001).

The study of the corrosion zinc-nickel coated ST2 stainless steel

Julieta Daniela Chelaru[1], Maria Oana Felecan[2]
Babes-Bolyai University[1], Electrolytic Coating SRL[2]
E-mail: julieta.chelaru@ubbcluj.ro; oana.h1093@yahoo.com

Abstract: *In the present work, the corrosion of Zn-Ni coated steel in the presence of acetic acid was studied. Corrosion tests were carried out in salt spray and the corrosion rate was determined by the weight loss method. The results showed that the Zn-Ni layer acted as sacrificial coatings on steel, the acetic acid, even if it is a weak acid. Also, in this paper, a simulation was carried out regarding the corrosion protection of steel attacked by acetic acid using a sacrificial anode (Zn alloy). The results obtained from the simulation agree with the experimental ones.*
KEYWORDS: *STEEL CORROSION, SALT SPRAY TEST, CORROSION RATE, COMSOL* Multiphysics, Zn-Ni COATINGS

1. Introduction

Corrosion is one of the most common problems in the process industry due to loss of materials, or degradation of mechanical and chemical properties [1, 2]. Since most machines in the process industry are made of steel, the corrosion of steel in various environments is a constant concern. The increase in corrosion resistance is significant both from an engineering and economic point of view by increasing the life of machines. Consideration should also be given to reducing the risk of accidents or disasters due to corrosion [1]. One of the most used methods for the protection of the steel surface is coating [1]. Metallic coating is efficient and practical in protecting steel against corrosion in different environments [3-5]. In this study, the steel mild plate was coated with zinc-nickel (Zn-Ni) alloy using electrodeposition in a hull cell. The covering of the steel plates was done inside the hull cell. The corrosion tests were carried out in the presence and absence of acetic acid, in a salt spray chamber.
Based on the studies acetic acid enhances the corrosion rate of steel [6] by accelerating the cathodic reaction [7, 8]. A method of cathodic protection against steel corrosion is the use of a sacrificial anode [1, 9]. This method is often used due to its simplicity. The protection of a steel plate using a sacrificial anode (Zn alloy) was simulated in COMSOL Multiphysics (corrosion module).

2. Experimental

2.1 Electrodeposition

The samples used were steel plates with a standard size: 100 mm length, 70 mm width, and 3 mm thickness. The chemical composition of the steel used in the experiment: 0.12 % C, 0.6 % Mn, 0.37 % Si, 0.045 % S, 0.045 % P.
The tested plates were carefully cleaned to remove impurities. A Hull cell was used to apply the coating layer (Zn-Ni). The parameters were: 250 ml electrolyte, 20 minutes, and current density 1 A/dm^2. Table 1 presents the chemical composition of the bath.

Table 1 *The composition of electrolyte*

Compounds	Concentration [g/l]
Zn	8.34
Ni	1.84
NaOH	124
CO_3^{2-}	41.58

2.2 Salt spray test procedure

To evaluate the corrosion behavior of protective coatings (Zn-Ni) in the presence and in the absence of acetic acid, use the salt spray test.
For tests, a salt spray chamber type CC450iP (ASCOTT) was used. A salt solution, with 5% sodium chloride (NaCl) solution, was prepared and atomized into a fine mist within the chamber. The mist consists of tiny salt particles suspended in the air, replicating the corrosive nature of salt-laden atmospheres. The samples were maintained in the salt spray chamber for a period of 72 hours (Figure 1).

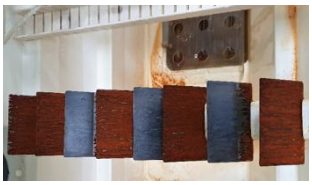


Fig. 1 Arranging the samples in the salt spray chamber

2.3 Corrosion rate

The corrosion rate was determined using the following formula [2]:

$$CR = \frac{\Delta M}{A \cdot t} \qquad (1)$$

Where: CR represents the corrosion rate; ΔM= weight loss (m1-m2),
A = 70 cm^2 is sample surface area; t=time
An important parameter for measuring corrosion resistance is the corrosion current density (i_{corr}). Based on Faraday's law, the corrosion rate (CR) can be calculated by the following equation:

$$i_{corr} = \frac{I_{corr}}{A} = \frac{CR \cdot \rho}{K \cdot EW} \qquad (2)$$

Where: K = 3272 (mm / A·cm·year) is the corrosion rate constant; I_{corr} is corrosion current (μA); EW = 27.9225 g is equivalent weight of Fe; ρ = 7.874 g / cm^2 is the density of Fe

2.4 Acetic acid

Walton [8] proposed the following dissociation mechanism of acetic acid to explain the increased corrosion rate in its presence.

$H_2O + Fe^{2+}(aq) \leftrightarrow FeOH^{+}(aq) + H^{+}(aq);$ (3)
K_1=1.63*10^{-7}
$Fe(OH)_2(s) + 2H^{+}(aq) \leftarrow Fe^{2+}(aq) + 2H_2O;$ (4)
K_2=1.63*10^{-7}
$H_2O \leftrightarrow H^{+}(aq) + OH^{-}(aq);$ (5)
K_3=1.63*10^{-7}
$CH_3COOH(aq) \leftrightarrow H^{+}(aq) + CH_3COO^{-}(aq);$ (6)
K_4=1.63*10^{-7}
$CH_3COO^{-}(aq) + Fe^{2+}(aq) \leftrightarrow CH_3COOFe^{+}(aq);$(7)
K_5=1.63*10^{-7}

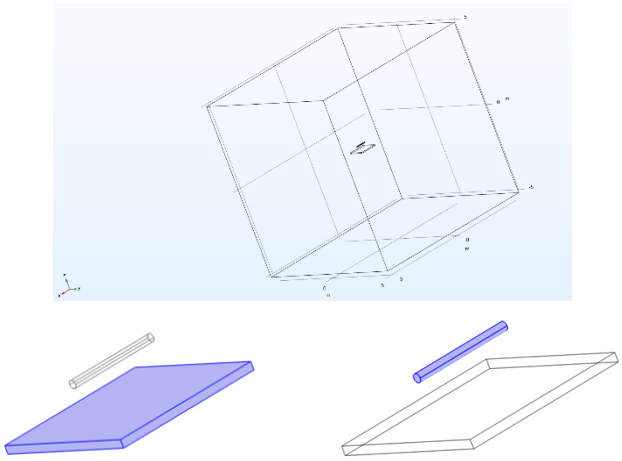
Eight aqueous species were considered in the study (Table 1) [8].

Table 2 *Diffusion coefficients for species*

Species	D [dm^2/s]	Species	D [dm^2/s]
Fe^{2+}	$0.7 \cdot 10^{-7}$	Na^+	$1.3 \cdot 10^{-7}$
H^+	$9.3 \cdot 10^{-7}$	CH3COOH	$1.1 \cdot 10^{-7}$
OH^-	$5.3 \cdot 10^{-7}$	$CH3COO^-$	$1.1 \cdot 10^{-7}$
$FeOH^+$	$1 \cdot 10^{-7}$	$CH3COOFe^+$	$1.1 \cdot 10^{-7}$

2.5 Corrosion protection of steel

Figure 2 shows the geometry analyzed in this study. The model consists of a steel plate (1m·1m·0.05m) surrounded by an electrolyte (NaCl) (volume = $1m^3$). A cylindrical sacrificial anode (Zn alloy) was used with the dimensions: 0.025m radius, and 0.6 m length.



cathode anode

Fig. 2 Model geometry

3. Results and discussion

3.1 Thickness of the coating

Table 2 *The thickness of the coatings obtained in Hull cell*

Samples	Speed deposition [µm/min]	Coating thickness [µm]	Ni [%]
1	0.229	7.406	13.70
		5.906	11.70
		3.316	12.70
		1.720	11.28
2	0.217	6.640	13.70
		5.850	11.23
		3.563	13.00
		1.830	10.97
3	0.276	9.730	13.77
		6.270	12.00
		3.513	12.83
		2.15	11.13

The coating thickness was measured at four points, after deposition. The results are presented in Table 3.

3.2 Corrosion rate

The corrosion rate (CR) and corrosion current density (i_{corr}) calculated with formulas (1) and (2). The results are shown in Table 3. It can be observed that Zn-Ni exibited corrosion protection in case of steel, in the presence of acid acetic, as expected.

Table 3 *Corrosion rate of steel in with/without Zi-Ni coating, after 80 minutes maintained in aced acetic 10%*

Samples	ΔM [g]	CR [mm/year]	i_{corr} [mA/cm^2]
Steel-	0.741	2.830	0.2439
Steel/Zn-Ni	0.187	0.714	0.0616

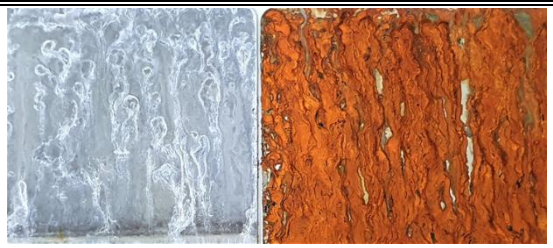


Fig. 3 *The steel plates after 72 hours: (a) with and (b) without Zn-Ni coating, in the presence of acetic acid 10 %*

The protection of the Zi-Ni coating was put in evidence also by visual inspection of the corroded surfaces of the samples (Figure 3). It can be observed that in the case of uncoated steel, the corrosion products layer is not uniform, with severely corroded areas. Based on the brown color of the steel surface, it can be assumed that the products of the corrosion layer contain iron oxides. Otherwise, in the case of steel coated, the aspect of the surface is more uniform, and the presence of rust is not visible.

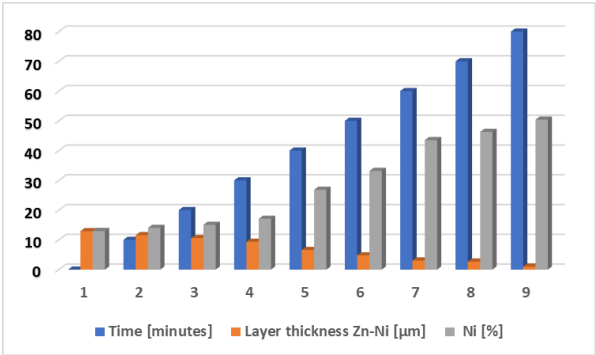


Fig. 4 *The behavior of Zn-Ni coating in acetic acid (10%)*



Fig. 5 *The brittleness of steel plate after 72 hours of exposure to salt spray*

For a better understanding of the phenomenon, the behavior in acetic acid of a steel plate coated with Zi-Ni was analyzed. The coating thickness and percentage of Ni in the layer were determined. Determinations were made every 10 minutes. The results are presented in Figure 4. Based on the test performed, it can be concluded that acetic acid, even if it is a weak acid, pickling almost the entire Zn-Ni coating. The increase in the percentage of Ni in the coating may be due to the formation of Ni oxides in it. Also, in the presence of acetic acid, the Zn dissolves more easily compared with Ni. It can be presumed to be the appearance of the dezincification phenomenon [5].

In the case of the steel plates uncoated with Zn-Ni, after the appearance of rust, embrittlement of the base material could also be observed (Figure 5), the plate broking at a simple bending test. The steel plate was maintained in acetic acid (10%) before exposure 72 hours in a salt spray chamber.

3.3 Simulation results

During the simulation, the steel plate and the sacrificial anode were surrounded by electrolyte as in Figure. 6. In this study was used

steel in the presence of acetic acid (1.6mM). Zn alloy was used as a sacrificial anode. Zn is a common sacrificial metal used in a marine environment [1]. The Zn activity has consequently the protection of the steel surface against the electrochemical corrosion process. As can see in Figure 7 the red color zones are of anodic current and the blue color indicates a cathodic current.

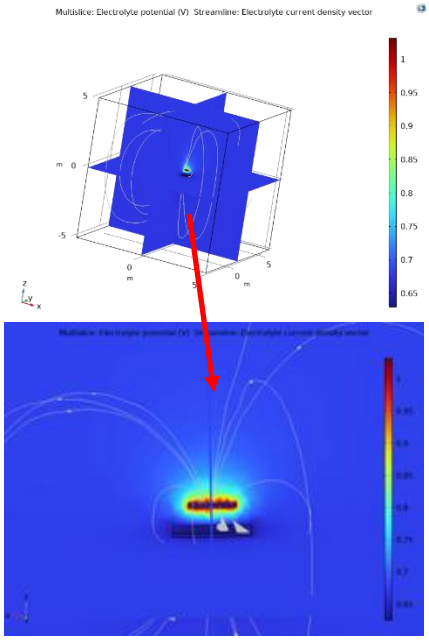


Fig. 6 *Showing 3D representation of electrolyte potential*

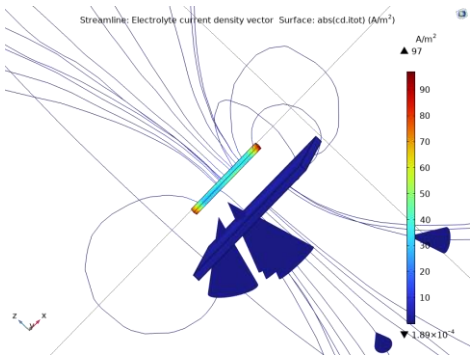


Fig. 7 *Showing 3D representation of electrolyte current density*

4. Conclusion

This paper analyzed the influence of acetic acid on steel corrosion. In the experimental study, Zn-Ni coating was used to protect the steel. The results showed that the Zn-Ni layer acted as sacrificial coatings on steel, the acetic acid, even if it is a weak acid, pickling almost the entire Zn-Ni coating. The increase in the concentration of Ni in the remaining coating implies the appearance of the dezincification phenomenon. As a result, the behavior of Zi-Ni coatings in corrosion protection depends on the Ni content.

As expected, the simulation results confirmed that the Zn alloy acts as a sacrificial anode in the case of steel subjected to acetic acid attack.

5. References

1. Makhlouf A. S. H., Herrera V., Muñoz E., Handbook of Materials Failure Analysis - With Case Studies from the Construction Industries, Chapter 6 - Corrosion and protection of the metallic structures in the petroleum industry due to corrosion and the techniques for protection, 2018, 107-122.

2. Hussein S. S., Ali N. A., Hasan B. O. International Journal of Current Engineering and Technology, Corrosion of carbon steel in flowing sulfuric acid, 6, 1, 2016, 277-283.

3. Md.Nor M.S., Salleh Z., Masdek N.R.N.M., Taib Y.M., Hyie K.M., Abu M.Z., Materials Today: Proceeding, Electrodeposition of Co-Ni-Fe thin film using hull cell, 46, 4, 2021, 1792-1798.

4. Cotolan N., Turdean G. L., Chelaru J. D., Studia UBB Chemia, Improving the corrosion resistance of mild steel by zinc-graphene oxide coatings, LXV, 3, 2020, 23-32.

5. Gavrila M., Millet J.P., Mazille H., Marchandise D, Cuntz J.M. Surface and Coatings Technology, Corrosion behaviour of zinc–nickel coatings, electrodeposited on steel, 123, 2000, 164–172.

6. Liao K., Leng J., Huang Q., Yang L., Zhou F., Zhao S., Liu X., International Journal of Electrochemical Science, The effect of acetic acid on the localized corrosion of 3Cr steel in the CO_2-saturated oilfield formation water, 15, 2020, 8622 – 8637.

7. Tran T., Brown B., NACE- International Corrosion Conference Series. Investigation of the mechanism for acetic acid corrosion of Mild Steel, 2013, 1- 11.

8 Walton J. C., Corrosion Science, Mathematical modeling of mass transport and chemical reaction in crevice and pitting corrosion, 30, No, 8/9, 1990, 915-928.

9. Narozny M., Zakowski K., Darowicki K., Corrosion Science, Method of sacrificial anode transistor-driving in cathodic protection system, 88, 2014, 275-279.

Structure, phase composition and tribological properties of iron-based composites *in situ* synthesized from powdered Fe—high-carbon ferrochrome mixtures

Yevheniia Kyryliuk, Genadii Bagliuk, Iaroslav Sytnyk, Serhiy Ivanchenko., Victor Varchenko

Frantsevich Institute for Problems in Materials Science, NASU, Kyiv, Ukraine, 03142, Krzhizhanovsky str., 3

Abstract: *The article presents the results of investigations of tribotechnical properties of powder composite materials based on the iron-high-carbon (ФХ800) ferrochrome system during dry friction with ШХ15 steel at various loads of 30, 60, and 100 N. It was found that an increase of the load from 30 to 100 N leads to an increase in the coefficient of friction from 0,45 to 0,5 (for 25% ФХ800) and from 0,40 to 0,46 (for 40% ФХ800). At the same time, the mass wear of samples made of powder materials decreases with an increase in ФХ800 content from 25 to 40 (wt. %) and with growth of the load from 30 to 100 N, respectively, from 3,5 – 8,0 to 0,75 – 1,6 mg/km., which provides wear resistance improvement (km/mm) by 2,8 – 2,2 times. X-ray phase full profile analysis using the Rietveld method established that there are 2 phases: metallic α-Fe (79,68%) and carbide Me_7C_3 (20,32%) in the composite Fe – 25%ФХ800 and 3 phases: α-Fe (69,5%), γ-Fe (3,96%) and carbide Me_7C_3 (26,57%) in the Fe – 40% ФХ800 composite. Topographic studies of 2D profiles of worn surfaces of composites after friction under different loads were conducted. The results of optical profilometry show that the main mechanism of destruction of the powder composite surface during dry friction with ШХ15 steel is adhesive wear (seizing) of the contacting surfaces.*

KEYWORDS: *COMPOSITE MATERIALS, WEAR RESISTANCE, CARBIDE STEEL, FE-CR-C MATERIALS, TRIBOTECHNICAL PROPERTIES. ФХ800 CONTENT FROM 25 TO 40 (WT. %)*

1. Introduction

In recent years, a number of researchers have shown increasing interest in metal matrix composites based on iron due to the unique combination of their basic mechanical properties and high wear resistance [1-11]. Most of the modern alloys that are used in industry as wear-resistant contain a significant amount of expensive elements, such as tungsten, cobalt, nickel, molybdenum, vanadium, etc. In a significant part of the known wear-resistant composites titanium carbide is used as a hardening solid phase, the introduction of which into the composition of the material leads to increase of the hardness and wear resistance of the latter [1-5].

At the same time, of considerable interest as materials obtained from more affordable and cheaper components, are also the iron-based composites reinforced with chromium carbides, produced using powder metallurgy methods from mixtures of chromium carbide and steel powders of the appropriate composition [12-15].

As the authors [15] have shown, at the sintering of consolidated chromium carbide — steel powdered mixtures the interaction of the initial chromium carbide Cr_3C_2 powder with matrix steel complex iron–chromium carbide of $(Cr, Fe)_xC_y$ type forms and with increasing temperature it undergoes a number of phase transformations.

Unlike the technological approaches presented in [12-15], the authors of [16, 17] proposed using cheap and non-deficient high-carbon ferrochrome instead of chromium carbide Cr_3C_2 powder for manufacturing of chromium carbides reinforced iron-based composites. Molten ferrochrome of industrial production, in a lump or granulated state, due to its high brittleness, is quite easily crushed into a powder suitable to produce wear-resistant and corrosion-resistant powder materials and products made of them. The operational and mechanical properties of wear-resistant alloys depend on many factors, primarily on the characteristics of the carbide phase. It is shown, that in the process of liquid-phase sintering the interaction of high-carbon ferrochrome with iron powder take place with transformation of iron into chrome ferritic-austenitic steel.

The aim of this article is to study the peculiarities of the structure and phase composition of composites sintered from a mixture of iron and ferrochrome powders with different component composition and their tribotechnical characteristics.

1. Materials and research methods

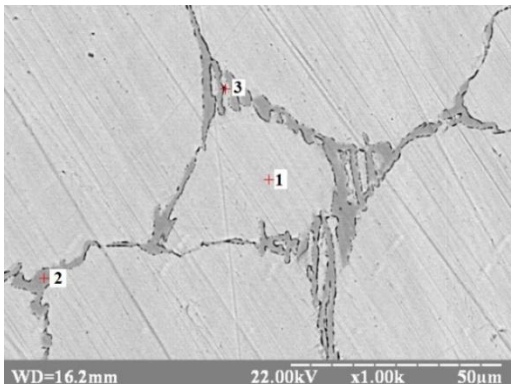
The initial materials were powders of iron ПЖР3.260.28 and high-carbon ferrochrome ФХ800 (wt. %): 72,2 Cr, 18,8 Fe, 8,4 C, 0,6 O – fractions –200+100 μm. Powder mixtures were prepared by wet grinding in a ball mill according to the modes shown in [10]. The content of ФХ800 was varied from 25 to 40 (wt. %). The samples were consolidated in a closed mold at a pressure of 800 MPa. Sintering was carried out in a vacuum electric furnace at 1100 – 1300 °C under a vacuum of at least 10^{-2} Pa. The mechanical properties of the samples were determined according to standard methods used in testing powder materials and hard alloys [18, 19]. The microstructure of the materials was studied using a REM-106I electron microscope. Filming was carried out from cuts in copper monochromatic radiation; X-ray phase analysis – on a DRON-3 diffractometer. The search for correspondence of diffraction lines to known compounds in Fe-Cr-C systems was carried out using the PDF-2 database. Refinement of the structures was carried out by the Rietveld method using the PowderCellBase suite of programs. The wear resistance of the materials was studied according to the shaft (counter-body) – plane (sample) scheme by dry friction on ШХ15 steel at room temperature (+ 30 °C). Test conditions: sliding speed v = 1 m/s; load, p = 30, 60, 100 N; friction path – 1 km. Mass and linear wear, wear resistance, quantitative and qualitative parameters of the surface relief were determined by the method of optical profilometry using a non-contact interference 3D profilograph Micron-Alpha by the company "Micron-system".

3. The results of the experiments and their discussion

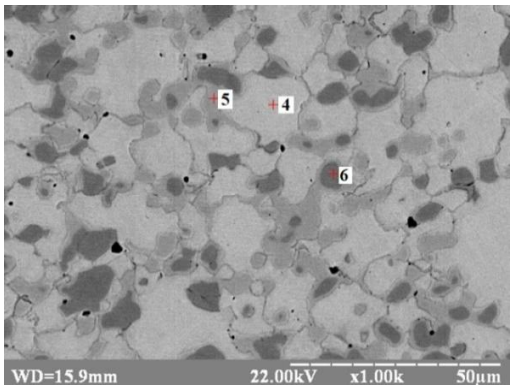
Full-profile analysis of Fe – 25% ФХ800 and Fe – 40% ФХ800 carbides was carried out according to the Rietveld method. X-ray phase analysis made it possible to determine that there are two phases in the Fe–25% ФХ800 composite, metallic α-Fe – 79,68% and carbide Me_7C_3 – 20,32%. The results of indexing the X-ray pattern indicate that the metal phase of carbide steel Fe – 25% ФХ800 is a BCC phase based on α-Fe with a period of a = 0,2875 nm (that is, slightly increased compared to pure iron due to the dissolution of chromium). Therefore, the results of the X-ray phase analysis allow us to conclude that when the amount of high-carbon ferrochrome changes from 25% to 40%, the phase composition of the composite changes, namely, a small amount of austenitic γ-Fe is formed in the amount of 3,96% in the Fe – 40% ФХ800 composite. The content and lattice parameters of the carbide phase of the Me_7C_3 type remain practically unchanged in both composites.

Microstructures of sintered carbide steels with 25 and 40 (wt. %) ФХ800 are shown in Fig. 1. It can be observed that the microstructure thereof is heterogeneous and consists of metal and carbide phases and a certain number of pores. As the ferrochrome content increases, it changes: from matrix-framework at 25 (wt. %) ФХ800 (Fig. 1, a) to matrix-filled at 40 (wt. %) ФХ800 (Fig. 1, b). X-ray microspectral analysis of samples with 25 and 40 (wt. %) ФХ800 revealed that the metal phase is similar in composition to chromium steel, the content of the main elements is shown in (Fig. 1). The microhardness of the matrix for materials of both compositions is 2,15 – 2,3 GPa. According to the results of X-ray

phase and micro-X-ray spectral analyses, the carbide phase of the composites is a complex iron-chromium carbide of the Me_7C_3 type. As can be seen from the above microstructure (Fig. 1, b), three phases are clearly visible in the 60% Fe – 40% ΦX800 composite: light gray, gray, and dark gray.



a



b

Spectrum №	Content of the main elements, (wt. %)	
	Fe	Cr
1	80.7	17.8
2	32.3	67.6
3	53.1	45.4
4	79,4	19.23
5	40,83	57.23
6	28,91	70.7

Fig. 1. *Microstructure of carbide steels sintered at 1250 °C for 30 min (SEM): a – 25, b – 40 (wt. %) ΦX800*

X-ray microspectral analysis with large measurement statistics on different carbides indicates that the ratio of iron and chromium atoms in them is different. In the volume of one carbide, the amount of chromium increases and reaches a maximum in the center. Taking into account the fact that the formation of the phase composition occurs by a diffusion mechanism due to the movement of chromium atoms from the carbide into the iron matrix and iron atoms from the matrix into the carbide, it is possible to state that the contrast in (Fig. 1, b) is due to the different ratio of iron and chromium atoms in lattices of the same type of carbide, accordingly, it affects the different microhardness of the carbide phases. The microhardness of the carbide phase (Fig. 1, b, № 5) is 6,4 GPa, (Fig. 1, b, № 6) – 11,4 GPa. The microhardness of the carbide phase in the Fe – 25% ΦX800 composite is 12,2 GPa.

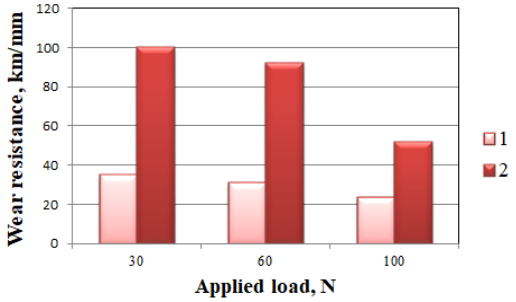
The table 1 shows the density, volume shrinkage, and basic physical and mechanical properties of composites with 25 and 40 (wt. %) ΦX800 sintered at optimal temperatures. Experiments have shown that with an increase in the amount of ΦX800 from 25 to 40 (wt. %), the hardness and the bending strength limit increase symbatically. The increase in the hardness of materials occurs due to an increase in the amount of the solid component and secondary carbides, which were formed because of the intensive interaction of high-carbon ferrochrome with the iron base during sintering.

Table 1

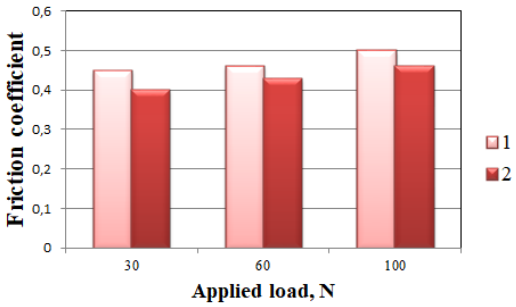
The influence of the content of high-carbon ferrochrome on the density, volume shrinkage and physical and mechanical properties of carbide steels

Samples composition (wt. %)	T_{sint},°C	γ, g/cm³	ΔV/V, %	HRA	σ_b,МПа	K_{Ic}, MPa*m$^{1/2}$
75Fe – 25FKh800	1250	6,94	24,5	66	1100	24,9
60Fe – 40FKh800	1250	7,3	32	76	1665	19,4

Systematic studies of the tribotechnical properties of powder composite materials based on the iron-high-carbon (ΦX800) ferrochrome system during dry friction with ШХ15 steel at a sliding speed of 1 m/s and loads of 30, 60, and 100 N were conducted. The dependence of the wear resistance effect (Fig. 2, a) and the coefficient of friction (Fig. 2, b), composites of different composition on the change in contact pressure was studied. It was established that an increase in the ΦX800 content from 25 to 40 (wt. %) and the load from 30 to 100 N leads to an increase in the coefficient of friction with ШХ15 steel (HRC 55 – 60) from 0,45 to 0,5 (25% ΦX800) and from 0,40 to 0,46 (40% ΦX800).



a



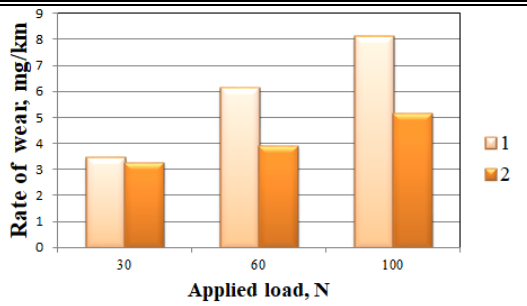
b

Fig. 2. *Dependence of wear resistance (a) and friction coefficient (b) of composites of the Fe – ΦX800 system on the load force: 1 – 75% Fe – 25% ΦX800; 2 – 60% Fe – 40% ΦX800*

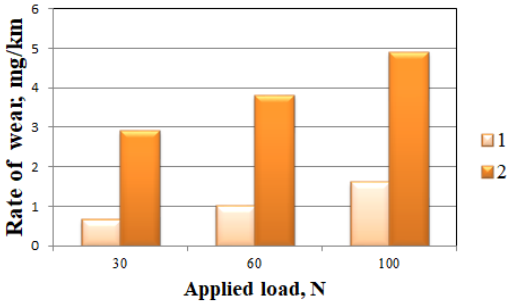
At the same time, the mass wear of the samples (Fig. 3) made of powder materials decreases with an increase in the ΦX800 content from 25 to 40 (wt. %) and growth of the load from 30 to 100 N, respectively, from 3,5-8,0 to 0,75 – 1,6 mg/km, which provides an increase in wear resistance (km/mm) by 2,8 – 2,2 times.

Such a significant increase in wear resistance is due to the higher content of the carbide component in the material with 40 (wt. %) ΦX800 and, accordingly, its high hardness. It is important to note that the mass wear of the counter-body made of ШХ15 steel for the materials of both compositions does not change significantly and ranges between 3,5 – 4,5 mg/km.

Topographic studies of worn surfaces of carbide steels Fe – (25, 40)% ΦX800 during dry friction on a counter-body made of ШХ15 steel under different loads were carried out (Fig. 4).



a

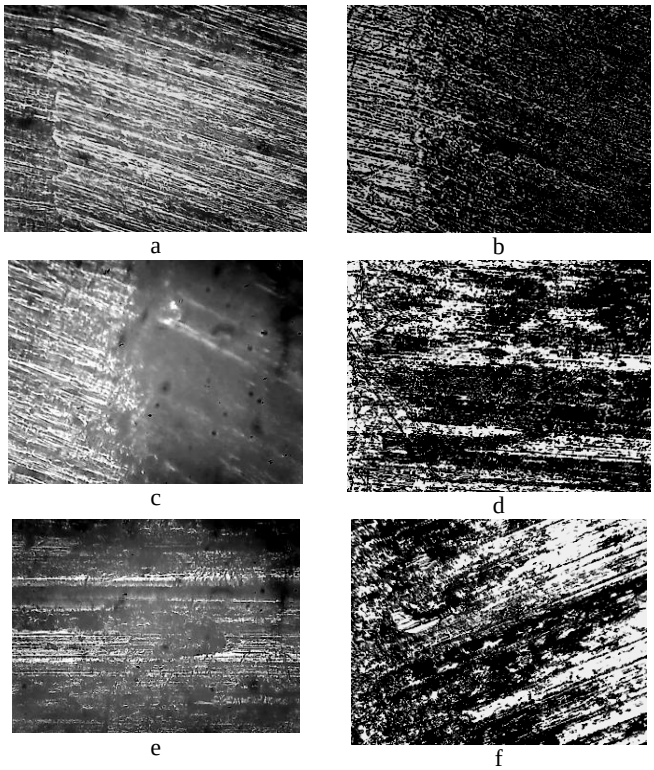


b

Fig. 3. *Dependence of the mass wear of sample (1) and counter-body (2) on the load force of Fe – 25% ΦX800 (a) and Fe – 40% ΦX800 (b) composites*

According to the research results, it is seen that an increase in the load from 30 to 100 N leads to critical wear of the materials of both compositions.

This is especially noticeable from the given 2D profilometry of the surfaces of carbide steel with 25% ΦX800 after the friction test at loads of 60 and 100 N (Fig. 4, c, e), significant grain tear-out and the formation of deep cavities are clearly visible after the tribotechnical researches.



a b c d e f

Fig. 4. *Image of 2D profiles of topography of wear surfaces of Fe – 25% ΦX800 (a, c, e) and Fe – 40% ΦX800 (b, d, f) material samples under different loads: 30 N (a, b); 60 N (c, d); 100 N (e,f)*

However, profilometric studies of the surface of this composite after friction at a lower load (30 N) showed uniform wear of carbide steel, without noticeable deep traces of grain tear-out, which is clearly visible from the 2D profile of the sample surface (Fig. 4, a).

Images of surface topographies of 2D and 3D profiles of 60% Fe – 40% ΦX800 carbide steel after tribotechnical tests, differ from the previous sample in more uniform wear over the entire plane of the sample under different loads. (Fig. 4, b)

As we can see from Fig. 4, d, local sharp protrusions, the number of which is much smaller compared to the 75% Fe – 25% ΦX800 composite, and no significant cracking of the grains was also found after the tribotechnical tests. With an increased load of up to 100 N, deep traces of wear and tear-out of the grain are clearly visible in the given photos of surface profilometry, which indicates significant wear of the composite under the given load (Fig. 4, f).

Based on the results of the research, we can conclude that increase in the amount of high-carbon ferrochrome to 40% leads to an increase in the uniformity of wear of the composite surface during dry friction on a counter-body made of ШХ15 steel at a load of 30 and 60 N. This dependence is confirmed by the results of optical profilometry for carbide steel 60% Fe – 40% ΦX800, it was also established that the main mechanism of destruction of the surface of the powder composite during dry friction with steel ШХ15 is adhesive wear (seizing) of the contacting surfaces.

Conclusions

1. Systematic studies of the tribotechnical properties of powder composite materials based on the iron-high-carbon (ΦX800) ferrochrome system during dry friction with ШХ15 steel at a sliding speed of 1 m/s and loads of 30, 60, and 100 N were conducted. It was established that an increase of the load from 30 to 100 N leads to an increase in the coefficient of friction with steel ШХ15 from 0,45 to 0,5 (for 25% ΦX800) and from 0,40 to 0,46 (for 40% ΦX800). At the same time, the mass wear of samples made of powder materials decreases with an increase in the ΦX800 content from 25 to 40 (wt. %) and growth of the load from 30 to 100 N, respectively, from 3,5 – 8,0 to 0,75 – 1,6 mg/km, which provides wear resistance improvement (km/mm) by 2,8 – 2,2 times.

2. X-ray phase full-profile analysis using the Rietveld method, established that there are 2 phases: metallic α-Fe (79,68%) and carbide Me_7C_3 (20,32%) in the Fe – 25% ΦX800 composite and 3 phases: α-Fe (69,5%), γ-Fe (3,96%) and carbide Me_7C_3 (26,57%) in the Fe – 40% ΦX800 composite. Thus, it was confirmed that in both composites the main BCC phase is based on iron with a lattice period of a = 0,2875–0,2879 nm, which is slightly larger compared to the period for pure iron due to the dissolution of chromium.

3. Topographic studies of 2D profiles of worn surfaces of composites under friction and loads of 30, 60, and 100 N clearly record the breaking out of particles and the formation of a significant number of deep cavities, which is particularly noticeable in the composite with 25 (wt. %) ΦX800 at high loads. Unlike it, profilometric studies of the surface of the composite with 40 (wt. %) ΦX800 did not reveal a significant amount of destruction, tearing out and crushing of grains. The main parameters of the texture of worn surfaces indicate that increase in the amount of ferrochrome to 40 (wt. %) ensures uniform wear of the composite surface. The results of optical profilometry confirm that the main mechanism of destruction of the surface of the powder composite during dry friction with ШХ15 steel is adhesive wear (seizing) of the contacting surfaces. The developed powder composites are recommended for the manufacture of wear-resistant structural parts, linings of brake and friction devices.

References

1. Baglyuk G.A., Poznyak L. A. Powder metallurgy wear-resistant materials based on iron. Part 1. Materials prepared by sintering and infiltration. *Powder Metall. Met. Ceram.*, **40**, No. 1–2, 34–39 (2001).

2. Parashivamurthy K.I., Kumar R.K., Seetharamu S., Chandrasekharaiah M.N. Review on TiC reinforced steel composites. *Journal of Materials Science*, **36**, 4519–4530 (2001).

3. Razavi M., Yaghmaee M. S., Rahimipour M. R. et al. The effect of production method on properties of Fe–TiC composite. *International Journal of Mineral Processing.* **94**, 97–100 (2010).

4. Baglyuk G.A., Martyukhin I.D., Pavligo, T.M. et al. Structural features of hot-forged carbide steel (high-speed steel–titanium carbide). *Powder Metall Met Ceram.* **48,** 34–37 (2009).

5. Brown, I.W.M., Owers, W.R. Fabrication, microstructure and properties of Fe–TiC ceramic–metal composites. *Current Applied Physics*, **4**, 4, 171–174. (2004).

6. Deshpande M.V., Deshpande M.V., Saxena J.P., Basu S., Sebardt W. Tougher cemented carbide material with iron-rich binder for steel turning and form-grooving. *International Journal of Refractory Metals & Hard Materials,* **15**, 157-162 (1997).

7. Straumal, B.B. Konyashin, I. WC-Based Cemented Carbides with High Entropy Alloyed Binders: A Review. *Metals,* **13**, 171-188, (2023).

8. Zhong L.S., Xu Y.H., Hojamberdiev M., Wang J.B., Wang J. *In situ* fabrication of carbide particulates-reinforced iron matrix composites. *Materials & Design.* **32**, 3790-3795 (2011).

9. Pittari J. J., Murdoch H. A., Kilczewski S. M., Hornbuckle B. C., Swab J. J., Darling K. A., Wright J. C. Sintering of tungsten carbide cermets with an iron-based ternary alloy binder: Processing and thermodynamic considerations. *International Journal of Refractory Metals & Hard Materials,* **76,** 1–11 (2018).

10. Martins I.M., Oliveira M., Carvalhinhos H. Wear Resistant High Speed Steel Matrix Composites. *Advances in Powder Metallurgy & Particulate Materials.* - Princeton, N.J. **l** (6), 213÷218 (1992).

11. Schubert W.D., Fugger M., Wittmann B., Useldinger R. Aspects of sintering of cemented carbides with Fe-based binders. *International Journal of Refractory Metals and Hard Materials*. 49, 110-123 (2015).

12. Maslyuk V. A., Napara-Volgina S. G. Wear-resistant and corrosion-resistant carbide-steel-type materials having different matrices. *Powder Metall. Met. Ceram.*, **38**, No. 9–10, 521–525 (1999).

13. Maslyuk V. A., Napara-Volgina S. G. Kud' V. K. Sintered composites based on stainless steel. *Powder Metall. Met. Ceram.*, **39**, No. 11–12, 549–553 (2000).

14. Maslyuk, V.A. Tungsten-Free Hardmetals and Carbide Steels with Chromium Carbides. *Powder Metall Met Ceram* **53**, 162–169 (2014).

15. Yakovenko, R.V., Maslyuk, V.A., Mamonova, A.A. et al. Interaction of Chromium Carbide with a Kh13M2 Steel Matrix. *Powder Metall. Met Ceram.* **52,** 644–650 (2014).

16. Kyryliuk E., Bagliuk G., Maslyuk V., Bondar A. Structure and properties of chromium carbide reinforced steel matrix composites produced from powder iron-ferrochrome mixtures. *Machines. Technologies. Materials.* **VII**, No. 1, 3-5 (2021).

17. Kyryliuk Ye., Bagliuk G., Mamonova A., Maslyuk V. Synthesis of Fe-Based Alloy Reinforced with Chromium Carbide Via Sintering of Iron-Ferrochrome Powder Mixture. *Powder Metallurgy Progress*. **21** (1), 18-26 (2021).

18. ISO 4498-1-:1990. Sintered metal materials, excluding hardmetals – determination of apparent hardness. Part 1: Materials of essentially uniform section hardness. Ed. 1990-08-2. ISO, 1990.

19. ISO 3327:2009. Hardmetals – Determination of transverse rupture strength. Ed. 2009-05-15. ISO, 2009.

Production method role for the composite powders quality

Krasimira Toncheva[1], Zoya Savova,[2] Luben Lakov[1]
[1]Bulgarian Academy of Science, Institute of Metal Science, Equipment and Technologies with Hydro- and Aerodynamics Centre, "Acad. A. Balevski", 67, "Shipchenski Prohod" Blvd, 1574 Sofia, Bulgaria,
[2] Private investor
krasiton4@abv.bg

***SUMMARY**:Self-propagating high-temperature synthesis (SHS), refers to a technology for the production of useful materials (mainly composite powders) that uses combustion processes. The solid combustion process results in the release of more heat which is needed to re-bond the elements of the system and it is this extra amount of heat that is used to self-sustain the combustion process and its development. This process is known as self-propagating high temperature synthesis.*

This paper presents the study of the magnetic properties of the products obtained by this method in comparison with other methods which use nickel-zinc ferrites. The latter are widely used in radio devices, antennas and transformer cores, as well as in high-frequency filters where the current loss is significant.

***Keywords**: Self-propagating high temperature synthesis (SHS), ferrite powders, magnetic properties*

1. Introduction

Today, there exist various production methods that involve the synthesis and processing of composite powder materials with controlled properties.

Metal and ceramic powders produced by self-propagating high-temperature synthesis with controlled microstructures, as well as parts produced using them have shown very good quality and improved properties. These better properties include higher hardness, higher yield strength and ductility of the metal ceramic materials.

As a result, these materials find application as sensors, catalysts and coating materials (surface property modifiers). Some of the well-known methods for obtaining metal ceramic materials are: laser absorption, plasma synthesis, chemical vapour deposition, mechanical alloying or high energy milling, and sol-gel synthesis. All these techniques require long processing times, expensive chemicals and special equipment.

The self-propagating high-temperature method has been adopted as a technique for the production of useful materials using the method of sintering and solid-fuel combustion. The combustion process is carried out by exothermic oxidation and reduction reactions between oxidant and fuel. In this case, the heat involved is greater than that required for the reaction and thus the system becomes self-sustaining. The exothermic reaction brings the system to a high temperature. The process is known as self-propagating high temperature synthesis (SHS).

Compared with the conventional process, the SHS method has some advantages such as high productivity, low consumption of external energy, short synthesis time, simple equipment, and high product quality.

Nickel-zinc ferrites are widely used in radio frequency antennas and transformer cores, as well as in high-quality filters due to their resistivity and low eddy current losses.

2. Experimental procedure

One of the so-called low methods for the production of $NiO.35ZnO.65Fe_2O_4$ powder materials and parts thereof is the self-propagating high temperature SHS synthesis technology. Increasing the combustion temperature leads to an increase in grain size.

Microphotographic and magnetic (XRD, TEM) studies show that at 1000°C the basic structure of spinel products is phase. The particle shape is spherical and homogeneous with a size of 0.5 μm. Compared with other methods, the results prove that Ni-Zn ferrite powders can be produced by the SHS method at 1000°C and have improved magnetic properties.

The raw materials used to obtain the magnetic composition of $NiO.35ZnO.65Fe_2O_4$ are as follows:

- Ferrite powders - iron with an average particle size of 20 μm, iron oxide with an average particle size of 0.8 μm
- Nickel oxide with an average particle size of 0.8 μm
- Zinc oxide with an average particle size of 0.5 μm

The purity of the raw materials is 99%.

First, the starting reagents were weighed according to the required stoichiometric proportion. Then they were mixed and pressed into briquettes with a thickness of 4 mm, diameter of 50 mm and length of 100 mm. The experiments were conducted in a water-cooled cylinder.

The pressed Pt/Rh thermocouples in the briquettes were used to measure the main SHS process parameters and the combustion temperature. The experimental data were registered with a recorder. Fig. 1 shows pictures of different high pressure experimental chambers. The flowmeter records the measurement of the gas components enabling the solid combustion process.



***Fig.1.** Different types of chambers with professional flowmeters*

The phase composition and degree of saturation (compaction) of the resulting products were investigated using X-ray diffraction analysis (XRD).

The magnetic properties of the obtained products were recorded using a vibrating sample magnetometer (VSM, M - 9500, USA). The size and the shapes were analyzed using transmission electron microscopy (TEM, Philips CM12 CTEM).

3.Results and discussions:

The XRD diagrams of the combustion products obtained at different temperatures are presented in Fig. 2.

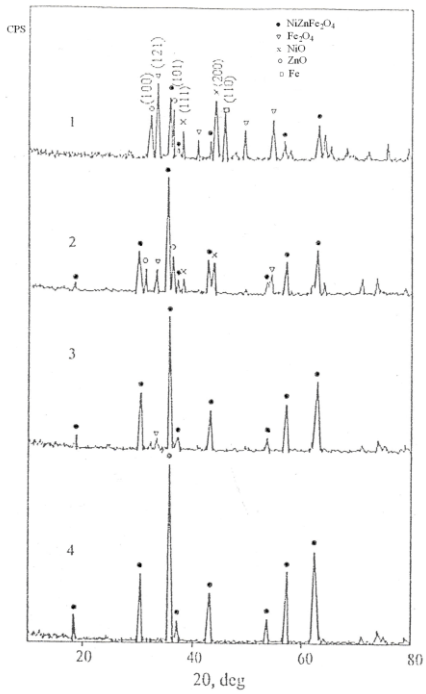
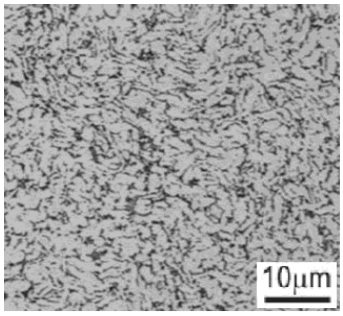
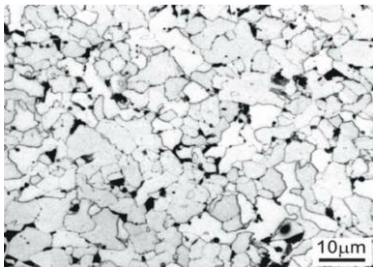


Fig. 2. *XRD results of the products obtained at different combustion temperatures*
1 - 700°C; 2 - 900°C; 3 - 1000°C; 4 - 120 °C

They show that in parallel with the increase in the combustion temperature from 700°C to 1200°C, the intensity of the diffraction peaks of NiO - nickel oxide, ZnO - zinc oxide, Fe - iron and Fe2O3 - iron oxide raw materials decreases, while the intensity of combustion products decreases with the increase in the density.



а



б

Fig. 3 *TEM micrographs of products obtained at different combustion modes.*
(a)- at 1000 °C; (b) - at 1200 °C.

At 1000°C the diffraction peaks of Fe, NiO amd ZnO disappear and the spinel peaks of ferrites can be clearly observed in the X-ray spectra of the products.

At 1200°C XRD can be indexed as spinel type phase with additional lines corresponding to every other phase. However, the diffraction peaks are quite sharp due to the grain growth of the crystallites produced at the higher combustion temperatures. Fig. 2 clearly shows the influence of the combustion temperature on the particle size for Ni - Zn ferrite powders. It is evident that increasing the combustion temperature leads to an increase in particle size.

In Fig. 3 are shown TEM micrographs of products obtained at different combustion modes.

They clearly show the spherical shape of the particles with an average size of about 0.5 μm produced at the lower temperature of 1000°C. In the next picture (1200°C) the particle size is approximately the same - 0.5 μm, but the shape is extremely crude and rough. Such a product cannot be used for sintering.

The magnetic properties of the SHS products were investigated at room temperature. The results are summarized and presented in Fig. 4 and Fig. 5.

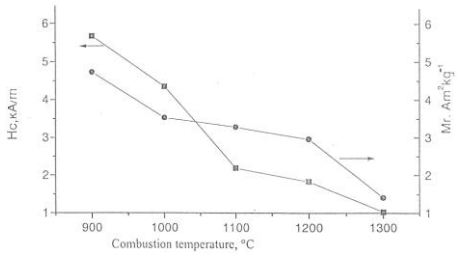


Fig 4. *Coercive force H_c and residual magnetism M_r as a function of T °C*

The saturation magnetization M_s increases due to the increase in the combustion temperature. This fact indicates an increase in particle size and a high degree of ferritization. At the same time, the residual magnetization M_r and the coercivity H_c decrease. Fig. 4 shows that when the combustion temperature is higher than 1350°C, the magnetic activity of the powder decreases and a ferrite with low magnetic parameters is obtained.

Hysteresis curves of the combustion products are obtained at different temperatures. They are presented in Fig. 5.

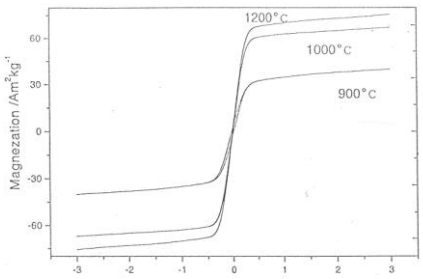


Fig. 5. *Hysteresis curves of ferrite powders obtained at different temperatures*

The M_s values are also compared with those published in the literature. The comparison shows that the saturation magnetization of SHS products and ferrite powders obtained using other methods have similar values. The conducted experiments prove the improved properties of SHS products.

SYNTHESIS METHOD	Saturation magnetization M_s
SHS	66.15
Wet chemical method	45.50
Solid reaction	48.50
Molten salt synthesis	65.00
High energy ball mill	66.00

CONCLUSIONS:

-Ferrite powder NiO,35ZnO,65Fe_2O_4 was synthesized using the SHS method;

-Increasing the combustion temperature leads to particle growth;

-XRD and TEM studies show that at 1000°C, the crust structure of the products is mainly spinel type phase;

-At 1000°C, particle size is spherical and homogeneous and equals about 0.5μm;

-Comparison with other methods proves that Ni - Zn ferrite powders can be obtained by SHS method at 1000°C.

LITERATURE:

1. Anil Kumar B.S – J. Appl. Phys. 81/1997/4788
2. Murin I.V. – Solid State Ionic 133/2003/203
3. Bowen C.R. Derby B. - Brit. Cer. Trans. 96, 1997, 25 – 28
4. Satori Takashi – Mat. Trans. Vol. 6 /2006/1181
5. Jiang J.S. –J. Mater. Sci, Lett. 18/1999/1783

Development of a composite alloy zinc-containing material and investigation of its influence on the chemical composition of BRSN5ZN5PB5 powders produced by the method of induction melting and spraying the melt with an inert gas

Aliaksandr Ilyushchanka[1, 2], Ruslan Kusin[2], Iryna Charniak[2], Aliaksei Kusin[2]
State research and production powder metallurgy association[1] – Minsk, Republic of Belarus
State Scientific Institution "O.V. Roman Powder Metallurgy Institute" [2] – Minsk, Republic of Belarus
Educational establishment "Belarus State and Agrarian Technical University" – Minsk, Republic of Belarus
E-mail: alexil@mail.belpak.by, 19081877@mail.ru, irinacharniak@tut.by, 2312444@mail.ru

***Abstract**: The process of obtaining bronze powders of grade BrSn5Zn5Pb5, obtained by the method of induction melting and spraying of the metal melt with an inert gas, has been studied. It is known that in the production of BrSn5Tsn5Pb5 powder, the main losses of zinc occur during the melting of the components. To study the possibility of reducing zinc losses in the melt, a zinc-containing composite alloying material has been developed. Its effect on the chemical composition of BrSn5Zn5Pb5 powders obtained by induction melting and spraying the melt with an inert gas has been studied.*

***KEYWORDS:** INDUCTION MELTING, ZINC LOSS, BRSN5ZN5PB5 BRONZE POWDER, COMPOSITE ALLOYING MATERIAL, TECHNOLOGY, RESEARCH, PROPERTIES*

1. Introduction

Bronze powders of the BrSn5Zn5Pb5 brand are widely used for spraying coatings by the gas-thermal methods on the working surfaces of parts operating under conditions of friction and wear. One of the main ways to obtain spherical powders for spraying is the spraying of a superheated metal melt with a gas flow [1–3]. The method of obtaining metal powders by melt spraying is technological, versatile and highly productive.

However, during induction melting, the multi component alloy BrSn5Zn5Pb5 becomes significantly depleted in zinc due to the large difference between its boiling temperatures with the melting temperature of the main component. A large number of techniques have been developed to reduce the loss of alloying components during melting and alloy casting, the main recommendations of which are as follows [4–6]: to prevent overheating of the melt [7]; use deoxidizers; use fluxes.

Zinc and its alloys based on it are very sensitive to overheating. Losses of metals from evaporation depend on the saturation vapor pressure of the liquid metal: the higher the vapor pressure, the greater their losses during the preparation of alloys [8]. At the moment when the vapor pressure of the metal becomes equal to the external pressure, the metal begins to boil, i.e. evaporation occurs not only from the surface, but also throughout the volume.

It`s known that in the production of BrSn5Zn5Pb5 powder, when lump zinc is introduced into an overheated melt of copper, tin and lead, its surface actively melts and begins to evaporate, while the central part of the introduced piece is still in the solid phase. When a piece of zinc is completely melted, it takes time for it to be evenly distributed over the volume of the crucible, during which the zinc also continues to actively burn out. Then, the melt superheated to 1300 °C enters the metal receiver of the spraying unit, from where it flows to the spraying unit, where the melt jet is directly sprayed onto discrete particles and crystallized. During the residence time of the melt in the metal receiver, zinc burnout also occurs, however, this time can be reduced either by reducing the amount of melt being poured (decreasing productivity) or by increasing the outlet of the metal receiver (decreasing the efficiency of the spraying process), which is impractical. Thus, the main task is to reduce the time for melting and distribution over the volume of the crucible introduced into the zinc alloy.

The purpose of the work is to reduce the loss of zinc in the process of obtaining bronze powder BrSn5Zn5Pb5 by induction melting and spraying the metal melt with a gas stream.

2. Experimental results and discussion

The production of experimental samples of sprayed bronze powders of the brand BrSn5Zn5Pb5 included the following main operations [9 – 12]:

– *weighing of the initial components*. The following components were used as initial components: copper scrap without soldering and soldering, zinc lamellar anodes, tin grade O1, lead sheets grade C1 in the state of delivery;

– *loading components into the induction melting furnace and heating.* The melt was superheated with respect to the main component by 117–317°C: the melt temperature was 1300°C;

– *melt jet spraying*. Within 30 seconds from the moment of readiness, the melt entered the metal receiver. From the metal receiver, the melt flowed freely through the nozzle with a hole of a certain diameter in the form of a vertically falling jet into the spray zone, and dispersed into fine droplets by a stream of inert gas. Atomized drops of the melt due to the forces of gravity moved into the water, where they crystallized and cooled; figure 1 shows the installation of spraying molten metal;

– *extracting the powder from the plant and it`s drying.* The atomized powder was removed from the tray and dried at a temperature of 110-120°C;

– *sieving of the powder*. The dried powder was dispersed into fractions and its chemical composition was studied.



***Fig. 1** Installation for spraying powders with an inert gas.*

To solve the problem, samples of bronze powder BrSn5Zn5Pb5 were made by the method of induction melting by spraying the metal melt with an inert gas, a zinc-containing composite alloying material (CAM) was developed. To study the reduction of zinc losses, CAM was introduced into the bronze melt in three ways.

In the first method, a layered CAM was made for research, consisting of rolled zinc and lead plates. To increase the uniformity of the zinc melting process, it was decided to coil the plate together with a plate of another alloying component – lead, since its melting point is closer to the melting point of zinc than the melting point of the alloying component - tin. The melting and boiling points of the components of the BrSn5Zn5Pb5 alloy are given in Table 1 [6].

Table 1 *- Melting and boiling points of the components of the alloy BrSn5Zn5Pb5 [6]*

Metal	Melting t, °C	Boiling t, °C
Copper (Cu)	1083.0	2570.0
Tin (Sn)	232.0	2270.0
Lead (Pb)	327.0	1740.0
Zinc (Zn)	419.5	907.0

For ease of administration and dosing, CAM was made in the form of small elements, weighing 50 g (zinc - 25 g, lead - 25 g). The plates were folded into a spiral. The appearance of zinc, lead and CAM plates is shown in Figure 2.



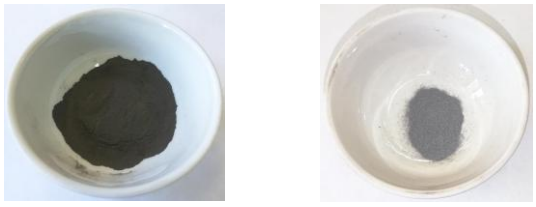
a) b) c)

Fig. 2. *Plates of zinc (a), lead (b) for the manufacture of a layered composite alloying material and CAM (c).*

The resulting BrSn5Zn5Pb5 powder was examined for zinc content. The chemical composition of the powder was determined using an ED 2000 X-ray fluorescence spectrometer (England). The zinc content in the resulting powder was 2.0%, i.e. 61.2% of the initially introduced zinc burned out, which differs slightly from the classical technology for introducing lump zinc (2.58 - 2.6%, i.e. 61.19 - 61.49 % [12, 13]).

As a result of the analysis of the obtained results, it was decided to introduce zinc in the second way, not in the form of a plate, but in the form of discrete particles of zinc powder, mixed and pressed with lead particles, in the form of a disk. The CAM obtained in this way had advantages over the layered one. When it was introduced into the melt, lead was first melted, which still contributed to the uniform rapid melting of zinc.

Dispersion-strengthened CAM was made in the form of discs 30 mm in diameter and 30 g in weight (15 g of zinc and 15 g of lead). The appearance of the materials used to obtain CAM is shown in Figure 3.



a) b)

Fig. 3. *Lead powders (a) and zinc (b) for the manufacture of dispersion-strengthened Zn-Pb CAM.*

The appearance of the dispersion-strengthened Zn-Pb CAM is shown in Figure 4.



Fig. 4. *Appearance of dispersion-strengthened Zn-Pb CAM.*

According to the technology described above, an experimental sample of BrSn5Zn5Pb5 powder was fabricated [9–12]. The only difference was that instead of the layered CAM, the preheated copper-tin alloy was introduced with the dispersion-strengthened Zn-Pb CAM. The zinc content in the resulting powder was 2.79%, i.e. 45.4% of the initially introduced zinc burned out, which already gives a significant reduction in the amount of burnt zinc compared to the classical technology of introducing zinc into the alloy (2.58 – 2.6 %, т.е. 61.19 – 61.49 % [12, 13]).

To further reduce the zinc loss during melting of the BrSn5Zn5Pb5 alloy, by the third method, it was decided to increase the melting temperature of zinc, i.e. to introduce it into the melt not in its pure form, but in the form of a more refractory compound. As a more refractory zinc compound, brass L63 was chosen, containing 62–65% copper, no more than 1% impurities, the rest being zinc [5, 8, 14, 15]. The melting point of zinc is 419.5 °C, and the melting point of L63 is 906 °C, i.e. When brass is heated in a melt to 906 °C, zinc doesn't evaporate.

As in the previous case, it was decided to introduce brass (zinc) in the form of discrete particles. However, since the zinc content of brass is 34-37%, the volume of the brass part is much larger than the volume of the lead particles. In this regard, we received CAM based on 3 elements: L63, Pb and Sn.

Brass L63 was used in the form of a wire 2 mm in diameter, which was cut into particles up to 2 mm long. The CAM samples were made in the form of disks with a diameter of 30 mm and a weight of 30 g. The appearance of the starting materials is shown in Figure 5, the prepared mixture - in Figure 6 and the appearance of the sample of dispersion-strengthened CAM L63-Pb-Sn - in Figure 7.



a) b) c)

Fig.5. *Starting materials for the manufacture of dispersion-strengthened CAM L63-Pb-Sn: particles of brass L63 (a); lead powder (b); tin powder (c).*



Fig. 6. *Charge for the manufacture of dispersion-strengthened CAM L63-Pb-Sn.*



Fig. 7. *Appearance of dispersion-strengthened composite alloying material from L63-Pb-Sn charge*

In the case when dispersion-strengthened CAM L63-Pb-Sn was introduced into the copper melt, zinc did not burn out when heated to a temperature of 419.5 °C, but only when the melting temperature of brass reached 906 °C [6, 8, 14, 15], i.e. The burn-out time of zinc in the induction melting process has been greatly reduced. The study of the chemical composition of the resulting BrSn5Zn5Pb5 powder showed that the zinc content was 4.67%, i.e. 7% of the initially introduced zinc burned out, and the loss of zinc during induction melting and subsequent spraying of the melt with a gas flow is reduced by more than eight times compared to traditional technology (2.58 - 2.6%, i.e. 61.19 - 61.49 % [12, 13]).

As a result, the influence of the method of introducing zinc into the melt on the chemical composition of the resulting sprayed powders was evaluated. The results of the chemical composition of the feedstock and experimental samples of BrSn5Zn5Pb5 bronze powders studies, taking into account the developed CAM, designed to reduce zinc losses during melting, are shown in Table 2.

Table2. *Chemical composition of the feedstock and experimental samples of powders BrSn5Zn5Pb5*

Chemical element	The content of chemical elements in the feedstock,%	The content of chemical elements in the equivalent amount of experimental samples of powders, %			The chemical composition of the alloy BrSn5Zn5Pb5 according to GOST 613-79, %
		Layered CAM	Dispersed CAM Zn-Pb	Dispersed CAM L63-Pb-Sn	
Copper (Cu)	84.0	86.7	86.0	84.3	80.7–88.0
Lead (Pb)	5.0	5.2	5.1	5.0	4.0–6.0
Tin (Sn)	5.0	5.2	5.1	5.0	4.0–6.0
Zinc (Zn)	5.0	2.0	2.8	4.7	4.0–6.0
Rest.	1.0	1.0	1.0	1.0	Not more 1.3

As can be seen from the data obtained, the method of introducing zinc into the BrSn5Zn5Pb5 alloy, i.e. the type of composite alloying element used, under other identical process conditions, significantly affects the chemical composition of the resulting powders.

As a result of the research, it was found that the most effective is a composite zinc-containing composite alloying material, which is a mechanical pressed charge of brass L63, tin and lead in a mass ratio: L63 - 57.5%, Sn - 21.3% and Pb - 21.3%.

3. Conclusion

The process of obtaining bronze powders of the brand BrO5Ts5S5 by the method of induction melting and spraying of the metal melt with an inert gas has been studied. A zinc-containing composite alloying material has been developed. The influence of the method of introducing zinc-containing CLM into the metal melt during induction melting by spraying bronze powder BrSn5Zn5Pb5 is estimated.

It has been established that the most effective CAM for reducing zinc losses in the process of melting the alloy when obtaining bronze powders BrSn5Zn5Pb5 is zinc-containing CLM, which is a dispersion-hardened charge of brass L63, tin and lead in a mass ratio: L63 - 57.5%, Sn - 21 .3% and Pb - 21.3%.

The study of the chemical composition of the resulting BrSn5Zn5Pb5 powder showed that the zinc content was 4.67%, i.e. 7% of the initially introduced zinc burned out, and the loss of zinc during induction melting and subsequent atomization of the melt with a gas flow was reduced by more than eight times compared to traditional technology (2.58 - 2.6%, i.e. 61.19 - 61.49 % [12, 13]).

4. Reference

1. Kiparisov, S. Powder metallurgy, Moscow, Metallurgy, 1980, 496 p. (S. Kiparisov, G. Libenson) (in Russia).
2. Silaev, A. Dispersion of liquid metals and alloys, Moscow, Metallurgy, 1983, 144 p. (A. Silaev, B. Fishman) (in Russia).
3. Libenson, G. Processes of powder metallurgy, Moscow, NISIS, 2001, vol. 2, pp. 65-105. (G. Libenson, V. Lopatin, G. Gamarnitsky).
4. Urvachev, V. Jewelry and artistic investment casting of copper alloys, Chelyabinsk, Metallurgy, 1991, 166 p. (V. Urvachev, V. Kocheikov, N. Gorina).
5. Akulich, N. Processes and production of ferrous and non-ferrous metals and their alloys, Gomel, 2008. (N. Akulich).
6. Chursin, V. Melting of copper alloys, Physico-chemical and technical foundations, Moscow, Metallurgy, 1982, 152 p. (V. Chursin).
7. Brockmeier, K. Induction melting furnaces, trans. with him. ed. Shevtsova M.E., Stolova M.Ya., Moscow, Energy, 1972, 304 p. (K. Brockmeier).
8. Aliev, D. Oxidation kinetics and anodic behavior of zinc–aluminum alloys doped with alkaline earth metals, abstract of diss. cand. tech. Sciences: 02.00.04, Dushanbe, 2010. (D. Aliev).
9. Ilyushchanka A. Small-sized installation and nozzle with the design of the Laval nozzle for obtaining atomized powders based on copper, Powder metallurgy, Minsk, Belarusian science, Vol. 34, Year 2011, pp. 37-42. (A. Ilyushchanka, R. Kusin, I. Charniak, A. Kusin, D. Zhehzdryn, E. Manoilo, V. Kaptsevich).
10. Ilyushchanka, A. Sprayed bronze and aluminum powders for restoring worn-out surfaces using gas-flame spraying, Machines. technologies. Materals, Sofia, Bulgaria, Year XII, 2018, ISSUE 12, P. 517-520. (A. Ilyushchanka, R. Kusin, I. Charniak, A. Kusin, Y. Manoila, V. Semenov).
11. Ilyushchanka A. Ph. Study of the process of obtaining powders of bronze grade BrSn5Zn5Pb5 by induction melting and atomization of the melt with a gas stream, Ilyushchanka, A.Ph., Kusin R.A., Chernyak I.N., Kusin A.R., Pylenok A.V., New materials and technologies : powder metallurgy, composite materials, protective coatings, welding, Minsk, Belarusian science, 2020. - pp. 172-174.
12. Ilyushchanka A., Charniak I., Kusin A., Yarahovich D., Kusin R., Dechko M., Marhanava V. Production of powders of copper alloy (copper 85, tin 5, lead 5, zinc 5) by spraying a melt with a gas flow, Ilyushchanka A., Charniak I., Kusin A., Yarahovich D., Kusin R., Dechko M., Marhanava V, Machines. Technologies. Materals, Sofia, Bulgaria, 2020. – Year XIV. - ISSUE 7. - P. 280-282.
13. Brockmeier, K. Induction melting furnaces. Per. with him. ed. Shevtsova M.E. and Stolov M.Ya. - Moscow, Energy, 1972. - 304 p.
14. Ten, E.B. Processing of bronze-smelting slag with the production of a metal alloy and vitreous waste, E.B. Ten, E.A. Shangin, Non-ferrous metals. No. 7. (2012). - S. 20-24.
15. Ten, E.B. Processing of bronze-smelting slags in induction furnaces, E.B. Ten, E.A. Shangin, D.V. Stadnichenko, V.N. Krasnov. Russian foundry worker. No. 10. (2013). pp. 42-45.

Structure and physical-mechanical properties of bulk and ribbon amorphous and nanocrystalline iron-based alloys

Viktor Nosenko, Maksym Nizameiev, Oleksandr Semyrga, Vitaliy Bevz, Mykola Skoryk, Vasyl Kyrylchuk, Oleksandr Kondaurov
G. V. Kurdyumov Institute for Metal Physics of the N.A.S. of Ukraine. Kyiv, Ukraine
E-mail: victorn58@ukr.net, o_semyrga@ukr.net, bevzv@ukr.net, mykolaskor@gmail.com,

Abstract: *The physic-technological basis for fabrication of bulk rods and plates of amorphous, amorphous-nanocrystalline and 100% nanocrystalline alloys at melt cooling rates from 80 to 3200 K/s with crystal sizes from 10 to 50 nm has been developed. The multiphase structure formed in the initial bulk samples, as well as in the process of nanocrystallization of amorphous ribbons, is characterized by record microhardness values of 17-22 GPa. Amorphous powders (20-100 μm) of* $Fe_{55}Ni_8Co_6Mo_4Cr_2V_1Al_2P_9C_6B_5Si_2$ *and* $Fe_{61.37}Co_{6.84}Cr_{3.78}V_{0.85}W_{0.82}Mo_{1.06}Nb_{0.85}B_{19.87}C_{1.99}Si_{2.57}$ *alloys are used to create a wear-resistant coating on structural stainless steels and low-carbon St3 by the gas-thermal "cold" method » sputtering and subsequent melting of the applied layer.The values of microhardness (Hμ) of nano-coatings significantly exceed the microhardness of all known tool steels. Examples of technology transfer and practical using of developed amorphous and nanocrystalline alloys are presented.*

KEYWORDS: *AMORPHOUS ALLOYS, NANOSTRUCTURES, THERMAL STABILITY, MICROHARDNESS, COATING*

1. Introduction

One of the priority areas of modern physics of metals is the determination of the formation mechanisms of completely disordered and partially ordered structural states. An important advantage of non-equilibrium structural states, the limit of which is amorphous, is the expansion of the spectrum of structure-dependent physical properties and the formation of their combinations, which cannot be realized in materials with partially crystalline structures. In particular, in recent decades, the interest of both scientific centers and global industrial corporations in bulk metallic glasses has grown significantly, thanks to which new areas of practical use of the unique physical properties of alloys with an amorphous and partially crystalline nanoscale structure are opening up. The main obstructions to the wider use of amorphous alloys based on iron, are some scientific and technological problems that have not been solved until now. One of which is the lack of physically based criteria for the predisposition of alloys to amorphization (PA), and the use of the most common semi-empirical criteria, which are based on the combinations of experimentally measured temperatures of the glass transition and amorphous phase crystallization and liquidus, gives ambiguous results. In addition, a significant complication on the way to the practical use of Fe-based BMGs is the unsystematic nature of the vast majority of experimental studies, as well as the limited amount of data regarding the thermal stability of amorphous phases, the physical mechanisms of their crystallization, and the effect of subsequent crystallization on physical and mechanical properties.

2. Objective and research methodologies

The main purpose of this work is to establish the influence of the chemical composition and production conditions on the structure, crystallization kinetics, and properties of rapidly hardened amorphous and nanocrystalline iron-based complex alloys for the further development of high-strength composites and wear-resistant coatings. The goal is the optimization of promising compositions according to the content of both the main alloying carbide- and boride-forming elements (Si, B, C, P) and the complex of additional elements (Ni, Cr, Co, Mo, Nb, W, V, Mn, Al) and the development of the composition of alloys that will be used as wear- and corrosion-resistant materials for application in various ways to the working surfaces of steel structures to protect them from oxidation and wear during operation in order to extend their working life.

3. Research objects and methods

The objects of research and development in this work were: technological processes of obtaining fast-hardened high-strength alloys of the Fe–(Cr,Ni,Co,Mn,Mo,V,W,Nb,Cu,Al)–(Si,B,Al) system directly from the melt P,C) with an amorphous and nanocrystalline structure with boride and carbide strengthening, thermal stability, mechanical properties and electrical resistance of ribbons, powder and volume samples (plates and rods). Research and development of methods were carried out on basic (known) and mainly on new alloys, the chemical compositions and markings of which are given in Table 1. All alloys were produced using industrial raw materials and ferroalloys (metallurgical ligatures). According to the degree of alloying, in particular metalloids, transition metals and the content of certain impurities, new alloys can be divided into 3 groups.

Table 1. *Marking and chemical composition of the investigated alloys*

No	Alloy brand	Chemical composition, at.%	Total content of metalloids, at.%
		Group 1:	
1	HB-2	$Fe_{66}Cr_{14}W_2C_2Si_1B_{15}$	18
2	HBRM-4	$Fe_{60.6}Cr_{13.8}Mn_{0.3}Mo_{1.9}Nb_2Al_{0.2}Cu_{0.5}B_{16.2}C_2Si_{2.5}$	20,7
3	HBRM-4-1	$Fe_{58.5}Cr_{14.1}Mn_{0.3}W_{1.9}Mo_3Nb_{0.9}Al_{0.1}Cu_{0.5}B_{17.1}C_2Si_{1.6}$	20,7
		Group 2:	
4	NHRP-3	$Fe_{55.47}Ni_{11.14}Cr_{4.2}Co_{2.31}Mo_{3.37}V_{0.23}B_{14.90}C_{2.13}P_{0.81}Si_{5.44}$	23,28
5	NHRP-4	$Fe_{50.0}Ni_{19.0}Cr_{6.5}Mo_{1.5}V_1B_{14.1}C_{2.5}P_{4.4}Si_1$	22
6	NHRP-6	$Fe_{55}Ni_8Cr_2Co_6Mo_4V_1Al_2B_5C_6P_9Si_2$	22
		Group 3:	
7	HB-4	$Fe_{61.37}Co_{6.84}Cr_{3.78}V_{0.85}W_{0.82}Mo_{1.06}Nb_{0.85}B_{19.87}C_{1.99}Si_{2.57}$	24,43
8	HBKNV-1	$Fe_{52,07}Co_{14,9}Cr_{2,9}W_{0,81}Nb_{2,4}V_{1.94}B_{19,69}C_{2,48}Si_{2,77}$	25
9	HBKNV-2	$Fe_{31,14}Co_{32}Cr_6W_{1,79}Nb_{4,67}B_{19,1}C_2Si_{3,3}$	24,5
10	HBKMN-1	$Fe_{50}Co_{18}Mo_4Nb_4B_{17}Si_5C_2$	24

It should be noted that the alloys of all three groups were synthesized (melted) taking into account the well-known physicochemical approach for predicting facilitated glass formation, which is based on the properties of the alloy components and the features of their interaction displayed on the state diagrams. In particular, the presence of deep eutectics on the double (Fe–B, Fe–P) and ternary (Fe–B–Si, Fe–P–C) state diagrams contribute to the formation of glasses, a significant (at least 15%) difference in the atomic diameters of the components (transition metals and metalloids), a large difference in their valency [1-2], as well as the presence in each alloy of significantly more than three components with large negative enthalpies of mixing (ΔH^{mix}).

3.1 Preparation of starting alloys from pure components and industrial raw materials

All alloys (weighing weight – 2-2.5 kg), the composition of which according to the results of X-ray fluorescence analysis are given in the Table. 1, were melted in an induction furnace in quartz crucibles in an Ar atmosphere from a mixture of chemically pure metals (≥ 99.8%), polycrystalline silicon (99.9%) and ligatures Fe_3C (pre-synthesized from armco-iron and graphite), Fe_2B (synthesized from armco-iron and ferro-boron FB-20) and ferrophosphorus FP-16 (Fe – 16 wt.% P).

3.2 Production of rapidly quenched ribbons by the PFC method

From these ingots, ribbon samples ~22–35 μm thick and 5–20 mm wide were produced by PFC method in air onto a single Cu–Cr wheel of diameter 600 mm at tangential velocity of ~40 m s^{-1}. The temperature of the melts was monitored by an optical pyrometer and during ejection was 1623–1653 K. The molten metal was ejected by argon gas at an overpressure of 20 kPa through the orifice in the quartz nozzle positioned at ~ 0.2 mm from wheel surface.

Productivity of obtaining quick-hardened ribbon – 0.5–2.5 kg/cycle; the rate of descent of the formed ribbon (the range of adjustment of the working linear speed of rotation of the tempering disc) is 10–40 m/s; tape width – 3–25 mm; typical cooling rate of the melt is $(5–10)\cdot10^5$ K/s.

Plastic ribbons with a thickness of 18–22 μm, which could withstand a 180° bend along the zero radius, were also obtained from HB-4, NNPR-4, and NNPR-6 alloys when quenched to 2.5 kg of melt.

The elemental composition of the alloys was confirmed within ± 0.2 at.% by the X-ray fluorescence analysis. The carbon composition was further specified by chemical spectral analysis when burning up to 3 g of dispersed powder.

3.3 Production of bulk amorphous and nanocrystalline samples (plates, rods) of new complex alloyed alloys

Bulk samples were obtained by pouring or ejecting of the melt under an excess pressure of 50 kPa into massive copper molds 120 mm high with a rectangular constant (5×10 mm^2) or wedge-shaped ((0.5–2.5)×10 mm^2) section. In Fig. 1 demonstrates just such a method of obtaining plates (cross section of 3×10 and 5×10 mm^2).



a b c

Fig. 1. Equipment for HF melting and production of bulk amorphized ingots (plates or rods) with a cross section from 3 to 200 mm^2 in a protective atmosphere (a); the process of obtaining HB-4 nanocrystalline alloy plates with a cross section of 3×10 and 5×10 mm^2 by pouring the melt into a copper quenching unit in air (b, c)

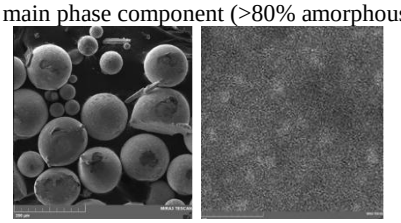
The basis of the technological scheme for obtaining bulk samples was the ejection of the processed (overheated and aged) melt in a certain way. An important factor in this process was the achievement of minimum melt viscosity to ensure rapid and complete filling of the quench mold. In this regard, the most promising alloys are HBRM-4, NHRP-4, NHRP-6, HB-4 and HBKNV-2 (the strongest plate with a thickness of 2 mm was obtained). It should be noted that the last alloy was the most doped with cobalt, tungsten and niobium, was nanocrystalline, although its casting properties were not optimal, in particular, the kinematic viscosity was the highest.

Thus, a technique for obtaining fast-hardening Fe–(Ni, Co, Cr, Mn, Mo, W, V, Nb)–(Si, B, C, P) alloys was proposed, which ensured the formation of a predominantly amorphous state in plates with a cross section of up to 40 mm^2 and nanostructured - in plates up to 100 mm^2.

3.4 Production of amorphous nanocrystalline and submicron powders of HB-4 and NHRP-6 alloys

Dispersed powders from HB-4 and NHRP-6 alloys with a nanocrystalline and partially amorphous structure were obtained by rapid quenching of the melt in two ways: ultrasonic plasma atomization and spraying of the melt in water. The Polish plasma ultrasonic atomizer "ATO LAB" (www.metalatomizer.com) of the company LLC "TECHNOLOGY PARK" "UKRAINIAN INFORMATION AND TELECOMMUNICATION TECHNOLOGIES" (Kyiv) was used. In the "ATO LAB" installation, the melting of the source alloy rod was carried out by a plasmatron burner in an argon atmosphere. The process of atomization (formation of microdroplets with a size of 20-130 μm) occurred during the spreading of melt droplets on a small polished tungsten plate that vibrated with a frequency of 20 kHz and was cooled by water. By this method, a dispersed powder of HB-4 alloy was obtained, mainly spherical in shape (Fig. 2 a), the structure of which is mainly nanocrystalline with the size of the structural components of eutectic colonies of 60 nm (Fig. 2 b).

Dispersion of the melt with the help of "Poletiv"(“flights”) in water was carried out using the original installation of LLC "INTER-CONTACT PRIOR" (Kyiv). The principle of operation of the installation is that the molten alloy, previously prepared by high-frequency melting, is poured into a crucible-metal receiver. From there, the melt flows through a hole with a diameter of 4-6 mm in the lower part of the metal receiver. The melt stream is crushed by impact vanes (flights), which rotate at a speed of 2000 to 3500 rpm. depending on the type of alloy and the properties of the powders to be obtained. By changing the speed of rotation of the blades (rotor), it is possible to change the granulometric composition of powders and, thereby, their technological properties - bulk density, fluidity, and others. In one cycle, you can get from 10 to 18 kg of powder. After grinding, the melt particles are cooled by falling into the water that fills the spray chamber. After the spraying cycle, the powder carried by the water stream into the receiving tank is dehydrated, stabilized, and dried. HB-4 alloy powder (Fig. 3) is characterized by high thermal stability of the main phase component (>80% amorphous phase).



a b

Fig.2 SEM image of HB-4 alloy powder with a submicron structure obtained by ultrasonic atomization of the melt

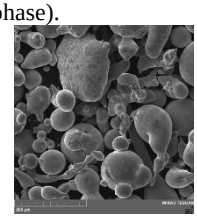


Fig. 3 SEM image of HB-4 alloy powder obtained by spraying the melt in water.

The actual invariance of the thermophysical characteristics in comparison with the original ingot of the alloy is also demonstrated.

3.5 Methods of studying the structure and thermal stability of the amorphous state in hardened strip, powder and bulk alloys

The as-prepared and heat treated samples of ribbons, plates and powders were structurally characterized by X-ray diffraction (XRD) using Fe filtered Co Kα and monochrome Mo Kα radiation in a DRON-3M automated diffractometer. The experimental diffraction patterns of the partially crystallized samples were considered as a superposition of intensities scattered from amorphous and crystalline (bcc α-Fe (110) peak) phases [3]. The volume fraction of

crystalline phase was calculated as $X_{cr} = A_{cr}/(A_{cr} + A_{am})$ [4], where A_{am} and A_{cr} are the integral intensities of maxima corresponding to amorphous and crystalline phase respectively. The average grain size, L, in the partially crystallized samples was estimated from the half-width of the XRD peaks B_θ (after instrumental broadening subtracting and neglecting possible strain contributions) using the Scherrer's equation $L \approx \lambda/(B_\theta \cos\theta_B)$, where θ_B is the peak position. In turn, from the values of X_{cr} and L the volume density of α-Fe nanocrystals was estimated as $N = 6\,X_{cr}/(\pi L^3)$.

The thermal stability of non-equilibrium (amorphous or nanocrystalline) structures that are formed in strip, powder and bulk samples during the rapid cooling of the melt, as well as the nature and kinetics of their transition to the equilibrium state, was studied by the method of differential scanning calorimetry (DSC) on a NETZSCH 404 calorimeter in conditions of continuous heating at rates of 5, 10, 20 and 40 K/min. Electron microscopic analysis The micro- and nanostructure of quick-hardened tapes, powders, surfaces and chips of bulk samples and applied coatings was studied by the method of raster electron microscopy on a Tescan Mira 3 LMU microscope with determination of the local chemical composition using an energy dispersive spectrometer X-MAX 80 mm Oxford Instruments. For a more complete characterization of the sample structure, a JEOL JSM - 6490 LV, 10–20 kV microscope was additionally used. Investigations of the surface of plates, powders, annealed ribbons without preliminary treatment and grinds of the ends of ingots (hardened plates) and steel with a coating were carried out in the modes of reflected and secondary electrons.

The microhardness, H_μ, measurements of the as-quenched and annealed melt-spun ribbons were performed using standard PMT-3 tester with 136° diamond pyramid indenter and a 0.686 N (70 gf) load. At least 20 indentations during 10 s were made for each microhardness value reported in this paper and the standard deviation was near to 3% of the mean value.

4. Results and discussion

4.1 Peculiarities of the formation of the nanocrystalline heterophase structural state in complex alloys of the system $Fe_{58,5–66}(TM)_{13,1–26}(Si,C,B)_{18–24,4}$

According to the results of X-ray studies (Fig. 4), the structure formed in 2- and 3-mm-thick castings of the HBRM-4 alloy consists of nanocrystals with sizes of 16–43 nm of a solid solution based on α-Fe, boride TM_2B (TM - transition metal) and a small amount of carbide Fe_5C_2. It can be seen that the relative amounts of α-Fe nanocrystals, boride, and carbide depend on the cooling rate. The crystallization of these phases in the supercooled melt occurs separately, and with an increase in the cooling rate, the crystallization of the boride phase is significantly suppressed.

It was established that the crystallization of the amorphous ribbon takes place in two clearly separated stages, in the first of which nanocrystals of a solid solution based on α-Fe are formed, and in the second - nanoscale crystals of boride Me2B (carbide Fe_5C_2 could not be detected in the ribbons) (Fig. 5).

The analysis of the profile of the diffraction line of the sample after the first stage of crystallization of the amorphous ribbon showed that the average size of solid solution nanocrystals based on α-Fe, L, and their relative fraction, X, are 10 nm and 35%, respectively. At the second stage of crystallization, crystals of the Fe_2B isostructural boride phase are formed in the remaining amorphous matrix, and primary crystallites with bcc structure are aggregated (Fig. 4). The bulk density of α-Fe nanocrystals, $N=6X/(\pi L^3)$, formed at the first stage of crystallization of the amorphous phase of the HBRM-4 alloy, is approximately 6.7×10^{23} m^{-3}.

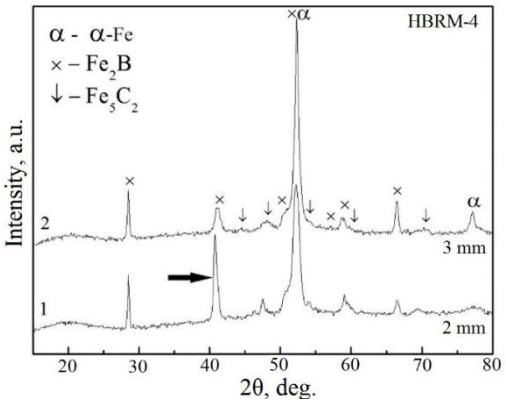


Fig. 4 *Diffractograms of samples of rapidly cooled castings HBRM-4 alloy thickness 2 mm (1) and 3 mm (2). α – α– Fe, × – isostructural phase boride Fe_2B, and ↓ isostructural phase Fe_5C_2, respectively. The arrow shows the (200) line of Fe_2B boride, the width of which was used to calculate the size of the crystallites*

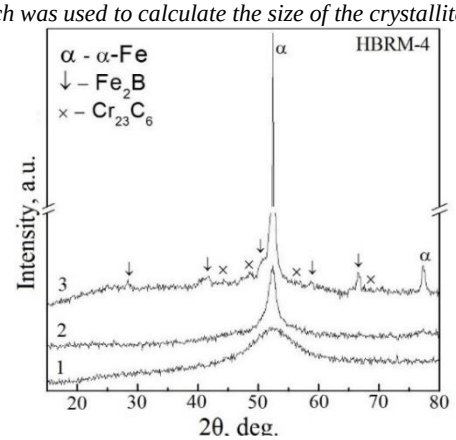


Fig. 5 *Diffractograms of alloy ribbons HBRM-4 in the initial state (1) and after heating at a rate of 10 K/min. to the temperatures of completion of the first (2) and second (3) stages of crystallization*

The structure of the HBRM-4-1 alloy rod with a diameter of 2.7 mm consists of α–Fe crystals and phases isomorphic to borides $Cr_{23}C_6$ ($Fe_{23}B_6$), Fe_3B and carbide $(Fe,Cr)_7C_3$. The evaluations showed that the average size of α–Fe crystals and $Fe_{23}B_6$ boride in the structure of the HBRM-4-1 alloy rod is 19.0 and 32.0 nm, respectively.

Study of a bulk sample (plate 3 mm thick) of the alloy $Fe_{61,37}Cr_{3,78}Co_{6,84}V_{0,85}W_{0,82}Mo_{1,06}Nb_{0,85}B_{19,87}C_{1,99}Si_{2,57}$ (HB-4), in which, in comparison with the alloys HBRM-4 and HBRM -4-1, the chromium content was significantly reduced and 0.85 at.% vanadium and almost 7% Co were added, showing that its structure is completely crystalline. Three phases with nanoscale grain sizes are present in the plate structure: α–Fe (100–130 nm), an isostructural phase of Fe_3B boride, (≥ 150 nm) and a small amount of an unknown phase (15–21 nm).

4.2 Nanocrystallization and volumetric amorphization of complex alloys synthesized from industrial raw materials Fe–(Ni,Co,Cr,Mn,Mo,V,Al)–(Si,B,C,P)

Alloys of nominal composition (weight up to 1 kg) of the second (NHRP-3, 4, 6) group were obtained using industrial raw materials in the form of plates with a thickness of 5, 3, 2 and 0.5 mm, as well as in the form of amorphous tapes. X-ray studies showed that ingots with a thickness of 3 and 5 mm of all these alloys had a crystalline structure. The structure of the NHRP-6 alloy, highly doped with phosphorus and carbon, consists of α-Fe crystals, non-equilibrium borocarbides $TM_3(B,C)$ and $TM_{23}(B,C)_6$, and some isostructural Fe_2P (Co_2P type) and Fe_3P phases. A similar phase composition was observed in $Fe_{73}Mo_3Si_{3,3}P_{8,7}C_{7,0}B_{5,0}$ alloy ingots [5]. At the same time, the structure of the NHRP-4 ingot is

significantly simpler and consists mainly of solid solution crystals based on γ–Fe and the equilibrium boride TM_2B. The observed differences in the phase composition of the ingots are most likely due to the increased concentration of nickel in the NHRP-4 alloy, which stabilizes the fcc modification of Fe, the increased solubility of metalloids in the γ–Fe lattice, and the reduced Mo content, which contributes to the inhibition of the formation of Fe-based γ–solid solution crystals. The presence of equilibrium boride in this alloy is obviously caused by the highest boron content. A characteristic feature of the diffraction lines of borocarbide crystals on the diffractogram of the alloy plate is their wide width, which is typical for nanoscale objects. Approximate estimates of the average sizes of $TM_3(B,C)$ and $TM_{23}(B,C)_6$ crystallites and phases of isostructural phosphides based on the width of reflexes on X-ray images gave values of 22, 27, and 28 nm in the NHRP-6 alloy plate. At the same time, the width of the (111) γ–Fe reflex in the diffractogram of the NHRP-4 alloy ingot is significantly lower, and the crystallite size estimate was over 100 nm.

4.3 Structure and microhardness of rapidly cooled ribbons and bulk samples

The structure and microhardness of rapidly cooled ribbons and bulk samples are summarized in table.2.

Tabl. 2 *Structure and microhardness of rapidly cooled ribbons and bulk samples*

Alloy brand	Ribbon (A*)	Bulk samples (NC*)	
	H_{μ}^{ribb}, GPa	H_{μ}^{bulk}, GPa	Phases
Group 1			
HBRM-4	10,28 ±0,06	9,55±0,06	α-Fe + Fe_2B
HBRM-4-1	9,14±0,05	11,09±0,05	α-Fe + $Fe_{23}B_6$ + Fe_3B
Group 2			
NHRP-3	11,20±0,12	14,61±0,12	α-Fe + Fe_2B + Fe_3B
NHRP-4	9,83±0,45	7,19±0,04	γ-Fe + Fe_2B
NHRP-6	8,85±0,06	12,23±0,08	α–Fe +$Cr_{23}C_6$ ($Fe_{23}B_6$) + Fe_3B + traces (Fe_2P (Co_2P) + Fe_3P)
Group 3			
HB-4	12,390±0,060	12,65±0,06	α-Fe + Fe_2B + X
		8,15±0,06	γ-Fe + Fe_2B+ X
HBKNV-1	11,220±0,051	12,04±0,07	α-Fe + Fe_2B + X
HBKNV-2	11,142±0,065	15,25±0,13	α-Fe + Fe_2B + X1 +X2
HBKMN-1	11,136±0,160	11,85±0,09	α-Fe + Fe_2B + X

* Structure: A – amorphous, NC– nanocrystalline

Measurements of the microhardness of amorphous ribbons of alloys of the NHRP group showed that its values lie in a wide range from 8.84 GPa (in the alloy of the NHRP-6 brand) to 11.2 GPa (in the alloy of the NHRP-3 brand), which is due to significant variations in the content of alloying elements (both metals and metalloids) (Table 2). The range of microhardness values of volume samples of alloys of the NHRP group is even wider - from 7.2 to 14.6 GPa, they are higher than the Hμ of amorphous tapes of alloys of the NHRP-3 and NHRP-6 brands, and lower than that of the alloy NHRP-4. Comparing the value of Hμ with the results of structural studies, it can be stated that the low microhardness of bulk samples of the NHRP-4 alloy is caused by the presence of a relatively high proportion of solid solution crystals based on γ-Fe in its structure. On the contrary, the plate of the NHRP-3 alloy, in the structure of which there are solid solution crystals based on α-Fe, has the highest hardness.

The microhardness of ribbons of alloys of the third group in the amorphous state is higher than that of the alloys of the groups considered above, and lies within relatively narrow limits of 11.1–12.4 GPa (Table 2). It is noteworthy that the hardness of HB-4, HBKNV-1, and HBKMN-1 alloy ingots with a nanocrystalline structure was close to, although slightly higher than, the hardness of amorphous strips (11.8–12.6 GPa), with the exception of the HBKNV-1 alloy ingot. Hμ of which in the initial state was 15.25 GPa. A comparison of the phase composition of ingots HBKNV-1 and HBKNV-2 shows that the increased hardness of the latter alloy is due to the presence of an additional phase in its structure. The hardness index of the HBKNV-2 alloy corresponds to the yield strength of 4.4 GPa, the value of which is close to the experimentally determined strength limit (4.7 GPa) of the bulk amorphous alloy $Fe_{52}Co_{20}Nb_4B_{20}Si_4$ [6].

4.4 Thermal stability and nanocrystallization of amorphous ribbons, powder and plates

The thermal stability of the amorphous state is one of the most important characteristics of alloys with an amorphous structure, the quantitative indicator of which was chosen in the work as the temperature of the beginning of crystallization, Tons, which was determined by DSC thermograms under heating conditions at different speeds.

In addition to the temperatures of the beginning of crystallization, the number of stages of their transition to the equilibrium crystalline state and the dynamic temperatures of these stages (temperatures of maximum transformation rates, T_{xi}) are also important parameters of the thermal stability of amorphous alloys, since each of them significantly affects the mechanical properties. The listed parameters characterizing the thermal stability of amorphous phases in the investigated alloys and the transition to the crystalline state at a heating rate of 20 K/min are summarized in Table 3. Glass transition temperatures Tg were determined as the inflection point of the thermogram and their values were used as a component of parameters characterizing the tendency of melts to amorphize.

Tabl. 3 *Parameters of thermal stability of amorphous ribbons*

Alloy brand	T_g, K	T_{ons}, K	$T_{ons} - T_g$, K	T_{x1}, K	T_{x2}, K	T_{x3}, K	T_{end}, K	T_{end}-T_{ons}, K
HBRM-4	767	803	36	832	925		992	189
NHRP-3		879		892			915	36
NHRP-4	755	764	9	777			790	26
NHRP-6	765	781	16	811			893	175
HB-4	818	830	12	845	1000		1030	200
HBKNV-1	831	848	17	875	982	1088	1110	262
HBKNV-2	860	886	26	910	1007	1076	1100	214
HBKMN-1	820	841	21	866	907	972	1000	159

Significant variations in the thermal stability of amorphous phases were observed in the group of NHRP alloys - from 765 K (NHRP-4 alloy) to 879 K (NHRP-3 alloy). The multi-component composition of the studied alloys and non-systematic changes in the concentration of metalloids and strengthening elements in NHRP alloys do not allow us to unambiguously establish the causes of sharp changes in the thermal stability of amorphous phases, in particular, the exceptionally high value of Tons in the NHRP-3 alloy. The character of the DSC curves of this group of alloys indicates that a one-stage process of eutectic crystallization takes place in them.

The temperature values of the start of crystallization of the third group of alloys (HB grades) lie in a relatively narrow temperature range - from 830 K (HB-4 grade alloy) to 886 K (HBKNV-2 grade alloy), and the process of transition to the crystalline state occurs in two (alloy grade HB-4) and three (all other alloys of this group) stages.

The obtained values of the activation energy (E_{a1}) of the first

stage of crystallization of the investigated alloys lie in a relatively wide range of values (from 386 to 731 kJ/mol), which is consistent with the few results given in the literature for complex-alloyed amorphous alloys based on Fe. The highest values of effective crystallization activation energy are characterized by: eleven-component alloy NHRP-6 - 629 kJ/mol, which had the highest glass-forming ability among alloys synthesized using industrial raw materials, and ten-component alloy HB-4 - 731 kJ/mol.

These two alloys were chosen to obtain powders. X-ray structural studies were carried out on the original powder with a wide range of sizes, as well as on the powder sifted through a sieve - with a fraction of 4-40 microns. Research has shown noticeable (Fig. 6) differences in the structure of these samples.

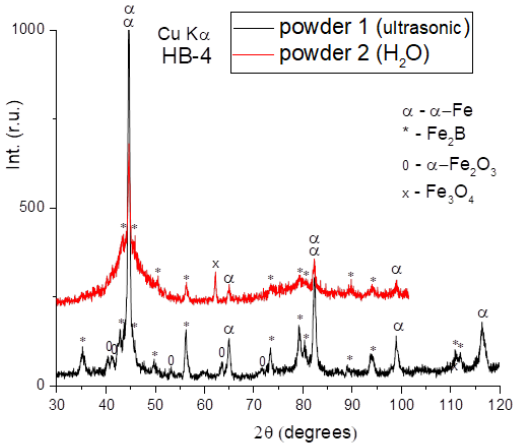


Fig.6 *Structural and phase composition of rapidly cooled powder in the initial state*

The results of calorimetric (DSC) studies of powders of different production methods and different fractions are shown in fig. 7 and in table 4.

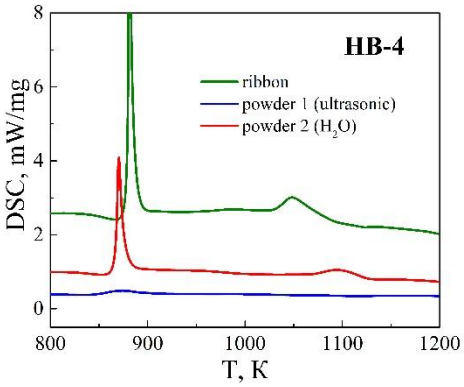


Fig. 7 *DSC – curves of initial powders and amorphous ribbons.*

The calculation of the ratio of the total heat release during the crystallization of the amorphous phase in the powders to the heat release during the crystallization of 100% of the amorphous phase of the tape made it possible to more accurately determine the volume fraction of the amorphous phase in powders of the HB-4 alloy hardened by various methods, as well as to determine it in powders of different fractions (tabl. 4).

The obtained results are correlated with X-ray data on the determination of the volume fraction of the amorphous phase in powders.

Tabl. 4 *Results of calorimetric studies of hardened powders of HB-4 alloy*

Sample	Peak				Total heat release, J/g	Percentage of amorphous phase, vol. %
	I		II			
	T, K	S, J/g	T, K	S, J/g		
Atomized powder 30-120μm	874	5,76			5,76	6,32
Powder sprayed in H_2O, 4-370 μm	870	30,08	1094	9,94	40,018	43,92
Powder sprayed in H_2O, <40μm	850	74,04			74,04	81,26
Ribbon, h=25 μm	881	69,48	1048	21,6	91,11	100

The effective activation energy of the first stage of crystallization of the amorphous phase in the dispersed (< 40 μm) powder sprayed in water was lower than this value for the amorphous tape by only 7%.

4.5 Formation of micro- and nanocomposite states in protective coatings applied by various methods

The proposed iron-based eutectic alloys NHRP-6 and HB-4 can be classified as self-fluxing. The use of gas-thermal (HT) sputtering by the "cold method" with the use of a CastoDyn 8000 torch makes it possible to obtain dense nanocomposite uniform coatings using HB-4 powder obtained as a result of grinding the original amorphous ribbons. For this alloy, reducing the temperature of the powder during sputtering allows you to preserve its nanodispersed amorphous structure, and the energy provided by the flame is optimally sufficient not only for diffusion welding, but also for the nanocrystallization of already deposited microflakes (powders) and the formation of a heterophase nanocrystalline structure of the coating. The estimated sizes of nanocrystals of the main component fractions of BCC - iron and boride Fe_2B are, respectively, 35±5 and 45±5 nm. The phase composition of the α-Fe + Fe_2B + X coating practically coincides with the composition of the bulk hardened plate (3 mm thick) of this alloy.

When using HB-4 alloy flakes of larger sizes (63-100 microns), which are the most mass fraction when grinding the tape in a planetary mill, reducing the temperature of the substrate and performing GP sputtering without an underlayer on the roughly polished surface of St.3, it was possible to obtain record microhardness values of 24,90-27.25 GPa, which could not even be predicted when studying phase formation and kinetics of nanocrystallization of HB-4 alloy. The obtained values of $H\mu$ are noticeably higher even than the values for the best carbide-containing powder mixture Eutalloy 1229 SJ with 60% WC formed by melting ($H\mu$ = 20-25 GPa)

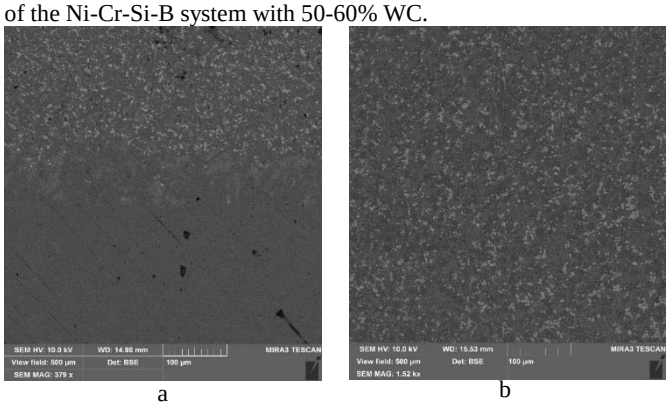
Gas-flame coatings from the NHRP-6 alloy, applied using an underlayer and coarse powder (flakes) 63-100 microns, after their heat treatment in a protective medium (Ar), exceed the microhardness value for the industrial powder PRN-65X25C3P3-3 by almost two times.

GP sputtering and alternation of the process of sputtering layers with their melting on 10-mm-thick rolled samples of 40X structural low-alloy steel were carried out with the initial (not dispersed into fractions) HB-4 alloy powder obtained by mechanical grinding of the melt and quenching in water. Such welded coatings are characterized by greater density and a noticeable transition layer between the substrate and the coating itself, which provides them with better adhesion. Figure 8 a shows an SEM image of such a coating. The thickness of the deposited layer was 400±30 μm, and the transition layer was about 100 μm. In fig. 8 b shows SEM

images of the HB-4 plate obtained by quenching the melt in a copper mold. It can be seen that the dimensions of the excess borocarbide phase in these photos (light crystals) are almost the same (2-5 μm), which indicates a considerable cooling rate of the melt in the layer that was melted.

As a result of rapid melting of the powder, diffusion welding with the steel of the base occurs, which leads to high adhesive and cohesive resistance of the coating.

The obtained high Vickers hardness values HV_{100}=820-880 correspond to the Rockwell hardness HRC = 65-67, which are among the best reported for coatings based on composite powders of the Ni-Cr-Si-B system with 50-60% WC.



a b

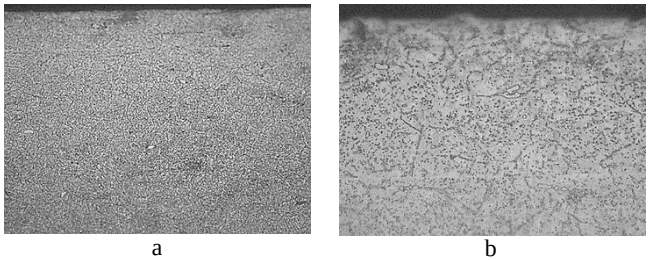
Fig. 8 *– SEM image deposited on a layer of HB-4 alloy (a) and HB-4 plate (b).*

In general, all samples (including rapidly cooled powders) of the developed nanoalloys also show a high anti-corrosion ability, which is due to the formation of dense protective surface oxide layers, therefore the mass loss (surface corrosion) of new economically alloyed nanostructured alloys is less than 1.2-3.4 g /m^2 per year, which is several times better than the indicators of industrial high-strength alloyed and austenitic stainless steels and special alloys.

4.6 Approbation of amorphous-nanocrystalline eutectic alloy NHRP-6 for wear-resistant coatings in the conditions of pipe rolling production

The publication [7] with the participation of the authors of this study presents the results of using the amorphous-nanocrystalline eutectic alloy NHRP-6 for wear-resistant coatings in the conditions of industrial pipe rolling production.

The surface microstructures of the coating applied to 4H5MF1C steel are shown in Fig. 9. On the surface of the samples, there is a coating of an amorphous alloy, and the core (steel) and the transition layer are tempered martensite and carbides of chromium, tungsten, molybdenum, and vanadium.



a b

Fig. 9 *Surface microstructure of 4H5MF1C steel samples after plasma application of coatings from amorphous powder of NHRP-6 alloy powder; x200 (a); x800 (b)*

The proposed technology, which includes obtaining an amorphous tape of the Fe-Ni-Si-B-P-C system, powder from it and applying it to the surface of the pipe-rolling tool by the plasma method. Testing in factory conditions of rollers and support bars of the state of KhPTR "15-30" with an applied coating showed an increase in their stability by 20÷25% in comparison with the technology used at enterprises and an improvement in the quality of the inner surface of the pipes. The proposed technology of thermal strengthening and additional application of nanocoatings from amorphous alloys with a thickness of 100 ÷ 150 μm by plasma spraying on the working surface of the pipe tool eliminates the third tempering, changes the structure and properties of the surface layer, increases strength, wear resistance and hardness up to $HV_{0.1}$ 950÷1050 (compared to HV 587÷690 according to existing technology). As a result, the steel acquires high hardness on the surface, which is necessary in conditions of significant pressure and friction when working on pipe rolling mills.

5. Conclusion

1. Using the method of ultrasonic plasma atomization of the melt, a dispersed powder of HB-4 alloy of mostly spherical shape was obtained, the structure of which was mainly nanocrystalline with the size of structural components of eutectic colonies of 60 nm. The possibility of obtaining a dispersed powder of this alloy was also demonstrated by the method of mechanical dispersion of the melt with quenching of the formed droplets in water, which is characterized by high thermal stability of the main phase component (>80% amorphous phase) and the actual invariance of thermophysical characteristics in comparison with the original ingot of the alloy.

2. Quantitative data were obtained regarding the kinetics and mechanisms of the formation of nanocomposite states in Fe-PM-X alloy coatings applied by various gas-thermal (gas-flame and plasma) methods (including remelting). Correlations were established between the parameters of the nanoscale structure of the applied coatings and the level of strength characteristics of the "base-coating" system, the temperature-time regimes of the formation of nanostructures with the optimal level of physical and mechanical properties.

3. New wear-resistant powder alloys of the eutectic type for coatings and methods of their application at industrial was positively approve. In particular, powder alloys and their application technology are at the stage of implementation, including as a material for the restoration of agricultural tillage equipment, and has already passed control tests.

Literature

1. Marcus M. On the correlation between glass-forming tendency and liquidus temperature in metallic alloys. - Mater. Sci. Eng., Vol. 23, 1976, P. 211 – 214. (Marcus M., D. Turnbull.)
2. Inoue A. Stabilization of metallic supercooled liquid and bulk amorphous alloys.- Acta Mater, Vol. 48, 2000, P. 279 – 306.
3. Botta W.J. Crystallization of Fe-based amorphous alloys.- J. Non-Cryst. Sol., Vol. 247, 1999, P. 19–25. (W.J. Botta, F.D Negri, A.R. Yavari)
4. Wesseling P. Quantitative evaluation of α-Al nano-particles in amorphous $Al_{87}Ni_7Gd_6$ – comparison of XRD, DSC, and TEM.- Scr. Mater. Vol. 48, 2003, P. 1537–1541. (Wesseling P, B.C. Ko, J.J. Lewandowski)
5. Jiao Z.B. Effects of alloying elements on glass formation, mechanical and soft-magnetic properties of Fe-based metallic glasses.- Intermet. Vol. 19, 2011, P. 1502 – 1508. (Jiao Z.B., H.X. Li, J.E. Gao, Y.Wu et. al)
6. Kim H.-K. Ductile Fe-based amorphous alloy.- Mater. Sci. Eng. A. Vol. 552, 2012, P. 399–403. (Kim H.-K., Lee K.-B., Lee J.-Ch.)
7. Krivchik L. Strengthening of pipe tools for cold roller rolling of corrosion-resistant pipes by application of amorphous alloys.- PAST. №5, Vol.135, 2021, P. 131-138. https://doi.org/10.46813/2021-135-131/ (Krivchik L., Khokhlova T., Pinchuk V., Holovachov A., Srebryansky G., Nosenko V., Zagorodniy O.)